OUKA
The University of Osaka
Institutional Knowledge Archive

Title	Resolved CFD-DEM Simulation of Gas-Liquid-Solid Three-Phase Flows with Controlled Interfaces
Author(s)	Nguyen, Thanh Gian
Citation	大阪大学, 2021, 博士論文
Version Type	VoR
URL	https://doi.org/10.18910/85256
rights	
Note	

The University of Osaka Institutional Knowledge Archive : OUKA

https://ir.library.osaka-u.ac.jp/

The University of Osaka

Doctoral Dissertation

Resolved CFD-DEM Simulation of Gas-Liquid-Solid Three-Phase Flows with Controlled Interfaces

Nguyen Thanh Giang

March 2021

Graduate School of Engineering

Osaka University

Abstract

In this study, a resolved CFD–DEM model for gas-liquid-solid three-phase flows was developed where CFD (Computational Fluid Dynamics) and DEM (Discrete Element Method) were used for simulating fluids and particles behaviours, respectively. In the three-phase flow simulation, it is of paramount importance to properly consider particle-particle, particle-fluids and interfacial interactions (such as surface tension and wetting of particle surface). This study focused on the modelling of the interaction between particles and fluids as well as the interfacial interactions. The unique point of this study is that both particle-fluids and gas-liquid interfaces are represented as smooth transition regions with controllable thickness. Three main models were developed for (i) particle-fluids interaction, (ii) interface capturing and (iii) wetting and capillary force. A summary of model development and key findings in each model is as follows:

(i) The particle-fluids interaction was considered by using the Volume Penalisation (VP) method, which is a family of the continuous forcing Immersed Boundary (IB) method. A smooth mask function has a profile of a hyperbolic tangent and allows to control the interface thickness. Optimal permeability was determined so as to reduce the model error in the momentum exchange between particle and fluid associated with the VP method, which was determined as a function of only the interface thickness and fluid kinematic viscosity. Sensitivity analysis of interface thickness was performed to evaluate the accuracy of the VP method with the smooth mask function and the optimal permeability. Several test cases were solved to check the

validity of the VP method for the particle flows in various systems, i.e. from dilute to relatively dense flows, and the results showed good agreement with the exact solution or empirical correlations. It was found that the error of lubrication force on a spherical particle approaching to a wall can be correlated with the ratio between the gap and interface thickness. The resolved CFD–DEM model developed was also applied to predict the relative viscosity of suspensions and the density segregation in fluidised beds.

(ii) The interface capturing method used in the present study was based on a colour function. The thickness of the gas-liquid interface was controlled by using both interface compression and diffuse interface techniques simultaneously whilst the CSF model was used to calculate the surface tension force. It was found from the validation simulations of a static droplet that the accurate evaluation of the surface tension force can be achieved by appropriately controlling the interface thickness. Moreover, the interface compression can be applied in the dynamic case to suppress the significant amount of interface smearing when the gas-liquid interface deforms drastically.

(iii) The wetting of the particle surface was expressed by the Immersed Free Surface (IFS) model, which artificially extends the gas-liquid interface into the interior of the particle. Based on the aforementioned gas-liquid interface capturing method in the IFS framework, the accuracy of two of the major methods in the literature to calculate the capillary force acting on particles was discussed. The wetting model was validated by both static and dynamic cases. Simulations of two colliding particles with a liquid bridge were performed to demonstrate the applicability of the resolved CFD–DEM model developed to a complex three-phase system.

CONTENTS

Abstract i

Acknowledgments ix

Preface xi

List of Figures xiii

List of Tables xix

1. Introduction 1

1.1 Background 1

1.2 Resolved CFD–DEM model for gas-liquid-solid three-phase flows 3

1.2.1 Hydrodynamic interaction model between particles and fluids 4

1.2.2 Interface capturing method 6

1.2.3 Wetting and capillary force models 8

1.3 Research objectives 9

1.4 Overview of the dissertation 10

2. Finite Volume Method for CFD 13

2.1 Introduction 13

2.2 Finite Volume Method for CFD 13

2.2.1 Spatial discretisation 14

2.2.2 Discretisation of equation 16

2.2.2.1 Face interpolation schemes 17

2.2.2.2 Gradient 18

2.2.2.3 Time derivative 19

2.2.2.4 Convection term 19

2.2.2.5 Diffusion term 20

2.2.2.6 Source term 21

2.2.2.7 Boundary conditions 21

2.2.3 Temporal discretisation 23

2.3 Summary 25

3. Discrete Element Method 26

3.1 Introduction 26

3.2 Discrete Element Method (DEM) 26

3.3 Soft-sphere model 29

3.3.1 Elastic repulsion force 32

3.3.2 Damping coefficient 33

3.3.3 Critical time step for DEM 35

3.3.4 Integration scheme 36

3.4 Summary 39

4. Fluid-Solid Two-Phase Flows with Volume Penalisation Method.....40

4.1 Introduction 40

4.2 Governing equations.....41

4.2.1 CFD governing equations 41

4.2.2 DEM governing equations 42

4.3 Optimal permeability.....43

4.4 Numerical solution procedure 49

4.5 Model validations 52

4.5.1 Flow past a stationary single particle.....52

4.5.2 Flow through a periodic array of stationary particles 58

4.5.3 A particle approaching to a plane wall 63

4.6 Model applications 68

4.6.1 Relative viscosity of suspensions 68

4.6.2 Simulation of fluidised bed.....71

4.7 Summary 75

5. Gas-Liquid-Solid Three-Phase Flows with Immersed Free Surface Model and Controlled Interfaces 79

5.1 Introduction 79

5.2 Governing equations 80

5.2.1 CFD governing equations 80

5.2.2 DEM governing equations 81

5.3 Interface capturing method 81

5.4 Surface tension force model 84

5.5 Immersed Free Surface model 85

5.6 Capillary force and torque 88

5.7 Numerical solution 91

5.7.1 MULES 91

5.7.2 Solution of advection equation 95

5.7.3 Solution of IFS equation 96

5.7.4 Fluid volume correction 97

5.7.5 Numerical solution procedure 98

5.8 Critical time step for diffuse interface 101

5.9 Model validations 104

5.9.1 Laplace pressure in a spherical droplet 104

5.9.2 Liquid bridge force between two stationary particles 109

5.9.2.1 Force due to Laplace pressure 113

5.9.2.2 Capillary force 116

5.9.2.3 Contact angle 118

5.9.3 Particle falling into liquid 122

5.9.4 Dynamic liquid bridge with a free-falling particle 129

5.10 Model applications 132

5.10.1 Influence of wettability on two colliding particles with liquid bridge 132

5.10.2 Analysis of hydrodynamic force acting on two colliding particles with liquid bridge 137

5.11 Summary 144

6. Conclusions 148

6.1 Conclusions 148

6.1.1 Hydrodynamic interaction model between particles and fluids 149

6.1.2 Gas-liquid interface capturing method 150

6.1.3 Wetting and capillary force models 151

6.1.4 Model applications 152

6.2 Suggestions for future work 153

References 155

Acknowledgments

My first acknowledgment goes to my supervisor, Professor Toshitsugu Tanaka, for giving me an opportunity to join his laboratory. I would like to express my deepest gratitude to him for his support, guidance and valuable comments during my research at Osaka University. I am also very grateful to Associate Professor Takuya Tsuji for many of fruitful discussions and valuable comments on my research.

Beside my advisor, I am greatly thankful to the dissertation committees, Professor Takeo Kajishima and Professor Shohji Tsushima (Graduate School of Engineering), for their thoughtful comments and questions, which helped me to widen my knowledge from various perspectives.

This work could not have been finished without the tremendous assistance and support from Senior Lecture, Ph.D. Kimiaki Washino. I would like to thank him for allowing me to use all kind of resources such as developed software and super computer as well as giving me the opportunity to join conferences, which prepared me for my future career. My deepest gratitude also goes to him for his advice, encouragement, motivation and criticism of my research.

This work would not have been possible without the financial support from Japan International Cooperation Agency (JICA) through ASEAN University Network / Southeast Asia Engineering Education Development Network (AUN/SEED-Net) project. I also acknowledge all of JICA and AUN/SEED-Net staff members for their administrative support.

My sincere appreciation goes to all members of Tanaka & Tsuji Laboratory and Vietnamese friends at Osaka University for their support and friendship during my stay in Osaka. Thank you, Jiang and Shi, for your very delicious Chinese foods. Thank you Naoya Shibuya, Seiya Tanaka, Uetsuka, Sakamoto and Yamamoto for the infinite amount of Japanese language assistant. Thank you, Dorian Faroux, for giving your time for English correction of my dissertation. Thank you, Thao, Luong, Dua, Nhan, Ngoc and Thanh, for being a part of the jogging team. I also would like to give special thanks to all members of Suita International Friendship Association (SIFA) and Minoh Association for Global Awareness (MAFGA) for their friendly assistance, which help my life become easier and more enjoyable.

Last but not least, to my dearest family, mother, father and brother who always support and encourage me to overcome everything.

Preface

This dissertation is the original work done by Nguyen Thanh Giang under the supervision of Professor Toshitsugu Tanaka. As the results of this dissertation, two journal articles are published and a poster and an oral presentation are presented at an international conference and a national conference, respectively, as follows:

Journal articles:

- G.T. Nguyen, E.L. Chan, T. Tsuji, T. Tanaka, K. Washino, Resolved CFD–DEM Coupling Simulation Using Volume Penalisation Method, Advanced Powder Technology, 32 (1), 255-236 (2021).
- G.T. Nguyen, E.L. Chan, T. Tsuji, T. Tanaka, K. Washino, Interface Control for Resolved CFD–DEM with Capillary Interactions, Advanced Powder Technology (2021). (accepted)

International conference:

- G.T. Nguyen, E.L. Chan, T. Tsuji, T. Tanaka, K. Washino, Volume penalisation method for solid-liquid-gas flows with immersed free surface. in The 18th Asian Pacific Confederation of Chemical Engineering Congress: Sapporo, Japan (2019), poster PB328.

Domestic conference:

- G.T Nguyen, T. Minamiyama, M. Yoshida, T. Tsuji, T. Tanaka, K. Washino, DNS-DEM coupling simulation of gas-liquid-solid three-phase flow. in JSMF

Multiphase Flow Symposium 2020: Online, Japan (2020), oral presentation 0149.

List of Figures

Figure 1.1. Illustration of gas-liquid-solid three-phase flow simulated by a resolved CFD–DEM model. 3

Figure 2.1. Discretisation of the simulation domain: (a) structured mesh and (b) unstructured mesh. 15

Figure 2.2. Two typical computational cells in 2D. The red line shows the internal face f. 15

Figure 3.1. Illustration of (a) hard-sphere model and (b) soft-sphere model. $V_{1,i}$ and $V_{2,i}$ are the velocities of particles before contact and $V_{1,j}$ and $V_{2,j}$ are the velocities of particles after contact. 27

Figure 3.2. Schematic diagram of the soft-sphere model. 29

Figure 3.3. Spring-dashpot-mass model in one-dimension. 34

Figure 4.1 The mask function distinguishes the particle domain Ω_s and fluid domain Ω_f. (a) the conventional (discontinuous) mask function and (b) the smooth mask function induces a smooth interface region $\Delta\Omega$ (bounded by the dashed lines) while the solid line illustrates the real particle surface ($\chi = 0.5$). 44

Figure 4.2. Smooth mask function χ as a function of the signed distance function σ normalised by the thickness parameter δ 45

Figure 4.3. Velocity profile of the flow between two parallel plates. Re $= 0.5$ and the thickness parameter is chosen as 80 times smaller than the distance between two plates. 49

Figure 4.4. Numerical solution flow chart of the resolved CFD–DEM model for fluid-solid two-phase flows. 51

Figure 4.5. The mask function with different thickness parameter δ; (a) $\delta = d_p/20$, (b) $\delta = d_p/40$, (c) $\delta = d_p/80$ and (d) $d_p/160$. 52

Figure 4.6. (a) Schematic diagram of the flow past a stationary single particle and (b) cross section view of the locally refined mesh. 53

Figure 4.7. Mesh independency test; (a) $\mathrm{Re} = 0.01$ and (b) $\mathrm{Re} = 100$. 55

Figure 4.8. Computed fluid velocity field with thickness parameter of $dp/20$ and $dp/80$ at resolution of 20. (a): Re = 0.01 and (b) Re = 100. 56

Figure 4.9. Comparison between the computed drag coefficient obtained from the simulation and the empirical model of Schiller & Naumann [98]. 57

Figure 4.10. Schematics of the flow through the (a) SC and (b) FCC arrays. 58

Figure 4.11. Relationship between dimensionless fluid force and the resolution. $\phi = 0.2$ and 0.6 for SC and FCC arrays, respectively. 60

Figure 4.12. Comparison of computed dimensionless fluid force and Zick & Homsy's study for SC arrays.....61

Figure 4.13. Comparison of computed dimensionless fluid force and Zick & Homsy's study for FCC arrays. 61

Figure 4.14. Instantaneous velocity field (SCC array, $\phi = 0.3$, resolution of 20 and Re = 0.053); (a) $d_p/20$ and (b) $d_p/160$. The white line presents the particle-fluid interface at $\chi = 0.5$. 63

Figure 4.15. Schematic diagram of a particle approaching to a plane wall. 64

Figure 4.16. The dimensionless fluid force acting on the particle with difference thickness parameters and resolutions when the particle approaches to the bottom wall with a constant velocity. 66

Figure 4.17. The error of the computed fluid force acting on the particle when it approaches to very near the plane wall at resolution of 20 and 40. 67

Figure 4.18. Schematic of suspension in a simple shear flow. 69

Figure 4.19. Relative viscosity plotted with the packing fraction. 71

Figure 4.20. Schematic of fluidised bed. 72

Figure 4.21. Fluidisation of particles at 0.02, 0.4, 0.6, 1.0 and 3.0 second from the left to the right; (a) uniform density and (b) binary mixture beds. The particles coloured in white, pink and purple show 2000, 2500 and 3000 kg/m^3 particles, respectively. ...74

Figure 5.1. Immersed free surface formed inside the particle region. $\boldsymbol{ts}$ and $\boldsymbol{tc}$ are perpendicular to $\boldsymbol{n}_s$ and $\boldsymbol{n}_c$, respectively. 87

Figure 5.2. Illustrations of capillary force models: (a) Model A and (b) Model B. 91

Figure 5.3. Numerical solution flow chart of the resolved CFD–DEM model for gas-liquid-solid three-phase flow. 100

Figure 5.4. Example of colour function fields obtained from (a) unstable and (b) stable simulations. 101

Figure 5.5. Relationship between the critical time step Δt_c and $\Delta x^4/(Ml^2)$. 104

Figure 5.6. Illustration for the spherical droplet in the cube simulation domain. 105

Figure 5.7. Gas-liquid interface of spherical droplet for $l_d^* = 0.0077$ with different interface resolution: (a) $l_{\Delta x}^* = 0.15$, (b) $l_{\Delta x}^* = 0.31$, (c) $l_{\Delta x}^* = 0.62$ and (d) $l_{\Delta x}^* = 0.92$. 107

Figure 5.8. The error of the Laplace pressure for spherical droplet with different gas-liquid interface thickness and resolution; (a) with and (b) without the interface compression term in Eq. (5.6).....108

Figure 5.9. Schematic of liquid bridge between two particles.....110

Figure 5.10. Example of liquid bridge between two particles with immersed free surface.....112

Figure 5.11. Difference of F_{LAP} from the results of the SE solver as a function of δ^*. 114

Figure 5.12. Computed velocity field with $l_{\Delta x}^* = 0.62$; (a) $\delta^* = 0.013$ and (b) $\delta^* = 0.0031$. The white and black lines show $\chi = 0.5$ and $\alpha = 0.5$, respectively. 115

Figure 5.13. Difference of F_{LAP} from the results of the SE solver as a function of l_p^*. 115

Figure 5.14. Difference of F_{CAP} from the results of the SE solver as a function of l_p^*; (a) Model A and (b) Model B.....117

Figure 5.15. Fields of (a) f_s and (b) f_{ccf} calculated with $l_{\Delta x}^* = 0.62$, $l_p^* = 0.0077$ and $\delta^* = 0.025$. The white line shows $\chi = 0.5$, and the isoline of $\alpha = 0.5$ is coloured with f_s and f_{ccf} values. 118

Figure 5.16. Static liquid bridges with different contact angle; (a) 30°, (b) 60°, (c) 90°, (d) 120° and (e) 150°.....120

Figure 5.17. Dimensionless liquid bridge forces; (a)F_{CAP}^*, (b) F_{LAP}^* and (c) F_{LB}^*.....122

Figure 5.18. Schematic of particle falling into liquid. 123

Figure 5.19. Snapshots of particle falling into liquid at t^*= 1.69, 2.57 and 2.75 from left to right (a) with and (b) without interface compression term. 126

Figure 5.20. Comparison between the experiment [139] (left) and the simulation (right) at (a) t^*= 1.69, (b) t^*= 2.57, (c) t^*= 2.75. The dashed line indicates the initial height of the gas-liquid interface.....128

Figure 5.21. Snapshots of dynamic liquid bridge. The top and bottom show the results obtained from the experiment [17] and simulation, respectively; (a) $t = 0$ ms (b) $t = 10$ ms (c) $t = 20$ ms and (d) $t = 26$ ms.....130

Figure 5.22. Temporal change of the distance between two particles with dynamic liquid bridge. 131

Figure 5.23. Schematic of two particles and a spherical liquid droplet. 133

Figure 5.24. Time evolution of particles with liquid bridge with different contact angles; (a) $\theta = 30$o and (b) $\theta = 120^{\mathrm{o}}$. The arrows show the particle velocity. 135

Figure 5.25. Time evolution of particle velocity. 137

Figure 5.26. Time evolution of particle velocity with the contact angle of 45°.....138

Figure 5.27. Instantaneous fluid velocity, penalty term and pressure gradient fields in stage I at $t = 2.432$ ms. (a): fluids velocity U, (b): penalty term f_{VP}; (c) pressure gradient Δp . The arrows show the particle velocity v. The white and black lines show $\chi = 0.5$ and $\alpha = 0.5$, respectively.....139

Figure 5.28. Instantaneous fluid velocity, penalty term and pressure gradient fields in stage II. (a): fluids velocity U, (b): penalty term f_{VP}; (c) pressure gradient Δp . The arrows show the particle velocity v. The white and black lines show $\chi = 0.5$ and $\alpha = 0.5$, respectively. 140

Figure 5.29. Instantaneous fluid velocity, penalty term and pressure gradient fields in stage III. (a): fluids velocity U, (b): penalty term f_{VP}; (c) pressure gradient Δp . The

arrows show the particle velocity v. The white and black lines show $\chi = 0.5$ and $\alpha = 0.5$, respectively. 142

Figure 5.30. Instantaneous fluid velocity, penalty term and pressure gradient fields in stage I at $t = 2.4675$ ms. (a): fluids velocity U, (b): penalty term f_{VP}; (c) pressure gradient Δp . The arrows show the particle velocity v. The white and black lines show $\chi = 0.5$ and $\alpha = 0.5$, respectively.....143

List of Tables

Table 4.1. Calculation conditions for the prediction of relative viscosity of suspension. 69

Table 4.2. Calculation conditions for fluidised bed. 73

Table 5.1. Calculation conditions for critical time step of diffuse interface. 102

Table 5.2. Gas and liquid properties for the calculation of Laplace pressure in the spherical droplet. 105

Table 5.3. Common calculation conditions for liquid bridge between two stationary particles. 110

Table 5.4. Calculation conditions of particle falling into liquid. 124

Table 5.5. Calculation conditions for dynamic liquid bridge with a free-falling particle. 129

Table 5.6. Fluid and particle properties for the simulation of two colliding particles with liquid bridge. 133

Chapter 1

Introduction

1.1 Background

Gas-liquid-solid three-phase flows can be encountered in many industrial processes such as fluidised beds, wet granulation, coating, drying and slurry mixing just to name a few. In these processes, two immiscible fluids, i.e. a gas and liquid, and solid particles, coexist in the same system, flow and interact with each other. It is in general difficult or may require expensive tomographic scanner to observe the movement of fluids and particles by experiments. Therefore, despite a long history of research, our knowledge today towards particle-particle interactions, particle-fluids interactions and interfacial interactions, e.g. surface tension and wetting of particle surface, is still limited.

In the past decades, numerical simulation was sometimes used as an alternative approach of experiments. The computational models proposed in the literature are largely classified into the following two categories: (i) Euler–Euler (E–E) and (ii) Euler–Lagrange (E–L) models. The E–E model, which is also referred to as the Two Fluid Model (TFM) [1,2], treats both particle and fluid phases as inter-penetrating continua and is often employed to investigate the overall flow in large systems. In this model, a constitutive relationship must be predetermined to find particle properties as continuum such as viscosity [3]. Despite the long history of the research in this field,

however, a universal constitutive relationship applicable to different flow regimes is still lacking.

Most of the E–L models couple the Computational Fluid Dynamics (CFD) and Discrete Element Method (DEM). CFD is applied to predict the flow behaviour of fluids while DEM [4] tracks the motion of individual particles by solving the Newton's second law of motion. In general, there are two main CFD–DEM models: the unresolved and resolved CFD–DEM models. The unresolved model, which is originally proposed by Tsuji et al. [5] and simply known as CFD–DEM, solves locally averaged equations for the fluid flow. An empirical closure must be prescribed to express the hydrodynamic forces. The unresolved CFD–DEM model is able to simulate relatively large-scale systems with millions to billions of particles, e.g. a fluidised bed [6–9] and wet granulation processes [10–12]. However, the outcome is largely dependent on the accuracy of the empirical closure used. The resolved model, which is sometimes called DNS–DEM, resolves the detailed flow around individual particles so that the particle-fluids interactions are directly computed from the resultant flow field rather than an input [13–18]. The resolved CFD–DEM model can provide fundamental understanding of the dynamics of the fluids and particles in complex multiphase flows. Complex phenomena such as particulate flow passing through membrane [19], heat transfer in dense particulate flow [20] and breakage of aggregated particles [21] and gas-liquid-solid flow with capillary effect [13,15–18,22–25] are elucidated by the resolved CFD–

DEM simulation. In principle, it can also be used to assess the existing closure relationships and/or generate new ones for the unresolved model.

1.2 Resolved CFD–DEM model for gas-liquid-solid three-phase flows

In a resolved CFD–DEM model for gas-liquid-solid three-phase flows, it is important to consider (i) hydrodynamic interactions between particles and fluids, (ii) gas-liquid interface (i.e. free surface) and (iii) particle wetting and capillary force, as shown in Figure 1.1. The currently available models in the literature are summarised below.

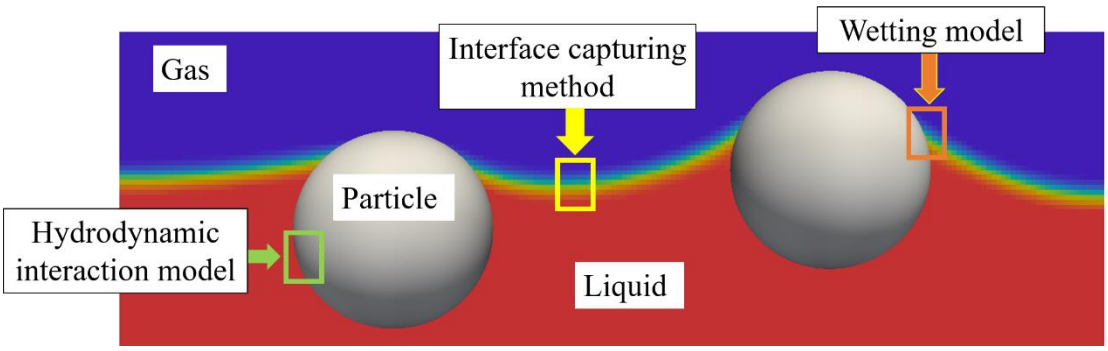

Figure 1.1. Illustration of gas-liquid-solid three-phase flow simulated by a resolved CFD–DEM model.

1.2.1 Hydrodynamic interaction model between particles and fluids

The physical boundaries between particles and fluids are described by using either a body fitted-mesh or Immerse Boundary (IB) method. The former considers the true non-slip boundary condition at particle surfaces. However, it usually requires a great deal of computational effort on the remeshing at every time step if the particles move or the particle surfaces deform. The latter, which is originally proposed by Peskin [26], treats the solid boundary conditions as constraints imposed on the CFD governing equations so that the remeshing step is eliminated.

In the IB method, the impact of the solid on the fluid flow is enforced by solving either discrete or continuous equations, namely the discrete forcing and the continuous forcing approaches [27], respectively. The implementation of the discrete forcing approach totally depends on the discretisation method [28–32] and it can be lengthy especially when higher-order schemes are employed [33–35]. In contrast, the continuous forcing approach is independent of the discretisation procedure. The induced force by the solid is directly added into the (continuous) governing equation [36–38] and the equation can be discretised by any major CFD schemes for the finite volume, finite difference, finite element and spectral methods.

As a member of the continuous forcing IB method, the Volume penalisation (VP) method has been developed mainly for the simulation of the flows with fixed or moving wall boundaries. In this method, an impermeable solid is considered as a porous

medium with a certain value of permeability where the fluid and solid domains are distinguished using a mask function [39–43]. A discontinuous mask function is used in the conventional VP method leading a numerical oscillation in the resultant flow fields [44–48]. In order to get rid of the aforementioned problem, a smooth mask function with finite solid-fluid interface is sometimes used [44,49–56]. The mask function is varied continuously from 0 to 1 across the solid-fluid interface. However, this brings another question: how to determine the permeability? In general, with the discontinuous mask function, the rule of thumb is to use low enough permeability so that only negligible amount of fluid can flow through the solid domain and yet to use high enough permeability so that the simulation can be finished within a reasonable time. Note that the time step interval must be in the same order of or smaller than the value of the permeability to avoid the numerical instability [44]. However, employing excessively low permeability with the smooth mask function makes the penalty term significantly large in the interface. In other words, the interface domain practically becomes solid and the results are dependent on the interface thickness.

Most of the studies which use the smooth mask function in the literature apply an empirical or trial-and-error approach to determine the permeability [44,49–56]. Recently, Hester et al. [43] analysed the VP method using the multiple-scales matched-asymptotics with a signed-distance coordinate system. They proposed an optimal permeability for a given mask function (and its interface thickness) aiming to eliminate the leading order model error, and applied it to the flow past a rotating cylinder in 2D.

However, the applicability of the optimal permeability to the particle-fluid interaction force calculation is not thoroughly discussed.

1.2.2 Interface capturing method

When two incompressible fluids are considered, either an interface tracking method or interface capturing method is used to determine the location of free surface. The interface tracking method, mainly including the marker [57] and front tracking methods [58], traces the movement of free surface explicitly. Although the interface tracking method could be accurate in terms of representing the free surfaces and evaluating the surface tension force, a special treatment is required to handle large deformation (breaking-up and coalescence) of free surfaces [59]. On the other hand, the interface capturing method implicitly captures free surface by using a certain indicator function, e.g. signed distance function [60] and colour function (or order parameter) [61], and can easily handle large deformation of free surfaces. This makes the interface capturing method a preferable choice for the resolved CFD–DEM coupling model although there are several attempts to use the front tracking method as well.

A drawback of the interface capturing method is the accuracy of the surface tension force calculation. In reality, free surface should sharply divide gas and liquid in the macroscopic view point (as opposed to the molecular view point [62]). However, in the interface capturing method, the location of the free surface cannot be directly obtained. The Continuum Surface Force (CSF) [63] model is usually used to circumvent

this problem: the free surface is extended to have a certain thickness (gas-liquid interface region) where the surface tension force is applied. This treatment may cause a large spurious current [64–66] that can deteriorate the simulation accuracy. The magnitude of the spurious current is dependent on the smoothness of the gas-liquid interface region.

In general, employing the colour function gives better mass conservation than the signed distance function when solving the advection equation, i.e. the time evolution step of the indicator function. However, solving the advection equation for the colour function with standard numerical schemes may cause excessive smearing of the interface (numerical diffusion) and the simulation may become unrealistic. One way to prevent this problem is to introduce an interface compression term [67] in the advection equation or apply an anti-diffusion treatment [68]. However, it is reported that the interface compression may lead to poor estimation of the surface tension force [65,66] since the gas-liquid interface region is artificially sharpened. Recently, Washino et al. [69] proposed a method to combine the interface compression and diffuse interface terms in the advection equation to overcome this problem. The desired thickness of the gas-liquid interface can be obtained by choosing appropriate parameters for the diffuse interface term. However, the influence of the diffuse interface parameters on the surface tension force calculation is not thoroughly investigated.

1.2.3 Wetting and capillary force models

In the IB method, the interior of the particles is filled with fictitious fluid and a body force is introduced to enforce the rigid body motion of the particles. It is not straightforward to set the value of the indicator function of the fictitious fluid: inappropriate handling of the indicator function may cause unrealistic mass transfer and excessively large interface curvature. One way to avoid this situation is to artificially extend the free surface in the exterior of particles into the interior in a continuous manner. This technique was originally used for the signed distance function [16,64,70,71] and called Immersed Free Surface (IFS) model by Fujita et al. [71], and later, a similar concept was also applied for the colour function [18,72,73]. The IFS model can be used as a wetting model if the extended free surface is controlled to intersect with the particle surface at a specified contact angle. There are two major approaches [18,23,71] to calculate the capillary force based on a gas-liquid interface capturing method. In the first approach, the surface tension exerted on a three-phase contact line on a particle surface is transformed into the surface tension force exerted on an artificially created immersed free surface in the interior of the particle, and it is applied in the study of Fujita et al. [71] and Sun & Sakai [18]. In the second approach, Washino et al. [23] proposed a Continuum Capillary Force (CCF) model to calculate the capillary force by applying the Dirac delta functions to convert the surface tension (as a line force) at the three-phase contact line into a body force. However, the comparison among these methods is not discussed in the literature.

1.3 Research objectives

This research is dedicated to develop a resolved CFD–DEM model for the simulation of gas-liquid-solid three-phase flows. Heat and mass transfer as well as phase change are not considered in this study. The hydrodynamic force acting on a particle is given by the VP method with a smoothed mask function and the optimal permeability. The interface capturing method with diffuse interface is combined with the IFS model to consider the surface tension and capillary forces. The unique point of the resolved CFD-DEM developed is that both particle-fluids and gas-liquid interfaces are represented as smooth transition regions with controllable thickness. The capillary force is then calculated by the models proposed in the study of Fujita et al. [71] and Sun & Sakai [18] as well as Washino et al [23]. Since the influence of interface thickness (both particle-fluids and gas-liquid) on the calculation of the hydrodynamic, surface tension and capillary forces are not discussed in the literature, the objectives of this study are to investigate the following important matters:

i) The influence of particle-fluids interface thickness on the accuracy of particulate flow simulation.

ii) The influence of the thickness of gas-liquid interface on the accuracy of the surface tension force calculation as well as the simulation stability.

iii) The accuracy of the capillary force models in the framework of the IFS model.

In order to demonstrate the applicability of the resolved CFD–DEM model, it is applied to:

i) Predict of relative viscosity of suspensions.

ii) Analyse the behaviour of the uniform density and binary-mixture fluidised beds.

iii) Analyse the wetting effect and hydrodynamic force acting on two colliding particles with a liquid bridge.

1.4 Overview of the dissertation

This dissertation includes six chapters as follows:

Chapter 1 Introduction:

This chapter provides the background information about the study of the resolved CFD–DEM model. Literature reviews, problem statements on the available models in the literature and the objectives of this study are presented. Overview of all chapters in this dissertation is also shown in this chapter.

Chapter 2 Finite Volume Method for CFD:

This chapter introduces the fundamental principle of the Finite Volume Method (FVM) for CFD. The discretisation applied in the FVM basically includes (i) spatial discretisation, (ii) equation discretisation and (iii) temporal discretisation and they are mainly discussed in this chapter.

Chapter 3 Discrete Element Method:

This chapter introduces the fundamental principle of Discrete Element method (DEM). The motion of discrete particles simulated by a soft-sphere model with a non-linear spring model and an integral scheme is presented.

Chapter 4 Fluid-solid two-phase flows with Volume Penalisation method:

This chapter introduces the resolved CFD–DEM developed with the VP method characterised by the optimal permeability for the study of fluid-solid two-phase flows. Since the optimal permeability is governed by the particle-fluid interface thickness, the influence of particle-fluid interface thickness on the simulation accuracy is tested. Simulations of the flows pass a stationary particle and periodic beds of particles and a particle approaching to a plane wall with different interface thickness are performed. In order to demonstrate the applicability of the resolved CFD–DEM model to the fluid-solid two-phase system, it is then applied to predict relative viscosity of suspension and analyse the behaviour of the uniform density and binary-mixture fluidised beds.

Chapter 5 Gas-liquid-solid three-phase flows with Immersed Free Surface method:

This chapter presents the resolved CFD–DEM model with the controllable gas-liquid interface thickness and the Immersed Free Surface (IFS) model for the study of gas-liquid-solid three-phase flows. A critical time step for the diffuse interface parameter is first proposed in order to avoid an unstable simulation. Laplace pressure

in a spherical droplet and a static liquid bridge between two particles are computed in order to evaluate the influence of diffuse interface parameters on the accuracy of the surface tension force calculation. The accuracy of two capillary force models is examined by computing the capillary force of the static liquid bridge exerted on a particle. The resolved CFD–DEM model developed is also validated by performing simulation of a particle falling into liquid and dynamic liquid rupture between moving particles. In order to demonstrate the applicability of considered models to the complex gas-liquid-solid three-phase system, simulations of two colliding particles with a liquid bridge are finally performed.

Chapter 6 Closure:

This chapter presents the overall key findings and suggestions for future work from this study.

Chapter 2

Finite Volume Method for CFD

2.1 Introduction

This chapter explains CFD principles as a part of the resolved CFD–DEM model. A generic transport equation for the fluid phase is introduced based on the continuum approach. To solve the transport equation, the Finite Volume Method (FVM) is applied to transform the continuous equation into a system of discrete algebraic equations. The basic concept of the FVM is based on the fluxes balance through control volumes by approximating a continuum problem in to discrete quantities. The discretisation applied in the FVM basically includes (i) spatial discretisation, (ii) equation discretisation and (iii) temporal discretisation. Each of them is discussed in this chapter.

2.2 Finite Volume Method for CFD

Finite Volume Method (FVM) was early introduced by MacDonal [74] and MacCormack & Paullay [75] for CFD. The technique is then developed and applied by many researchers [67,76–79]. The FVM solver introduced in this work is based on the literature [67,79]. The FVM generates a system of algebraic equations from a set of partial differential equations. The system of algebraic equations can be expressed in a matrix form and solved by using an appropriate numerical technique to determine a

value for the any considered quantity Φ. A generic form of the standard transport equation for any tensorial quantity Φ is rewritten as follows:

$$\frac{\partial \rho \Phi}{\partial t} + \nabla \cdot (\rho \boldsymbol{U} \Phi) = \nabla \cdot (\Gamma \nabla \Phi) + S_{\Phi}(\Phi) \tag{2.1}$$

where t is the time, ρ is the fluid density, $\boldsymbol{U}$ is the velocity, Γ is the diffusivity and $S_{\Phi}(\Phi)$ is the source term. The first and second terms on the left-hand side of Eq. (2.1) are the time derivative and the convection term, respectively. On the right-hand side of Eq. (2.1), the first term is the diffusion term whilst the second term is the source term in the considered system. The spatial discretisation, equation discretisation and temporal discretisation are presented in Sections 2.2.1, 2.2.2 and 2.2.3, respectively.

2.2.1 Spatial discretisation

The spatial discretisation splits the simulation domain into a small computational mesh or cell where the CFD governing equations are discretised. The simulation domain is totally filled by the contiguous meshes, which do not overlap with one another. There are two main types of mesh: structured and unstructured meshes. Illustrations of structured and unstructured meshes are shown in Figure 2.1(a) and (b), respectively. Structured meshes often have orthogonal quadrilateral elements in 2D or hexahedral elements in 3D whilst unstructured meshes are composed of non-orthogonal elements, e.g. triangles in 2D or tetrahedra in 3D. Since unstructured meshes have arbitrary structures, the connectivity between the mesh elements must be defined and

stored leading to large computational costs. An unstructured mesh is suitable for the study of complicated domain shapes. In contrast to unstructured meshes, structured meshes are simple and less computably expensive and they are mainly applied for relatively simple simulation domains [80]. This work applies a structured mesh and the remainder of this section is discussed based on a structured mesh assumption.

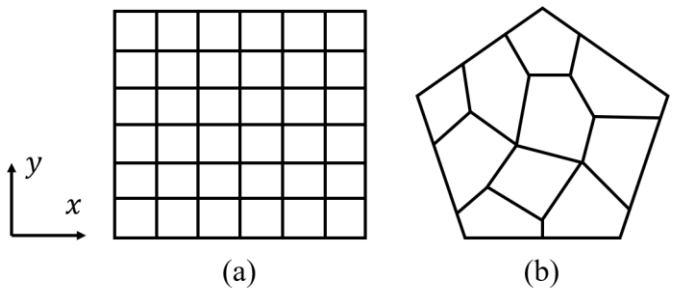

Figure 2.1. Discretisation of the simulation domain: (a) structured mesh and (b) unstructured mesh.

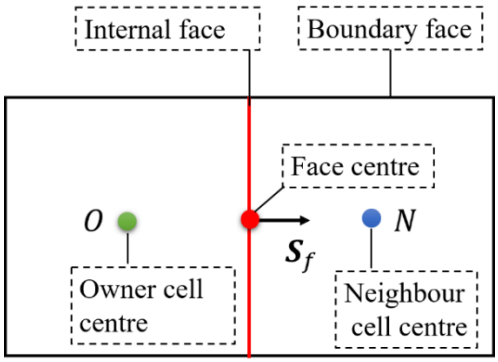

Figure 2.2. Two typical computational cells in 2D. The red line shows the internal face f.

Figure 2.2 illustrates two typical computation cells in 2D. Cell O is the owner cell and its neighbour cell N. In a structured mesh, a single control volume is bounded by faces (f) including: (i) internal faces located at the interface between two adjacent cells and (ii) boundary faces coinciding with the boundaries of the simulation domain. The cell centre or so-call computational point of each control volume is used to store variables such as the pressure and velocity fields. The position vectors $\boldsymbol{x}_O$ and $\boldsymbol{x}_f$ of cell O and internal face f with area vector $\boldsymbol{S}_f$, respectively, are defined as follows:

$$\int_{V_O} (\boldsymbol{x} - \boldsymbol{x}_O)\, dV = 0 \tag{2.2}$$

$$\int_{S_f} (\boldsymbol{x} - \boldsymbol{x}_f)\, dS = 0 \tag{2.3}$$

The face unit normal vector is defined as follows:

$$\boldsymbol{n}_f = \frac{\boldsymbol{S}_f}{|\boldsymbol{S}_f|} \tag{2.4}$$

2.2.2 Discretisation of equation

The discretisation of equation is performed by integrating and transforming Eq. (2.1) into the balance equations over the control volume V_O of the owner cell O as follows:

$$\int_t^{t+\Delta t}\left[\int_{V_O}\frac{\partial \rho\,\Phi}{\partial t}dV+\int_{V_O}\nabla\cdot(\rho\,\boldsymbol{U}\Phi)\,dV\right]dt = \int_t^{t+\Delta t}\left[\int_{V_O}\nabla\cdot(\Gamma\nabla\Phi)\,dV+\int_{V_O}S_\Phi(\Phi)dV\right]dt \tag{2.5}$$

where Δt is the time step. The discretisation of the time derivative and convection, diffusion and source terms is shown in Sections 2.2.2.3, 2.2.2.4, 2.2.2.5 and 2.2.2.6, respectively.

2.2.2.1 Face interpolation schemes

In order to construct the face centre value Φ_f from the cell centre value, face interpolation is applied, e.g. the interpolation of the fluid velocity from the cell centre to face centre for the calculation of the flux. The face flux F_{flux} is defined as follows:

$$F_{flux}=\boldsymbol{S}\cdot(\rho\boldsymbol{U})_f \tag{2.6}$$

Usually, two main schemes for the face interpolation are considered:

(i) The upwind differencing scheme [81,82]: Φ_f is determined by the direction of the flow. In order to obtain the flux through the face between cell O and N as shown in Figure 2.2, ϕ_f is defined as:

$$\Phi_f = \begin{cases} \Phi_O & if \;\; F \geq 0 \\ \Phi_N & if \;\; F < 0 \end{cases} \tag{2.7}$$

(ii) Central differencing [83] : Φ_f is determined by the interpolation of the cell centre values Φ_O and Φ_N as follows:

$$\Phi_f = f_x \Phi_O + (1 - f_x)\Phi_N \tag{2.8}$$

with

$$f_x \equiv \frac{|\boldsymbol{x}_f - \boldsymbol{x}_N|}{|\boldsymbol{x}_f - \boldsymbol{x}_N| + |\boldsymbol{x}_f - \boldsymbol{x}_P|} \tag{2.9}$$

Although the upwind differencing scheme is first order accurate, it guarantees the boundedness of the solution. On the contrary, the central differencing scheme is second order accurate but the boundedness of the solution may not be satisfied [79,83].

2.2.2.2 Gradient

In this study, Gauss integration is applied for the calculation of gradient of Φ at the cell centre. The volume integral is approximated by using the Gauss's theorem as follows:

$$\int_V \nabla \Phi dV = \int_S d\boldsymbol{S}\, \Phi \approx \sum_f \boldsymbol{S}\, \Phi_f \tag{2.10}$$

where Φ_f can be determined by either the upwind differencing or central differencing scheme. However, only the central differencing is applied in this study.

2.2.2.3 Time derivative

The time derivative in Eq. (2.1) is discretised by integrating over the control volume of the cell O. This study uses the Euler implicit method for its unconditional stability although it only first order accurate in time. Assuming the linear variation of Φ within a time step gives:

$$\int_{V_O} \frac{\partial \rho \Phi}{\partial t} dV \approx \frac{\rho_O^{n+1}\Phi_O^{n+1} - \rho_O^n \Phi_O^n}{\Delta t} V_O \tag{2.11}$$

where $\Phi_O^{n+1} \equiv \Phi(t + \Delta t)$ the new value at the next time step and $\Phi_O^n \equiv \Phi(t)$ denotes old values from the previous time step.

2.2.2.4 Convection term

The convection term $\nabla \cdot (\rho \boldsymbol{U}\Phi)$ in Eq. (2.1) is discretised by integrating over the control volume of the cell O. The volume integral is converted into a surface integral using the Gauss's theorem as follows:

$$\int_{V_O} \nabla \cdot (\rho \boldsymbol{U}\Phi)\, dV = \int_S d\boldsymbol{S} \cdot (\rho \boldsymbol{U}\Phi) \approx \sum_f \boldsymbol{S} \cdot (\rho \boldsymbol{U})_f \Phi_f \tag{2.12}$$

$$= \sum_f F_{flux} \Phi_f$$

2.2.2.5 Diffusion term

The diffusion term $\nabla \cdot (\Gamma \nabla \Phi)$ in Eq. (2.1) is discretised by a similar way to the convection term. After the integration over the control volume O, it is converted into a surface integral:

$$\int_{V_O} \nabla \cdot (\Gamma \nabla \Phi)\, dV = \int_S d\boldsymbol{S} \cdot (\Gamma \nabla \Phi) = \sum_f \Gamma_f \boldsymbol{S} \cdot \nabla_f \Phi \tag{2.13}$$

The face normal gradient $\nabla_f \Phi$ defined in Section 2.2.2.2 is a second order accurate approximation in orthogonal meshes. However, an additional correction term is added to preserve second order accuracy for non-orthogonal meshes. The full gradient approximation is determined as follows:

$$\boldsymbol{S} \cdot \nabla_f \Phi = |\boldsymbol{\Delta}| \nabla_f^{\perp} \Phi + \boldsymbol{k} \cdot (\nabla \Phi)_f \tag{2.14}$$

where $\boldsymbol{\Delta}$ and $\boldsymbol{k}$ are vectors determined by non-orthogonality treatment. However, this study only applies structured meshes so that non-orthogonality can be neglected.

2.2.2.6 Source term

The source term $S_\Phi(\Phi)$ can be explicitly computed based on the value of variable Φ, which is taken from the previous iteration, as long as the value $S_\Phi(\Phi)$ is constant or relatively small. However, when the variation in $S_\Phi(\Phi)$ is large as compared to other terms, it may cause a negative impact to the rate of convergence. In order to improve the rate of convergence, the source term is linearised using a Taylor-like series expansion and split into implicit and explicit parts as follows:

$$S_\Phi(\Phi) = \Phi S_I + S_E \tag{2.15}$$

where S_I and S_E are the implicit and explicit parts, respectively. The source term in Eq. (2.1) is then integrated over the control volume O as follows:

$$\int_{V_O} S_\Phi(\Phi)\, dV = \Phi_O S_I V_O + S_E V_O \tag{2.16}$$

2.2.2.7 Boundary conditions

A boundary element is located at a boundary patch and has at least one face expressed as the boundary face as shown in Figure 2.2. Boundary conditions must be specified in order to connect the boundary element with the mathematical model of the continuum problems. Each boundary condition presents a physical meaning described mathematically, crucial for the accuracy of CFD solvers. The most widely used

boundary conditions can be divided into two groups: Dirichlet and Neumann boundary conditions. Dirichlet boundary conditions present a specified value so-called *fixed value* whilst Neumann boundary conditions specify the flux so-called *fixed gradient* or *zero gradient*. They are described as follows:

Fixed value: Φ_B at the boundary is set by a fixed value so that the value of the boundary face is equal to Φ_B. When the face gradient $\nabla_f \Phi$ is required, it is determined by the value at the boundary face and cell centre as follows:

$$\boldsymbol{S} \cdot \nabla_f \Phi = |\mathbf{S}| \frac{\Phi_B - \Phi_O}{|\boldsymbol{d}_B|} \tag{2.17}$$

where $\boldsymbol{d}_B$ is the vector between the cell centre O and the centre of the boundary face normal to the boundary face.

Fixed gradient: a flux for Φ is specified at the boundary. Φ_f on the boundary face is extrapolated using the face normal gradient $g_B = \nabla_f^{\perp} \Phi$ and the normal vector between the cell centre of the owner cell and the boundary face as follows:

$$\Phi_f = \Phi_O + |\boldsymbol{d}_B| g_B \tag{2.18}$$

When the face gradient $\nabla_f \Phi$ is required, it is determined by substituting the face normal gradient g_B as follows:

$$\boldsymbol{S} \cdot \nabla_f \Phi = |\mathbf{S}| g_B \tag{2.19}$$

Zero gradient: when zero gradient boundary is described at the boundary, the discretisation is similar to the fixed gradient boundary condition with $g_B = 0$.

2.2.3 Temporal discretisation

The discretisation of the volume integrals in the standard transport equation is presented in Section 2.2.2. Using equations (2.11), (2.12), (2.13) and (2.16), Eq. (2.5) can be written as follows:

$$\int_t^{t+\Delta t} \left[\rho \frac{\Phi_O^{n+1} - \Phi_O^n}{\Delta t} V_O + \sum_f F_{flux} \Phi_f \right] dt = \int_t^{t+\Delta t} \left[\sum_f \Gamma_f \boldsymbol{S} \cdot \nabla_f \Phi + \Phi_O S_I V_O + S_E V_O \right] dt \tag{2.20}$$

The temporal variations of Φ_O, face values and gradients are expressed by either the old value Φ_O^n or the new value Φ_O^{n+1}. By taking the old value, Euler explicit method applies explicit discretisation of the spatial terms:

$$\Phi_O = \Phi_O^n \tag{2.21}$$

$$\Phi_f = \Phi_f^n \tag{2.22}$$

$$\boldsymbol{S} \cdot \nabla_f \Phi = \boldsymbol{S} \cdot \nabla_f \Phi^n = |\boldsymbol{\Delta}| \nabla_f^{\perp} \Phi^n + \mathbf{k} \cdot (\nabla \Phi^n)_f \tag{2.23}$$

On the other hand**,** Euler implicit method applies implicit discretisation of the spatial terms by using new values Φ_O^{n+1}:

$$\Phi_O = \Phi_O^{n+1} \tag{2.24}$$

$$\Phi_f = \Phi_f^{n+1} \tag{2.25}$$

$$\boldsymbol{S} \cdot \nabla_f \Phi = \boldsymbol{S} \cdot \nabla_f \Phi^{n+1} = |\boldsymbol{\Delta}| \nabla_f^{\perp} \Phi^{n+1} + \mathbf{k} \cdot (\nabla \Phi^n)_f \tag{2.26}$$

Euler implicit method is first order accurate in time and guarantees the boundedness of the solution. In addition, it is unconditionally stable. However, the non-orthogonal correction must be treated explicitly in order to satisfy the boundedness when unstructured meshes are applied. In this study, Euler implicit method is used exclusively and the final discretised standard transport equation now reads:

$$\rho_O \frac{\Phi_O^{n+1} - \Phi_O^n}{\Delta t} V_O + \sum_f F \Phi_{f(F,S)}^{n+1} = \sum_f \Gamma_f \boldsymbol{S} \cdot \nabla_f \Phi^{n+1} + S_I V_O \Phi_O^{n+1} + S_E V_O \tag{2.27}$$

2.3 Summary

Applying the FVM, the transport equation for the fluid phase is transformed into discrete algebraic equations which are then solved numerically. When the transport equation is discretised, the spatial discretisation is applied to split the simulation domain into small computational cells. The discretisation is obtained by integrating and transforming the transport equation into the balance equations over the control volume. Euler implicit method is used for the temporal discretisation in this study for its unconditional stability.

Chapter 3

Discrete Element Method

3.1 Introduction

This chapter introduces the fundamental principle of Discrete Element Method (DEM) as a part of the resolved CFD–DEM model. A general introduction of DEM is then presented in Section 3.2. The motion of discrete particle is simulated by the soft-sphere model using a non-linear spring model as shown in Sections 3.3.1 and 3.3.2. The critical simulation time step for DEM as well as the integration scheme applied to solve the equation of motion of the particle phase are introduced in Sections 3.3.3 and 3.3.4, respectively.

3.2 Discrete Element Method (DEM)

Discrete Element Method (also known as Distinct Element Method) is widely used to study the dynamical behaviour of granular flow. In DEM, the position and velocity of individual particles are calculated by solving the Newton's second law of motion. DEM accounts for particle collisions by using either hard-sphere model firstly proposed by Alder and Wainwright [84] for molecular dynamic modelling and later by Campbell and Brennen [85] for granular simulation, or the soft-sphere model proposed for DEM by Cundall and Strack [4].

In the hard-sphere model, it is assumed that the particles are rigid and the collisions are instantaneous as illustrated in Figure 3.1(a). In addition, the simulation time step is defined by the time between particle collisions. Hence, the dynamic behaviour of granular flow can be described solely by binary collisions. The hard-sphere model is simple and only suitable for the study of dilute flow where the collision frequency is low.

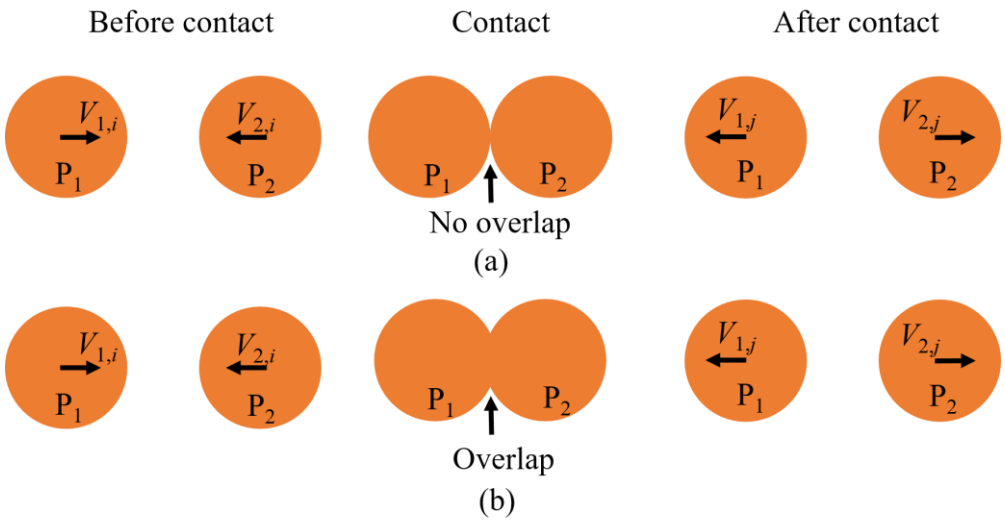

Figure 3.1. Illustration of (a) hard-sphere model and (b) soft-sphere model. $V_{1,i}$ and $V_{2,i}$ are the velocities of particles before contact and $V_{1,j}$ and $V_{2,j}$ are the velocities of particles after contact.

In the soft-sphere model, it is assumed that the particles remain geometrical rigid except for a finite contact duration where that becomes deformable as illustrated in

Figure 3.1(b). In contrast to the hard-sphere model, the soft-sphere model can account more than two particles colliding with one another. Therefore, the soft-sphere model is applicable to the study of dense system in which particle deformation and complexity of frictional forces during contact cannot be neglected. Since this study simulates various systems, i.e. from dilute to relatively dense flows, the soft-sphere model is chosen in this study.

The generic translational and rotational motions of a particle i are governed by the Newton's second law of motion as follows:

$$m_i \dot{\boldsymbol{v}}_i = \sum_j \boldsymbol{F}_{Ci} + \boldsymbol{F}_{fi} + \boldsymbol{F}_{Gi} \tag{3.1}$$

$$I_i \dot{\boldsymbol{\omega}}_i = \sum_j \boldsymbol{T}_{Ci} + \boldsymbol{T}_{fi} \tag{3.2}$$

where m is the particle mass, I is the particle moment of inertia, $\boldsymbol{v}$ and $\boldsymbol{\omega}$ are the translational and angular velocities of the particle, respectively, $\boldsymbol{F}_C$ is the contact force, $\boldsymbol{F}_f$ is the force exerted on the particle (i.e. hydrodynamic force, surface tension along with the three-phase contact line and buoyancy force), $\boldsymbol{F}_{Gi} = m_i \boldsymbol{g}$ is the force due to gravity and $\boldsymbol{g}$ is the gravitational acceleration, $\boldsymbol{T}_C$ is the contact torque and $\boldsymbol{T}_f$ is the torque exerted on the particle due to fluid force. Solutions of Eqs. (3.1) and (3.2) are given by the soft-sphere model described in the next section.

3.3 Soft-sphere model

The soft-sphere model was first proposed by Cundall and Strack [4]. The particle-particle collisions in the soft-spring model are modelled using springs, dash-pots and a frictional slider as shown in Figure 3.2. When particles are in contact, the contact forces due to the deformation of particle surfaces are resolved into a normal force and a tangential force.

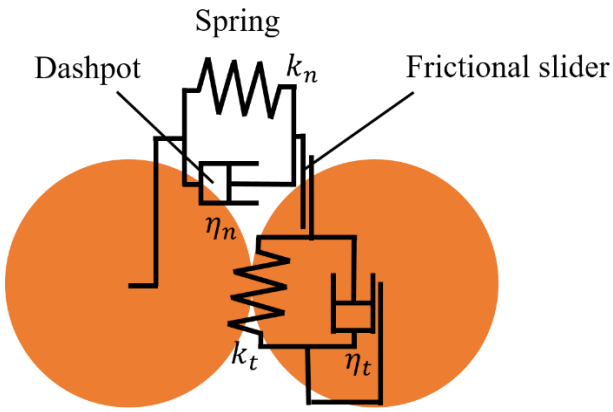

Figure 3.2. Schematic diagram of the soft-sphere model.

The normal force acts from the centre of one particle to that of the other and has two main contributions: the elastic repulsion force and the energy dissipation described by the spring and dashpot. The normal force can be defined by either a linear-spring model or a non-linear spring model. In the linear spring model, the elastic repulsion force is linearly proportional to the particle displacement. On the other hand, the elastic repulsion force is proportional to the particle displacement to the power of 3/2

according to the well-known non-linear Hertzian contact theory [86]. Although the linear spring model is simple since it has analytical solution of the collision parameters, it does not accurately describe individual collision forces between spherical particles [87,88]. In contrast to the linear spring model, the non-linear spring model can be described by the non-linear stiffness spring coefficient estimated according to the material properties, i.e. Young's modulus and Poisson's coefficient. Hence, DEM simulations using the non-linear spring model can accurately capture the dynamic behaviour of colliding particles in various systems. This study applies the non-linear spring model to the contact solution. The normal force $\boldsymbol{F}_{Cnij}$ exerted on particle i when it comes into contact with particle j is defined as follows:

$$\boldsymbol{F}_{Cni,j} = \left(-k_n \delta_n^{3/2} - \eta_n \boldsymbol{v}_{ni,j} \cdot \boldsymbol{e}_{ni,j}\right)\boldsymbol{e}_{ni,j} \tag{3.3}$$

where k_n, δ_n, η_n are the stiffness of the spring, the particle displacement and the damping coefficient of the dashpot in the normal direction, respectively. $\boldsymbol{v}_{ni,j}$ is the relative velocity of particle i to particle j in the normal direction. $\boldsymbol{e}_{ni,j}$ is the unit vector from the centre of particle i to particle j.

The tangential force, is perpendicular to the normal direction, presents either the static friction or the dynamic force described by the spring-dashpot or the frictional slider, respectively. The tangential force exerted on particle i is calculated as follows:

$$\boldsymbol{F}_{Cti,j} = \min\left[-k_t\delta_t\boldsymbol{e}_{tij} - \eta_t\boldsymbol{v}_{ti,j} - \mu_s\left|\boldsymbol{F}_{Cni,j}\right|\boldsymbol{e}_{ti,j}\right] \tag{3.4}$$

where μ_s is the sliding friction coefficient. k_n, δ_t and η_t are the stiffness of the spring, the particle displacement and the damping coefficient of the dashpot in the tangential direction, respectively. The function min[*A*, *B*] selects the smaller value between *A* and *B*. $\boldsymbol{v}_{ti,j}$ is the relative tangential velocity at the contact surface and is calculated from the sum of the translational and rotational velocities as follows:

$$\boldsymbol{v}_{ti,j} = \boldsymbol{v}_{ni,j} - \left(\boldsymbol{v}_{ni,j}\cdot\boldsymbol{e}_{ni,j}\right)\boldsymbol{e}_{ni,j} + r_p\left(\boldsymbol{\omega}_i + \boldsymbol{\omega}_j\right)\times\boldsymbol{e}_{ni,j} \tag{3.5}$$

The unit vector in the tangential direction is calculated based on the relative tangential velocity as follows:

$$\boldsymbol{e}_{ti,j} = \frac{\boldsymbol{v}_{ti,j}}{\left|\boldsymbol{v}_{ti,j}\right|} \tag{3.6}$$

When there are multiple collisions in the system, particle i can collide with more than two particles simultaneously. The total collision force and torque exerted on particle i is defined as follows:

$$F_{Ci} = \sum_j\left(\boldsymbol{F}_{Cni,j} + \boldsymbol{F}_{Cti,j}\right) \tag{3.7}$$

$$T_{Ci} = \sum_j\left(r_p\boldsymbol{e}_{ni,j}\times\boldsymbol{F}_{Cti,j} - \mu_s\left|\boldsymbol{F}_{Cni,j}\right|r_p\frac{\boldsymbol{\omega}_{pi}}{\left|\boldsymbol{\omega}_{pi}\right|}\right) \tag{3.8}$$

3.3.1 Elastic repulsion force

According to the well-known Hertzian contact theory for isotropic elastic particles with perfectly smooth surfaces proposed by Goldsmith [86], the elastic repulsion force is proportional to the deformation to the power of $3/2$ as shown in Eq. (3.3). The stiffness of the spring in the normal direction is calculated as follows:

$$k_n = \frac{\sqrt{2r_i}E_i}{3(1-\Gamma^2)} \tag{3.9}$$

where E_i is the Young's modulus and Γ is the Poisson's ratio of the particle. The stiffness of the spring in the tangential direction is calculated by Mindlin's theory [89] for non-slip case as follows:

$$k_t = \frac{2\sqrt{2r_i}G_i}{2-\Gamma}\delta_n^{1/2} \tag{3.10}$$

In the case of contact between the particle and the wall, k_t is defined as follows:

$$k_t = \frac{8\sqrt{2r_i}G_i}{2-\Gamma}\delta_n^{1/2} \tag{3.11}$$

where G_i is the shear modulus of the particle and it is calculated based on the Young's modulus and Poisson's ratio as follows:

$$G_i = \frac{E_i}{2(1-\Gamma)} \tag{3.12}$$

3.3.2 Damping coefficient

Based on the non-linear spring model, Tsuji et al. [90] proposed a correlation to express the damping coefficient of the dashpot. Considering a particle collides with a wall (or another particle) in the normal direction as illustrated in Figure 3.3, the equation of motion for the particle can be described as follows:

$$m_i\ddot{x} + \eta_n\dot{x} + k_n x^{3/2} = 0 \tag{3.13}$$

The coefficient of restitution of the particle e_p is written as follows:

$$e_p = -\frac{v_{ini}}{v_{out}} \tag{3.14}$$

where v_{ini} and v_{out} are the particle velocities before and after collision. In general, the coefficient of restitution has a constant value regardless of the impact velocity [90] so that e_p should be independent of the combination of m_i, k_n, and η_n. Tsuji et al. [90] "heuristically" confirmed that for η_n described as:

$$\eta_n = C_e(m_i k_n)^{\frac{1}{2}} x^{\frac{1}{4}} \tag{3.15}$$

where C_e is an empirical constant related to the coefficient of restitution.

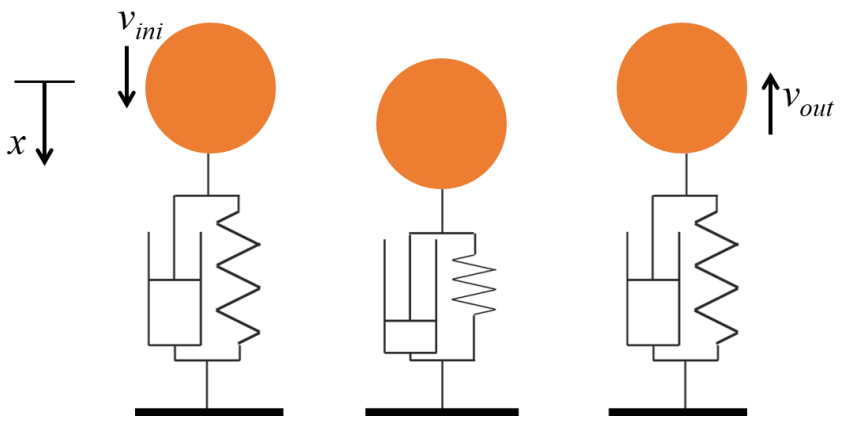

Figure 3.3. Spring-dashpot-mass model in one-dimension.

Substituting Eq. (3.15) in Eq. (3.13), and eliminating time t, Eq. (3.13) can be rewritten as follows:

$$v\frac{dv}{dx} + C_e\left(\frac{k_n}{m_i}\right)^{1/2} x^{1/4}v + \frac{k_n}{m_i}x^{3/4} = 0 \tag{3.16}$$

Here $v = \frac{dx}{dt}$. The non-dimensional velocity $\hat{v}$ and displacement $\hat{x}$ are defined as follows:

$$\hat{v} = v/v_{ini} \tag{3.17}$$

$$\hat{x} = x\left(\frac{5m_i v_{ini}^2}{4k_n}\right)^{-\frac{2}{5}} \tag{3.18}$$

Using the defined non-dimensional variables above, Eq. (3.16) is rewritten in the as follows:

$$\hat{v}\frac{d\hat{v}}{d\hat{x}} + C_e\left(\frac{5}{4}\right)^{1/2}\hat{x}^{1/4}\hat{v} + \frac{5}{4}\hat{x}^{3/4} = 0 \tag{3.19}$$

Eq. (3.19) is only dependent on C_e. Tsuji et al. [90] found that the coefficient of restitution e_p depends only on the value of C_e. Eq. (3.15) is rewritten with the displacement δ_n as follows:

$$\eta_n = C_e(m_i k_n)^{\frac{1}{2}}\delta_n^{\frac{1}{4}} \tag{3.20}$$

Regarding the damping coefficient in the tangential direction η_t, it is assumed that η_t is identical to η_n since it is difficult to evaluate η_t (Tsuji et al. [90]).

3.3.3 Critical time step for DEM

In DEM simulation with particle-particle interaction, stability of calculation is greatly affected by the time step during the numerical integration. In general, the smaller the time step gives the more stable the calculation. However, the time step should be as large as possible in order to save calculation cost. Two approaches are found in the literature to determine the critical time step for DEM. The first approach is based on the oscillation period of the mass-spring-dashpot system as proposed by Cundall and Strack [4] for the linear spring model. The second approach is based on

Rayleigh wave speed. In the simulation, it is assumed that all of the energy is transferred by the Rayleigh waves [91]. Based on the non-linear spring model, Li et al. [92] investigated the contact mechanics of non-adhesive particle through a comparative numerical-experimental study of the sandpile problem. The expression for the Rayleigh time step is proposed as follows [92]:

$$\Delta t = \frac{f\pi R}{0.1631\Gamma + 0.8766}\sqrt{\rho/G_i} \tag{3.21}$$

where R is the average particle radius and f is the safety factor. This study follows the second approach with a safety factor of 0.1 in Eq. (3.21).

3.3.4 Integration scheme

In order to solve the Newton's second law of motion numerically, the velocities and positions of particles are computed by an integration scheme. Various integration schemes can be applied such as symplectic Euler, position Verlet and velocity Verlet. In the symplectic Euler scheme, a first-degree Taylor approximation is applied to derive the first derivative $f'(t)$. The standard Euler method based on the forward difference approximation is used for the first derivative in order to solve for the velocities and positions of particles at the next time step. The position Verlet (also known as the basic Verlet method) is based on the central difference approximation. The first and second derivatives are expressed by a Taylor polynomial of degree two and three, respectively. The position Verlet scheme is a second order integrator and more stable than the

symplectic Euler scheme. However, the velocities are not provided at the next time step [93]. In order to improve the position Verlet scheme, the modified position Verlet scheme can be used and is called as the velocity Verlet scheme. The velocity Verlet scheme is also widely used in the literature [94]. This study also applies the velocity Verlet scheme to solve the equation of motion for particles

The positions $\boldsymbol{x}_{t+1}$ and velocities $\boldsymbol{v}_{t+1}$ calculated by the velocity Verlet scheme at the next time step are computed as follows:

$$\boldsymbol{x}_{t+1} = \boldsymbol{x}_t + \boldsymbol{v}_t \Delta t + \frac{1}{2}\dot{\boldsymbol{v}}_t \Delta t^2 \tag{3.22}$$

$$\boldsymbol{v}_{t+1} = \boldsymbol{v}_t + \dot{\boldsymbol{v}}_t \Delta t + \frac{1}{2}\ddot{\boldsymbol{v}}_t \Delta t^2 \tag{3.23}$$

where $\boldsymbol{x}_t$ and $\boldsymbol{v}_t$ are the position vector and the translational velocity at the previous time step, respectively. $\ddot{\boldsymbol{v}}_t$ is defined as follows:

$$\ddot{\boldsymbol{v}}_t = \frac{\dot{\boldsymbol{v}}_{t+1} - \dot{\boldsymbol{v}}_t}{\Delta t} \tag{3.24}$$

Substituting Eq. (3.24) into Eq. (3.23), the translational velocity $\boldsymbol{v}_{t+1}$ at the next time step is finally determined as follows:

$$\boldsymbol{v}_{t+1} = \boldsymbol{v}_t + \frac{1}{2}(\dot{\boldsymbol{v}}_t + \dot{\boldsymbol{v}}_{t+1})\Delta t \tag{3.25}$$

The angular velocity $\boldsymbol{\omega}_{t+1}$ of the particle can be defined in the same manner as Eq. (3.25):

$$\boldsymbol{\omega}_{t+1} = \boldsymbol{\omega}_{\mathrm{t}} + \frac{1}{2}(\dot{\boldsymbol{\omega}}_t + \dot{\boldsymbol{\omega}}_{t+1})\Delta t \tag{3.26}$$

In order to evaluate the translational and angular velocities in Eqs. (3.25) and (3.26), a predictor-corrector scheme is applied. The predictor calculates the position $\boldsymbol{x}_{t+1}$ as shown in Eq. (3.22) and predicts the translational velocity $\boldsymbol{v}_{t+1}^{pr}$ and angular velocity $\boldsymbol{\omega}_{t+1}^{pr}$ as follows:

$$\boldsymbol{v}_{t+1}^{pr} = \boldsymbol{v}_t + \frac{1}{2}\dot{\boldsymbol{v}}_t \Delta t \tag{3.27}$$

$$\boldsymbol{\omega}_{t+1}^{pr} = \boldsymbol{\omega}_{\mathrm{t}} + \frac{1}{2}\dot{\boldsymbol{\omega}}_t \Delta t \tag{3.28}$$

The new acceleration is then evaluated based on the predicted velocities and position. The translational velocity $\boldsymbol{v}_{t+1}$ and angular velocity $\boldsymbol{\omega}_{t+1}$ at the next time step are finally calculated as follows:

$$\boldsymbol{v}_{t+1} = \boldsymbol{v}_{t+1}^{pr} + \frac{1}{2}\dot{\boldsymbol{v}}_{t+1} \Delta t \tag{3.29}$$

$$\boldsymbol{\omega}_{t+1} = \boldsymbol{\omega}_{t+1}^{pr} + \frac{1}{2}\dot{\boldsymbol{\omega}}_{t+1} \Delta t \tag{3.30}$$

3.4 Summary

The motion of individual particles is solved numerically by DEM. The soft-sphere model is used for DEM simulation in this study due to its simplicity and efficiency. The particle-particle collision forces are modelled by using springs, dash-pots and a frictional slider. A non-linear spring model based on the well-known Hertzian contact theory [86] is applied for the normal force whilst the Mindlin model [89] is used for the tangential force. The Rayleigh time step with a safety factor of 0.1 is applied in this study to ensure to the stability of simulation. The velocity Verlet method, a second order integrator, is applied for the integration scheme in this study.

Chapter 4

Fluid-Solid Two-Phase Flows with Volume Penalisation Method

4.1 Introduction

The resolved CFD–DEM coupling model using the VP method with the optimal permeability for the study of fluid-solid two-phase flows is presented in this chapter. A smooth mask function is used to avoid sharp transition between the solid (particle) and fluid domains that may cause numerical oscillation with moving particles. Optimal permeability governed by a particle-fluid interface thickness is employed to reduce the model error associated with the VP method.

In order to investigate the influence of particle-fluid interface thickness governing the optimal permeability on the simulation accuracy, three types of simulations are performed with different interface thicknesses and resolutions: the flow past a single stationary particle, the flow through a periodic array of particles and a particle approaching to a plane wall, as shown in Section 4.5. Through these simulations, the resolved CFD–DEM with the VP method is also validated by comparing the simulation results with both theoretical and empirical data. The resolved CFD-DEM model is then applied to predict of relative viscosity of suspension and analyse the behaviour of the uniform density and binary-mixture fluidised beds as shown in Section 4.6.

4.2 Governing equations

4.2.1 CFD governing equations

The fluid is assumed to be isothermal and incompressible. The continuity and momentum equations for the fluid phase are given as follows:

Continuity equation:

$$\nabla \cdot \boldsymbol{U} = 0 \tag{4.1}$$

Momentum equation:

$$\frac{\partial}{\partial t}(\rho \boldsymbol{U}) + \nabla \cdot (\rho \boldsymbol{U}\boldsymbol{U}) = -\nabla p + \nabla \cdot \boldsymbol{\tau} + \boldsymbol{f}_{VP} + \rho \boldsymbol{g} \tag{4.2}$$

where t is the time, ρ is the fluid density, $\boldsymbol{U}$ is the velocity, p is the pressure, $\boldsymbol{\tau}$ is the viscous stress tensor, $\boldsymbol{f}_{VP}$ is the penalty term and $\boldsymbol{g}$ is the gravitational acceleration. The fluid applied in this work is Newtonian and the viscous stress tensor is described by the following expression:

$$\boldsymbol{\tau} = \mu \left(\nabla \boldsymbol{U} + \nabla \boldsymbol{U}^{\mathrm{T}}\right) \tag{4.3}$$

where μ is the fluid dynamic viscosity and the superscript T indicates the transposition of a tensor.

4.2.2 DEM governing equations

The translational and rotational motions of a particle i are governed by the Newton's second law of motion as follows:

$$m_i \dot{\boldsymbol{v}}_i = \sum_j \boldsymbol{F}_{Cij} + \boldsymbol{F}_{VPi} + \boldsymbol{F}_{Bi} + \boldsymbol{F}_{Gi} \tag{4.4}$$

$$I_i \dot{\boldsymbol{\omega}}_i = \sum_j \boldsymbol{T}_{Cij} + \boldsymbol{T}_{VPi} \tag{4.5}$$

where $\boldsymbol{F}_{VP}$ is the hydrodynamic force, $\boldsymbol{F}_B$ is the buoyancy force, $\boldsymbol{F}_G = m\boldsymbol{g}$ is the gravitational force, $\boldsymbol{T}_C$ is the contact torque, $\boldsymbol{T}_{VP}$ is the hydrodynamic torque. The contact force is modelled by the non-linear spring-dashpot model as proposed by Tsuji et al. [90]: the normal and tangent force is calculated by the Hertizian contact theory [95] and the Mindlin model [89], respectively, as shown in Section 3.3.2.

The fluid force and torque acting on the particle due to the penalty term is determined by integrating the counteracting force of the penalty force and its torque, respectively, over the particle volume as follows:

$$\boldsymbol{F}_{VPi} = -\int_{V_i} \boldsymbol{f}_{VP}\, dV \tag{4.6}$$

$$\boldsymbol{T}_{VPi} = -\int_{V_i} \boldsymbol{r} \times \boldsymbol{f}_{VP}\, dV \tag{4.7}$$

where V is the volume of the particle and $\boldsymbol{r}$ is the relative position from the center of gravity of the particle.

The buoyancy force is also not included in $\boldsymbol{F}_{VP}$ since $\rho\boldsymbol{g}$ in Eq. (4.2) is included in the particle domain, which compensates the hydrostatic pressure force around the particle. Therefore, the buoyancy force is calculated separately as [16]:

$$\boldsymbol{F}_{Bi} = -\int_{V_i} \chi\rho\boldsymbol{g}\, dV \tag{4.8}$$

4.3 Optimal permeability

The VP method considers the penalty term in the solid phase where fluid is allowed to flow through the solid body with a small permeability aiming to yield no-slip boundary condition at solid surface. Angot et al. [39] interpreted the Darcy law of the fluid flow in the solid domain considered as the porous media. The small permeability is applied in the solid domain to enforce the fluid velocity approaching the solid velocity. In order to penalise the no-slip boundary condition on the surface of solid phase, the penalty term $\boldsymbol{f}_{VP}$ is added into the fluid momentum equation as shown in Eq. (4.2), it is defined as follows:

$$\boldsymbol{f}_{VP} = \frac{\chi\rho}{\eta}(\boldsymbol{U}_{solid} - \boldsymbol{U}) \tag{4.9}$$

where η is the permeability. χ is the mask function applied to activate or terminate the penalty term in the solid and fluid domains, respectively. $\boldsymbol{U}_{solid}$ is the solid velocity determined by the particle velocity as follows:

$$\boldsymbol{U}_{solid} = \boldsymbol{v}_p + \boldsymbol{\omega}_p \times \boldsymbol{r} \tag{4.10}$$

where $\boldsymbol{r}$ is the relative position from the centre of gravity of the particle and $\boldsymbol{v}_p$ and $\boldsymbol{\omega}_p$ are the translational and angular velocities of the particle, respectively.

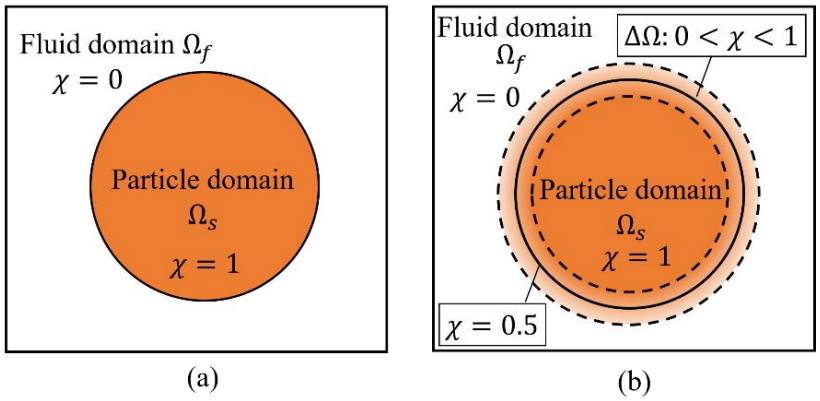

Figure 4.1 The mask function distinguishes the particle domain Ω_s and fluid domain Ω_f. (a) the conventional (discontinuous) mask function and (b) the smooth mask function induces a smooth interface region $\Delta\Omega$ (bounded by the dashed lines) while the solid line illustrates the real particle surface ($\chi = 0.5$).

As seen in Figure 4.1(a), the discontinuous mask function χ applied in the conventional VP method sharply divides the simulation domain into the fluid domain Ω_f and the solid domain Ω_s in which $\chi = 0$ and 1, respectively. On the other hand, the value of the smooth mask function varies rapidly yet continuously from 0 to 1 over the finite interface region $\Delta\Omega$ as illustrated in Figure 4.1(b). The hyperbolic tangent function is used for the mask function in this study:

$$\chi = \frac{1}{2}\left\{1 - \tanh\left(\frac{\sigma}{\delta}\right)\right\} \tag{4.11}$$

where σ is the signed distance (positive in the fluid domain and negative in the solid domain) from the real particle surface and δ is the thickness parameter. The resultant mask function is shown in Figure 4.2. The interface thickness is proportional to the thickness parameter.

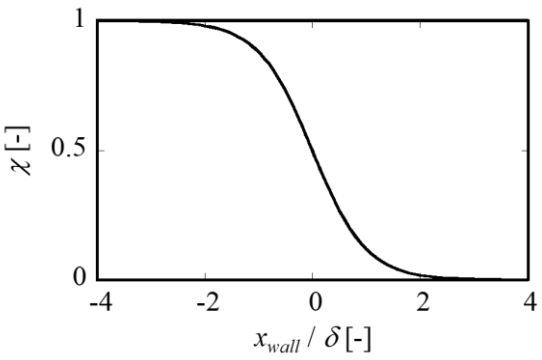

Figure 4.2. Smooth mask function χ as a function of the signed distance function σ normalised by the thickness parameter δ .

The permeability η is determined based on the work by Hester et al [43], which can eliminate the leading order model error based on the multiple-scales matched-asymptotics analysis. This is called optimal permeability in this work. This section only highlights the key idea for the derivation of the optimal permeability here and the readers may refer to the literature [43] for more details. First, the following dimensionless parameters are defined:

$$\mathrm{Re} = \frac{U_c L_c}{\nu} \tag{4.12}$$

$$\zeta = \frac{\eta U_c}{L_c} \tag{4.13}$$

where U_c and L_c are the characteristic velocity and length scales, respectively, ν is the kinematic viscosity of the fluid, Re is the Reynolds number, which characterises the ratio of viscous and inertial time scales and ζ is the dimensionless damping time scale, which characterises the ratio of dimensional damping time (also known as permeability η) and inertial time scales. ζ can be written as follows:

$$\zeta = \mathrm{Re}\varepsilon^2 \tag{4.14}$$

where $\varepsilon = \frac{\sqrt{\nu\eta}}{L_c}$ is the dimensionless damping length scale, which comes from balancing the viscous and damping. The continuity and momentum equations are then rewritten in the dimensionless form as:

$$\nabla^* \cdot \boldsymbol{U}^* = 0 \tag{4.15}$$

$$\frac{\partial \boldsymbol{U}^*}{\partial t^*} + \boldsymbol{U}^* \cdot \nabla^* \boldsymbol{U}^* = -\nabla^* p^* + \frac{1}{\mathrm{Re}} \nabla^{*2} \boldsymbol{U}^* + \frac{\chi}{\zeta} (\boldsymbol{U}^*_{solid} - \boldsymbol{U}^*) + \boldsymbol{g}^* \tag{4.16}$$

where the superscript $*$ indicates the dimensionless variables. Now, a signed distance coordinate system is introduced. The dimensionless signed distance is first defined as:

$$\sigma^* = \sigma / L_c \tag{4.17}$$

The solid surface is then parametrised by some orthogonal surface coordinates, say s_1 and s_2. This signed distance coordinate system allows to define the components in the normal and tangential directions of any quantity and differential operator. For example, the velocity is decomposed as follows:

$$\boldsymbol{U}^* = \boldsymbol{U}^*_\sigma + \boldsymbol{U}^*_\perp \tag{4.18}$$

where the subscripts σ and $\perp$ denote the normal and tangential components, respectively. In the interface region, the dimensionless signed distance is rescaled as:

$$\xi = \sigma^* / \varepsilon \tag{4.19}$$

Using on the asymptotic matching, the leading order normal velocity is zero and the momentum equation takes the following form in terms of the tangential velocity:

$$\left(\chi - \partial_\xi^2\right) U_{\perp 0}^*(\xi) = 0 \tag{4.20}$$

where the subscript 0 denotes the leading order, $\boldsymbol{U}_{\perp 0}^* = U_{\perp 0}^*(\xi)\boldsymbol{t}_\perp$, $\boldsymbol{t}_\perp$ is the tangential direction vector and the operator ∂_ξ is the partial derivative in the rescaled normal direction. The physically acceptable solutions of Eq. (4.20) in the limiting cases are given as:

$$U_{\perp 0}^*(\xi \to -\infty) \sim a e^{\xi} \tag{4.21}$$

$$U_{\perp 0}^*(\xi \to +\infty) \sim b(\xi - \ell^*) \tag{4.22}$$

where a, b and ℓ^* are the integral constants. ℓ^* is called the displacement length and defined as the leading order model error since it does not appear in the true no-slip boundary condition. The following mask function can eliminate the displacement length:

$$\chi = \frac{1}{2}\left\{1 - \tanh\left(\frac{2\xi}{2.648228}\right)\right\} \tag{4.23}$$

Although the mask function written Eq. (4.23) is considered as the optimal mask function in the study of Hester et al. [43], this study derives the optimal permeability based on Eqs. (4.11), (4.14), (4.17), (4.19) and (4.23) as follows:

$$\eta \approx 0.57 \frac{\delta^2}{\nu} \tag{4.24}$$

The unique point of the optimal permeability written in Eq. (4.24) is that it is a function of only two parameters: the thickness parameter δ and the fluid kinematic viscosity ν. The resolved CFD-DEM developed with the smooth mask function and the optimal permeability as shown in Eqs. (4.11) and (4.24), respectively, is simple in terms of implementation. When the optimal permeability is applied to the 2D flow between parallel plates, the velocity profile is in good agreement with the theoretical parabola as shown in Figure 4.3.

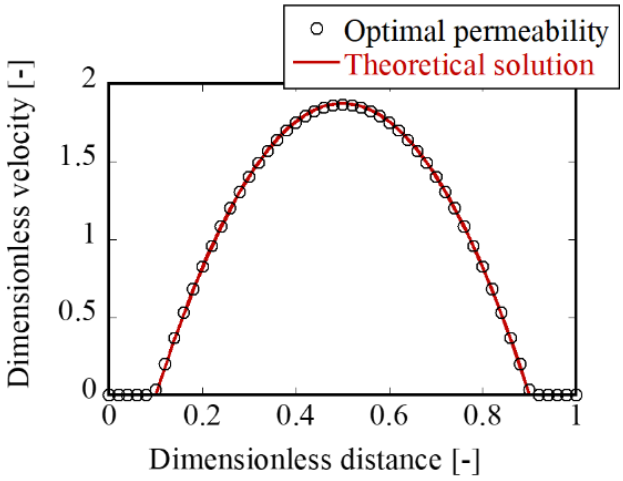

Figure 4.3. Velocity profile of the flow between two parallel plates. Re $= 0.5$ and the thickness parameter is chosen as 80 times smaller than the distance between two plates.

4.4 Numerical solution procedure

The resolved CFD–DEM simulation for particle-fluid two-phase flow is implemented by open-source CFD and DEM solvers: OpenFOAM for the fluid phase and LIGGGTHS for the particle phase. OpenFOAM uses the FVM to discretise the

continuity and momentum equations although the VP method is a family of the continuous forcing IB method and any discretisation method is applicable. The PIMPLE algorithm [96], which is the combination of PISO [97] (Pressure Implicit Split Operator) and SIMPLE [76] (Semi-Implicit Method for Pressure Linked Equations) algorithms, is used for the pressure-velocity coupling. The equation of motion for particles is solved by using the velocity Verlet algorithm. The simulation time step for CFD is kept to be smaller than the optimal permeably calculated by Eq. (4.24) while the time step for DEM is determined based on the Rayleigh time [92] with a safety factor of 0.1 as shown in Section 3.3.3. It only requires simple steps to couple the CFD and DEM solvers. A solution flow chart can be found in Figure 4.4.

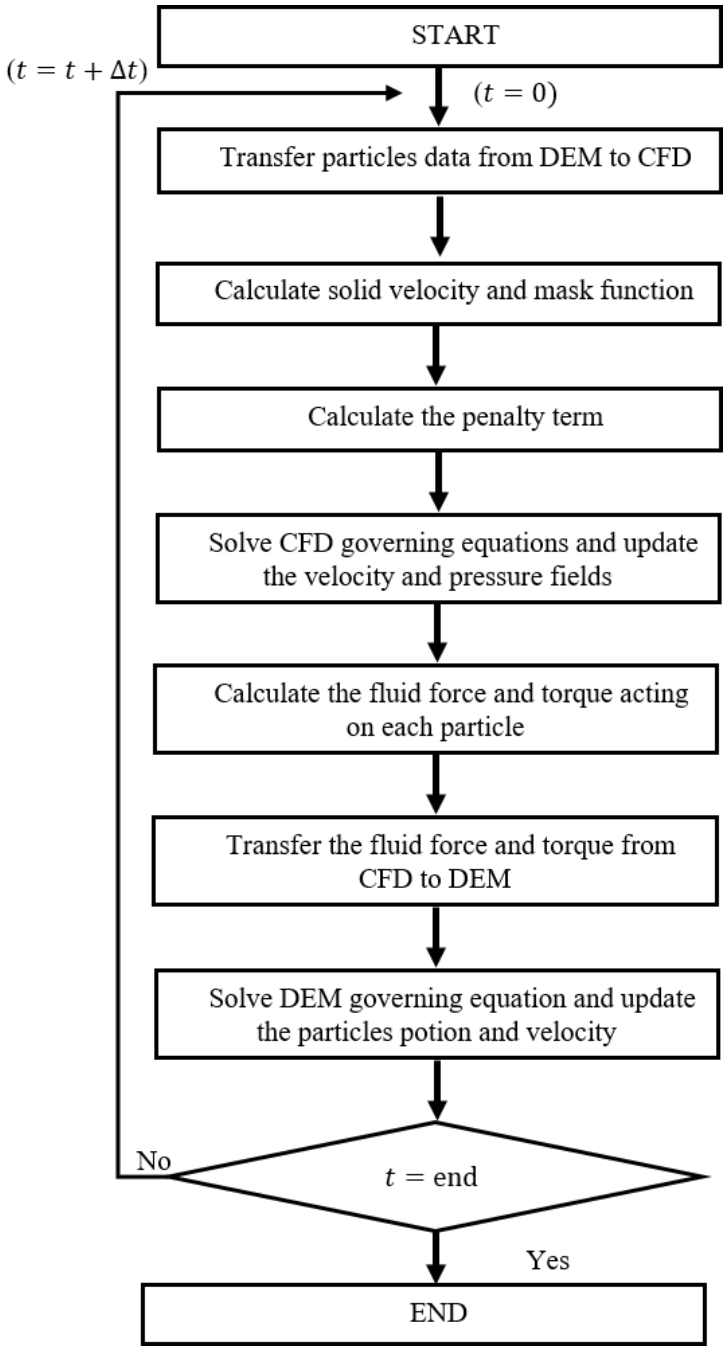

Figure 4.4. Numerical solution flow chart of the resolved CFD–DEM model for fluid-solid two-phase flows.

4.5 Model validations

4.5.1 Flow past a stationary single particle

This work focuses on the development of the resolved CFD–DEM model with the VP method for particulate systems. The first validation test presented is a stationary single particle with diameter d_p placed in a uniform flow. As depicted in Figure 4.5, the particle-fluid interface is smeared over a finite thickness by controlling the thickness parameter δ as $d_p/20$, $d_p/40$, $d_p/80$ and $d_p/160$.

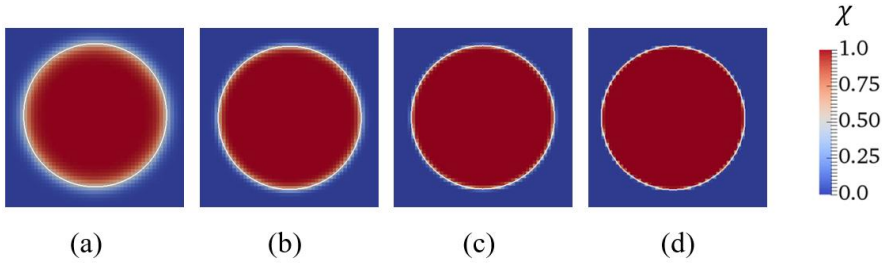

Figure 4.5. The mask function with different thickness parameter δ; (a) $\delta = d_p/20$, (b) $\delta = d_p/40$, (c) $\delta = d_p/80$ and (d) $d_p/160$.

A schematic diagram of the system is shown in Figure 4.6(a). A constant velocity is applied at the inlet while zero velocity gradient is applied at all the other boundaries. The pressure is set to zero at the outlet and takes zero gradient for all the other boundaries. The Reynolds number Re is defined as:

$$\mathrm{Re} = \frac{d_p U}{\nu} \tag{4.25}$$

where U is the inlet velocity.

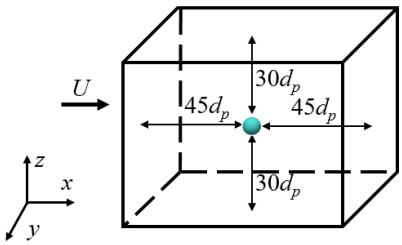

(a)

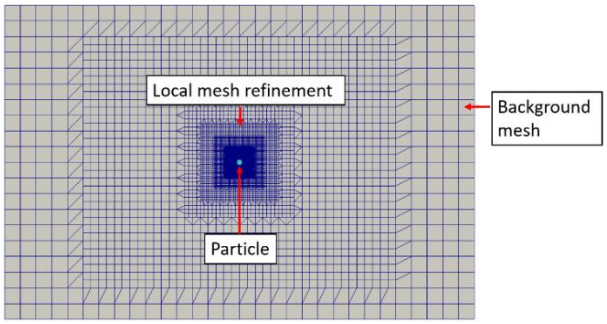

(b)

Figure 4.6. (a) Schematic diagram of the flow past a stationary single particle and (b) cross section view of the locally refined mesh.

It is confirmed in advance that the simulation domain is sufficiently large so that the results are not sensitive to the boundary effects. In order to reduce the calculation cost, local mesh refinement is applied in the simulation domain as shown in Figure 4.6(b). The finest mesh domain has edge length of $3 \times d_p$ and the centre is collocated

with that of the particle. From the finest mesh domain, the cell size gradually increases until it reaches that of the unrefined (i.e. background) mesh. The cell size of the unrefined mesh is $3 \times d_p$. Re is varied from 0.001 to 100 and the resultant drag coefficients are compared to the empirical model of Schiller & Naumann [98]. At the steady state, the drag coefficient C_D is calculated by the following expression:

$$C_D = \frac{2F_D}{\rho U^2 A} \tag{4.26}$$

where F_D is the calculated fluid force acting on the particle and A is the projected area of the particle.

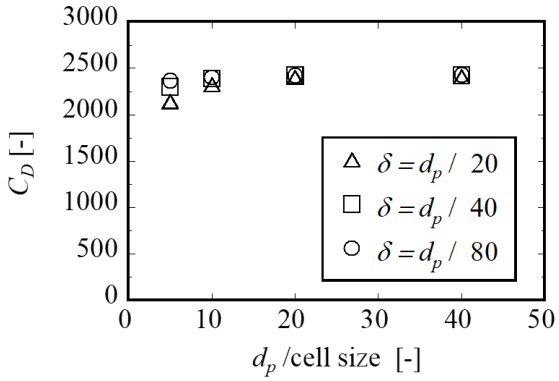

(a)

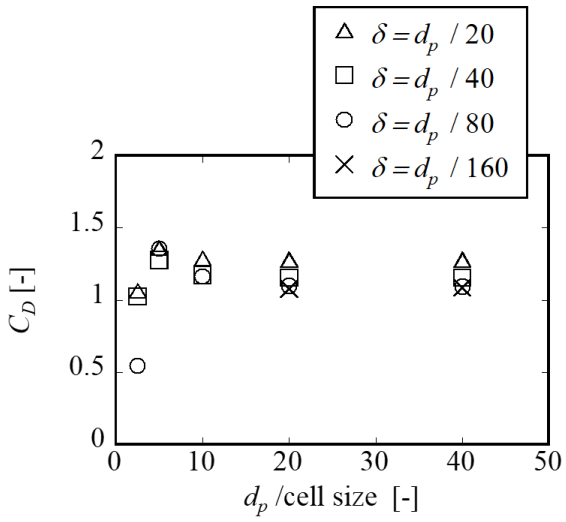

(b)

Figure 4.7. Mesh independency test; (a) Re = 0.01 and (b) Re = 100.

The mesh independency is checked for Re = 0.01 and Re = 100 cases representing the low and high Reynolds numbers tested, respectively. The resolution is defined as the ratio of the particle diameter d_p to the smallest cell size. As presented in Figure 4.7(a) and (b), the resultant drag coefficient is converged at around the resolution of 10 to 20 (depending on the thickness parameter) in all the cases. Therefore, the resolution of 20 is applied for the following results in this section to ensure the mesh independency. Note that the drag coefficient C_D is not sensitive to the thickness parameter when Re = 0.01 since the boundary layer is large when Re is small as shown in Figure 4.8(a). However, when Re = 100, the larger δ gives slightly larger C_D since there is excessive fluid flowing into the interior of the particle as shown in Figure 4.8(b)

with $\delta = d_p/20$. In general, the thickness of the boundary layer decreases when Reynolds number is increased as shown in Figure 4.8(b) with Re = 100. Therefore, employing small interface thickness (i.e. $d_p/80$) may be required to resolve the flow in the boundary layer properly.

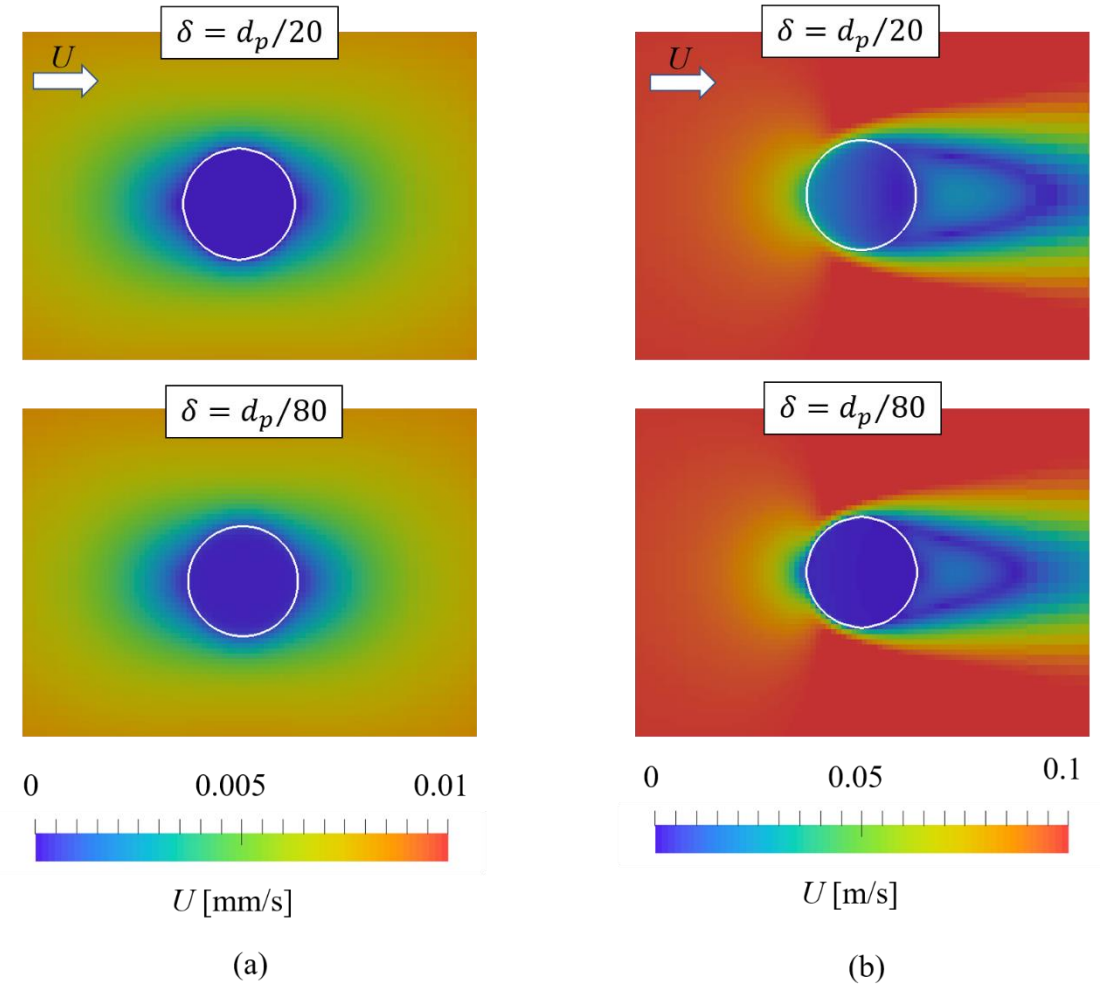

Figure 4.8. Computed fluid velocity field with thickness parameter of $d_p/20$ and $d_p/80$ at resolution of 20. (a): Re = 0.01 and (b) Re = 100.

As shown in Figure 4.9, the computed C_D values obtained from the simulation results agree well with the empirical model of Shiller & Naumann [98] as well as the simulation results reported in literature [15,22]. It is also found that the resultant drag coefficients are not very sensitive to the selection of the thickness parameter. This implies that the optimal permeability given by Eq. (4.24) is valid in this Re range. It is worth noting that employing a small thickness parameter is, on the one hand, more advantageous since the particle shape can be sharply described. This is especially important when the inter-particle (or particle-wall) distance is small as discussed in the following sections. On the other hand, the simulation time step can be larger when the thickness parameter is increased since the time step is restricted by the permeability [99]. Therefore, it is preferred to use larger thickness parameter if it does not influence the results, which is the case in Figure 4.9.

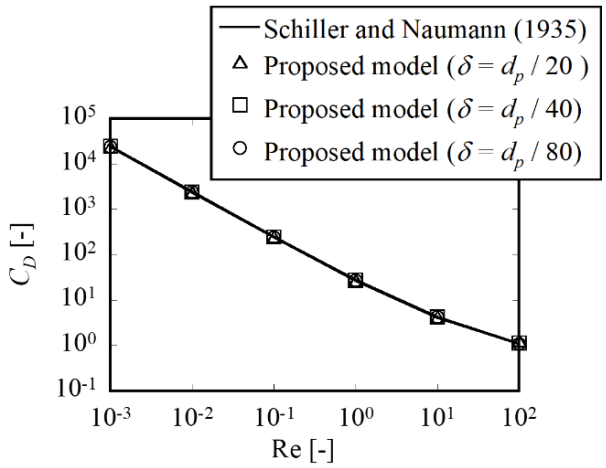

Figure 4.9. Comparison between the computed drag coefficient obtained from the simulation and the empirical model of Schiller & Naumann [98].

4.5.2 Flow through a periodic array of stationary particles

The simulation results in the preceding section prove that the resolved CFD–DEM model developed with the VP method can reasonably simulate the flow around a single particle. The resolved CFD–DEM model is applied for the flow through a periodic array of particles with the packing fraction ϕ up to 0.68 in this section. Simple Cubic (SC) and Face-Centred Cubic (FCC) arrays of stationary particles are considered in this work. Schematics of SC and FCC arrays are presented in Figure 4.10. In the SC array, five particles are aligned in a simulation domain with equal separation distance, and ϕ is varied from 0.2 to 0.5 by changing the particle size. However, the maximum packing fraction of the SC array is approximately 0.52. The FCC array is used for the higher packing fraction: 0.6 and 0.68.

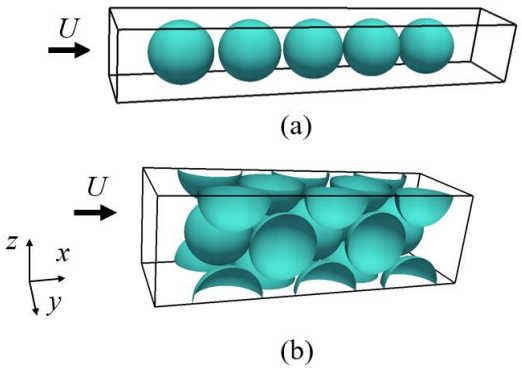

Figure 4.10. Schematics of the flow through the (a) SC and (b) FCC arrays.

Periodic boundary conditions are applied in the both y- and z-directions. A constant velocity is applied at the inlet in the x-direction whilst zero velocity gradient is set at the outlet. The pressure is set to zero at the outlet and takes zero gradient at the inlet. The Reynolds numbers calculated by Eq. (4.25) are kept to be less than 0.5 in all cases. The fluid flows through the stationary particles in a zero-gravity field. The fluid force acting on the central particle of the array is nondimensionalised by the following equation [100]:

$$K = \frac{F_D}{3\pi\mu U d_p} \tag{4.27}$$

A packed column is often modelled as a bundle of tangled tubes [101,102]. The tubes radius is replaced by an effective pore radius r_{eff}, which is determined as [103]:

$$r_{eff} = \frac{2(1-\phi)}{\phi\rho_p A_p} \tag{4.28}$$

where ρ_p is the density of the particle and $A_p = 6\ /(d_p\rho_p)$ is the specific surface area of the particle. In this case, uniform meshes are used and the resolution of the simulation is defined as the ratio of r_{eff} to the cell size.

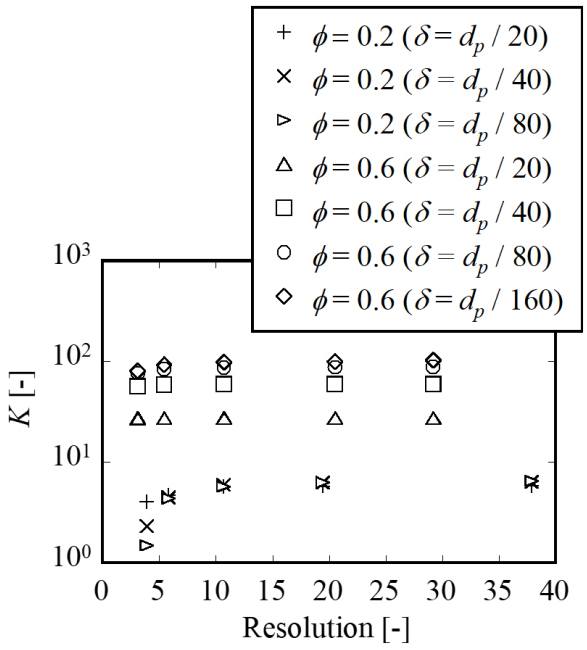

Figure 4.11. Relationship between dimensionless fluid force and the resolution. $\phi =$ 0.2 and 0.6 for SC and FCC arrays, respectively.

Figure 4.11 shows the dependency of the dimensionless fluid force on the resolution with different thickness parameters at packing fractions of 0.2 and 0.6 for the SC and FCC arrays, respectively. The results show that K is converged at the resolution of 10 in all the cases. Therefore, the resolution of 10 is ensured in the following results in this section. The fluid flow through a small gap between particles becomes important when the packing fraction increases. Hence, the solid-fluid interface thickness may have a significant impact on the resultant fluid force. The influence of the thickness parameter on the dimensionless fluid force is shown in Figure 4.12 and Figure 4.13 for the SC and FCC arrays, respectively.

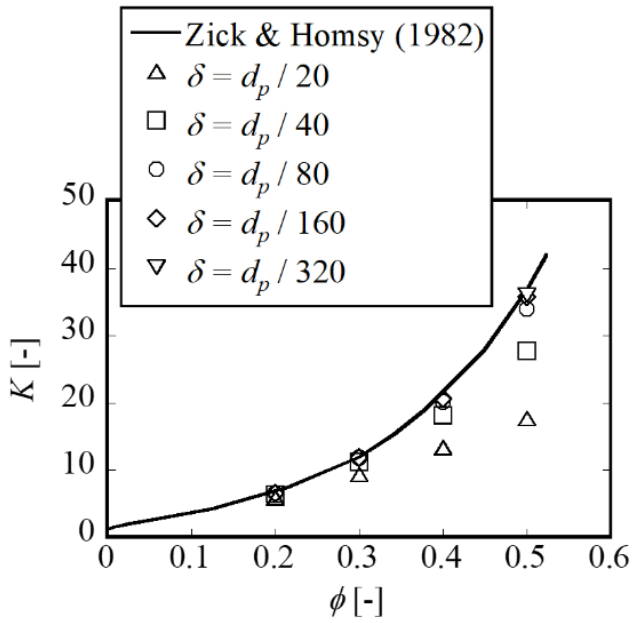

Figure 4.12. Comparison of computed dimensionless fluid force and Zick & Homsy's study for SC arrays.

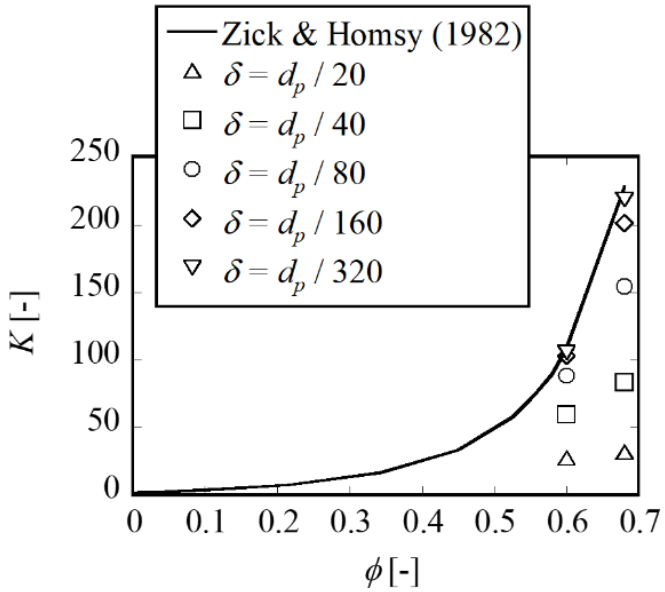

Figure 4.13. Comparison of computed dimensionless fluid force and Zick & Homsy's study for FCC arrays.

In the SC array, the difference due to the thickness parameter is marginal at the low packing fraction (e.g. $\phi = 0.2$). However, it has an impact on K when the packing fraction is larger than 0.3 and the smaller thickness parameter yields better agreement with the data of Zick and Homsy [100], which is obtained from the boundary integral method. When $d_p/20$ is applied, the large fluid velocity is found in the interior of particles as shown in Figure 4.14(a) whilst it is diminished in the case of $d_p/160$ as shown in Figure 4.14(b) since the permeability is small. The thickness parameter of $d_p/80$ provides sufficiently small particle-fluid interface region so that the fluid flow can be resolved correctly at the small gap between particles when the packing fraction is up to 0.4, as seen in Figure 4.12. However, it even requires smaller thickness parameter ($d_p/160$) in the case of packing fraction from 0.5 to 0.6 (see Figure 4.12 and Figure 4.13). When the packing fraction is 0.68, $d_p/320$ is needed since the gap between particles become tiny, as seen in Figure 4.13. When the packing fraction becomes larger, it requires a smaller thickness parameter and hence a sharper particle-fluid interface and a smaller permeability so that the fluid flow can be resolved appropriately at the narrow gap between particles. It is proven that the resolved CFD–DEM model developed with the controllable particle-fluid interface can simulate the flow through the packed particles from dilute to dense cases when the proper thickness parameter is appointed. However, no relative movement between particles are considered in this section. When particles are moving, the lubrication effect should have an impact, which is discussed in the following section.

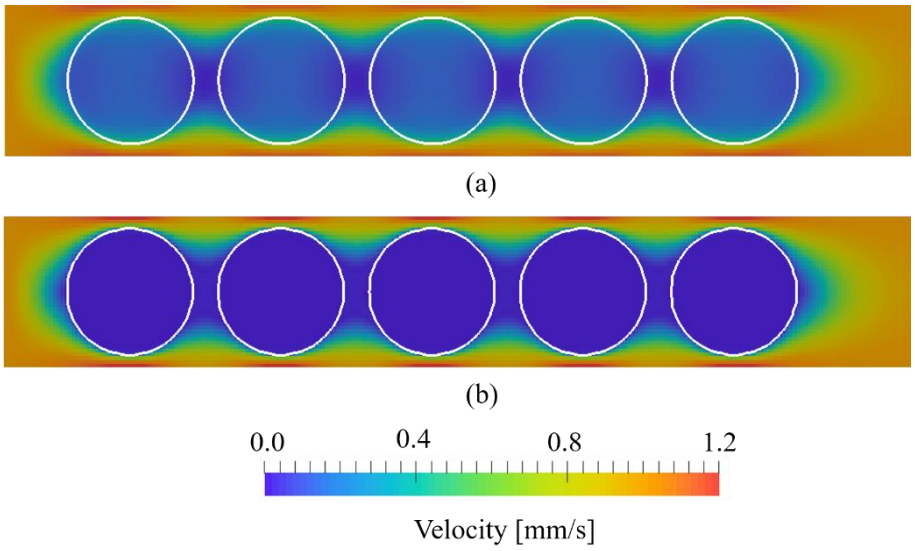

Figure 4.14. Instantaneous velocity field (SCC array, $\phi = 0.3$, resolution of 20 and Re = 0.053); (a) $d_p/20$ and (b) $d_p/160$. The white line presents the particle-fluid interface at $\chi = 0.5$.

4.5.3 A particle approaching to a plane wall

In Section 4.5.1 and 4.5.2, fixed particles are used to show the validity of the resolved CFD–DEM model developed with the controllable particle-fluid interface thickness. This section takes one step forward and examine a case with a moving particle: a particle approaching to a plane wall. Simulating this seemingly simple system is actually very challenging due to the well-known lubrication effect caused by the drainage of the interstitial fluid in the small gap between the particle and wall. It has been said that the numerical cells should be smaller than 0.1% of the particle size to properly capture the lubrication effect, which is practically impossible to run

simulation within a reasonable time scale with the current computer power. Therefore, most of the simulations in literature are performed using meshes whose cell size is around 1~10% of the particle size. This section mainly focuses on the error related to the lack of resolution with such coarse meshes.

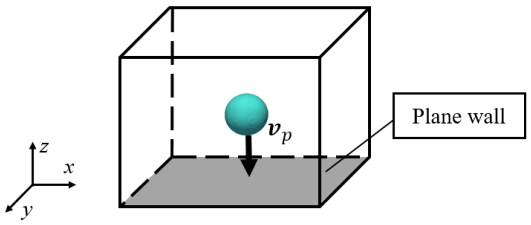

Figure 4.15. Schematic diagram of a particle approaching to a plane wall.

Figure 4.15 illustrates a cubic simulation domain whose edge length is $4.8 \times d_p$. The VP method is used for the particle whilst the no-slip condition is applied at the bottom wall. Zero velocity gradient is used at all the other boundaries. The pressure is set to zero at the top wall and takes zero gradient for all the other boundaries. The initial position of the particle is one d_p away from the bottom wall. The particle moves downwards in the negative z-direction at a constant velocity v_p. The Reynolds number used is $\mathrm{Re} = \frac{d_p v_p}{\nu} = 0.1$. Gravity is not considered in the simulation. The resolution tested (ratio of the particle to the cell size) is 20 and 40, and the thickness parameter is varied as $d_p/20$, $d_p/40$ and $d_p/80$. The fluid force acting on the particle is normalised using the Stokes drag as:

$$F^* = \frac{F_D}{3\pi\mu v_p d_p} \tag{4.29}$$

The resultant dimensionless fluid force is compared to the exact solution proposed by Brenner [104] written in the dimensionless form as follows:

$$F^* = \frac{4}{3}\sinh\alpha \sum_{n=1}^{\infty} \frac{n(n+1)}{(2n-1)(2n+3)} f(n) \tag{4.30}$$

$$f(n) = \frac{4\cosh^2\left(n+\frac{1}{2}\right)\alpha + (2n+1)^2\sinh^2\alpha}{2\sinh(2n+1)\alpha - (2n+1)\sinh 2\alpha} - 1 \tag{4.31}$$

where $\alpha = \cosh^{-1}(h/d_p)$ and h is the distance from particle centre to the plane wall.

Figure 4.16 shows the dimensionless fluid force acting on the particle as a function of the gap normalised with the particle diameter. In all the cases, the simulation results show a good agreement with the exact solution when the gap between the particle and wall is sufficiently large. However, F^* starts to deviate from the exact solution as the gap gets smaller. The deviation occurs sooner in the case of larger thickness parameter since the interface thickness becomes comparable to the gap. On the other hand, comparing the results between the resolutions of 20 and 40 with the same thickness parameter, the computed fluid forces are almost the same. This means that smaller thickness parameter is required to properly resolve the flow in the small gap although it requires longer simulation time as discussed in Section 4.5.1.

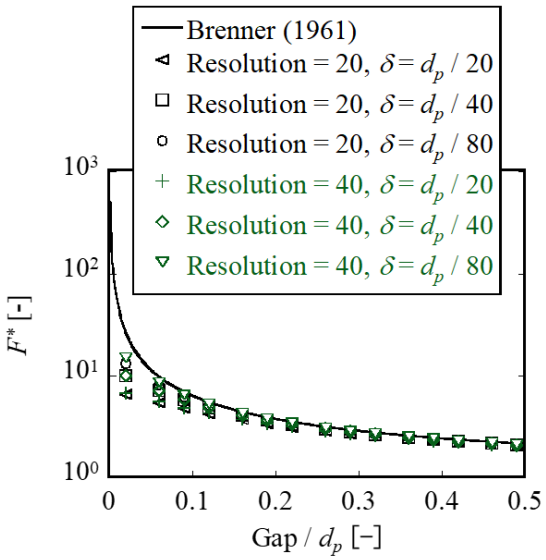

Figure 4.16. The dimensionless fluid force acting on the particle with difference thickness parameters and resolutions when the particle approaches to the bottom wall with a constant velocity.

According to Figure 4.16, it can be said that the thickness parameter is the dominant factor to cause the error. Figure 4.17 shows the error of the computed fluid force from the exact solution as a function of the gap normalised by the thickness parameter. It can be clearly seen that all the results are unified and fall into one curve. This means that the error can be universally characterised only by the ratio between the gap and thickness parameter regardless the resolution. The error increases rapidly when the particle gets closer to the plane wall: it becomes 5% roughly when the gap to thickness parameter ratio is 10 and becomes 10% roughly when the ratio is 5.

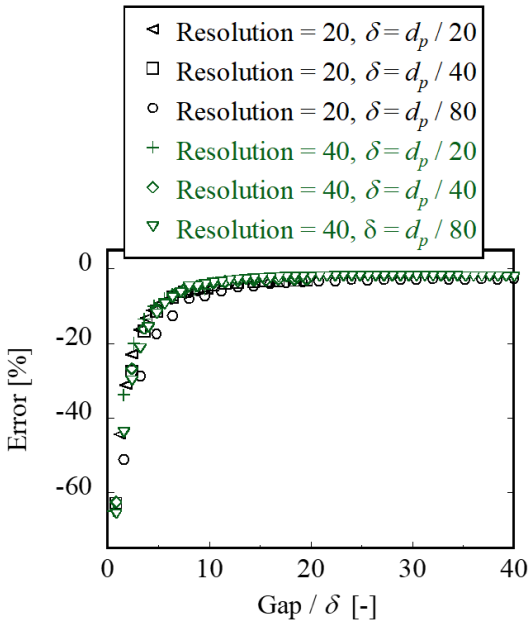

Figure 4.17. The error of the computed fluid force acting on the particle when it approaches to very near the plane wall at resolution of 20 and 40.

One way to further improve the accuracy of the simulation is to introduce the lubrication force model [47,105–109], i.e. the supplemental force model based on the solution of the lubrication equation. Typically, these lubrication models are resolution-dependent, that is, the gap to cell size ratio is used as a parameter. However, the results in this section reveals that it is important to use the gap to thickness parameter ratio instead if the interface has a thickness. The development and implementation of the lubrication force model is left in the future work and no further discussion is made in this work.

4.6 Model applications

4.6.1 Relative viscosity of suspensions

The rheology of fluid is characterized by the viscosity which is defined as the ratio between shear stress and shear rate. When particles are suspended in fluid, the viscosity of the suspension is often replaced by the effective viscosity. The relative viscosity, μ_r, is defined as the ratio of the effective viscosity to the viscosity of the suspending media. Since suspensions are of paramount importance in many processes [110], the rheological behaviours of suspensions have been intensively studied [111]. The linear dependency of the relative viscosity to packing fraction in very dilute systems is widely known as the Einstein equation [112]. For higher concentration cases, the relative viscosity of suspensions grows non-linearly with packing fraction [110,113–116]. In this section, the resolved CFD–DEM model developed is applied for the prediction of the relative viscosity of suspensions in a simple shear flow.

A schematic of suspension in a simple shear flow is shown in Figure 4.18. The no-slip boundaries are applied at the top and bottom walls which move with a constant velocity in the opposite directions to each other. The Reynolds number is $\mathrm{Re} = \frac{2UH}{\nu} = 7$ where H is the distance between the top and bottom walls. The depth in the y-direction is 5 mm and the height in the z-direction is $H = 7$ mm. The wall velocity is $U = 0.005$ m/s. Periodic boundary conditions are applied in the x- and y-directions. The particles are randomly generated in the entire simulation domain at the beginning of each simulation. Gravity, inter-particle cohesion and electrostatic forces as well as

the Brownian motion are not considered in the simulation. The fluid and solid properties are presented in Table 4.1.

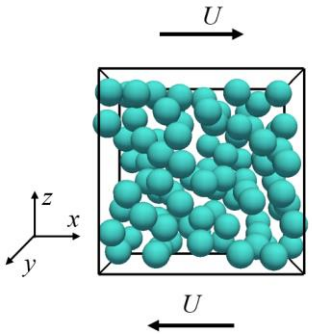

Figure 4.18. Schematic of suspension in a simple shear flow.

Table 4.1. Calculation conditions for the prediction of relative viscosity of suspension.

Property	Value
Simulation domain [mm3]	$7 \times 5 \times 7$
Thickness parameter [mm]	$d_p/80$
Particle diameter [mm]	1
Particle density [kg/m3]	2500
Young's modulus [MPa]	5
Poisson's ration [-]	0.25
Restitution coefficient [-]	0.9
Friction coefficient [-]	0.3
Fluid dynamic viscosity [Pa · s]	0.01
Fluid density [kg/m3]	1000

The packing fraction ϕ is varied from 0.0125 to 0.42 by changing the number of particles while the resolution (ratio of the effective radius, Eq. (4.28), to the cell size)

is kept more than 20 so that the simulations are mesh-independent based on Figure 4.11. The thickness parameter is $d_p/80$ which is determined based on Figure 4.12 with the packing fraction of roughly 0.4. The simulation results are compared to the experiment performed by Yoshida et al. [116] as well as the Einstein equation and the empirical equation of Mori & Ototake [117] defined by Eqs. (4.32) and (4.33), respectively.

$$\mu_r = 1 + \frac{5}{2}\phi \tag{4.32}$$

$$\mu_r = 1 + \frac{3\phi}{1 - \frac{\phi}{0.52}} \tag{4.33}$$

The results are shown in Figure 4.19. When the packing fraction is less than 0.05, the simulation results are well-matched with the Einstein equation. However, the computed μ_r starts to deviate from the Einstein equation at higher packing fraction since the hydrodynamic interactions between the particles become more prominent. Good agreement can be seen between the simulation results and the experiment results as well as the Mori & Ototake equation with ϕ up to around $= 0.3$. However, the simulation slightly underestimates the relative viscosity at $\phi = 0.42$. The potential reasons are the lubrication effect as well as the effect of the top and bottom walls. It can be concluded that the resolved CFD–DEM model developed in this study can capture the complex hydrodynamic interactions between particles in suspensions up to relatively high packing fraction.

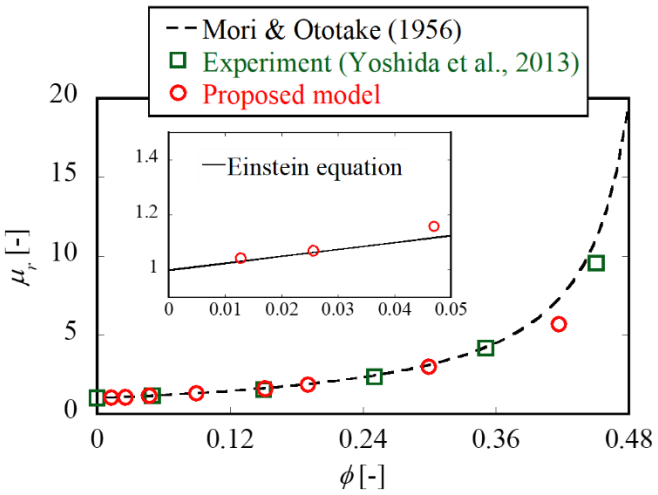

Figure 4.19. Relative viscosity plotted with the packing fraction.

4.6.2 Simulation of fluidised bed

This section shows an application of the resolved CFD–DEM model developed to the analyses of a liquid-solid fluidised bed. The schematic of the system is shown in Figure 4.20. A superficial velocity U is applied at the bottom of the bed. The particles are randomly generated in the whole simulation domain with the initial packing fraction of 0.168. The periodic boundary conditions are applied in the *x*- and *y*-directions. The resolution corresponding to effective radius is selected at 15 so that the simulations are mesh-independent as based on Figure 4.11. The thickness parameter is selected at $d_p/60$ which is based on Figure 4.12 with the packing fraction up to roughly 0.3.

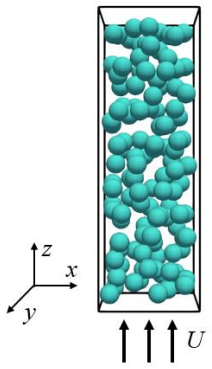

Figure 4.20. Schematic of fluidised bed.

Since the mixtures of particles with different density are commonly found in the application of fluidised bed [118], two cases are examined: uniform density (2500 kg/m^3) and binary mixture (2000 and 3000 kg/m^3) beds. Note that two beds have the same particle size. The volume ratio of the light to heavy particles for the binary mixture is 1 and they are uniformly mixed in the initial state. The average bed weight is the same between these two cases. The calculation conditions are shown in Table 4.2. When fluid flows through the particle bed, the pressure drop Δp is commonly determined by the Ergun equation [119] in the following form:

$$\frac{\Delta p}{L} = \frac{\phi}{d_p(1-\phi)^3}\left[1.75\rho_f U^2 + \frac{150\phi\mu U}{d_p}\right] \tag{4.34}$$

where L is length of the particle bed and U is the superficial velocity. When this is equivalent to the particles weight and buoyancy, Eq. (4.34) can be rewritten as:

$$\frac{\phi}{d_p(1-\phi)^3}\left[1.75\rho_f U^2+\frac{150\phi\mu U}{d_p}\right]=\phi(\rho_p-\rho_f)g \tag{4.35}$$

Eq. (4.35) is solved with respect to ϕ to estimate ϕ for the given conditions.

Table 4.2. Calculation conditions for fluidised bed.

Property	Value
Simulation domain [mm3]	$30 \times 30 \times 90$
Cell size [mm]	0.2
Thickness parameter [mm]	$d_p/60$
Particle diameter [mm]	6
Total number of particles [-]	120
Superficial velocity [m/s]	0.1
Young's modulus [MPa]	5
Poisson's ration [-]	0.25
Restitution coefficient [-]	0.9
Friction coefficient [-]	0.3
Fluid dynamic viscosity [Pa · s]	0.015
Fluid density [kg/m3]	1000

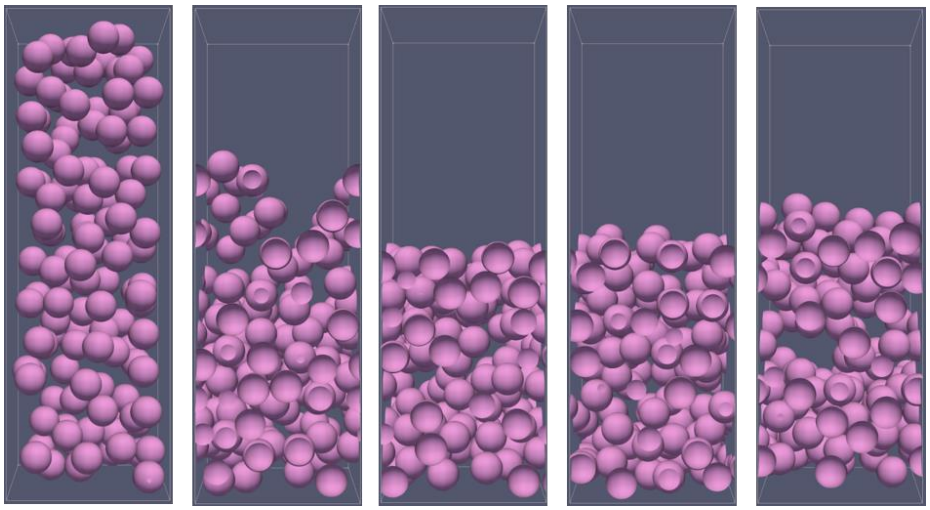

(a)

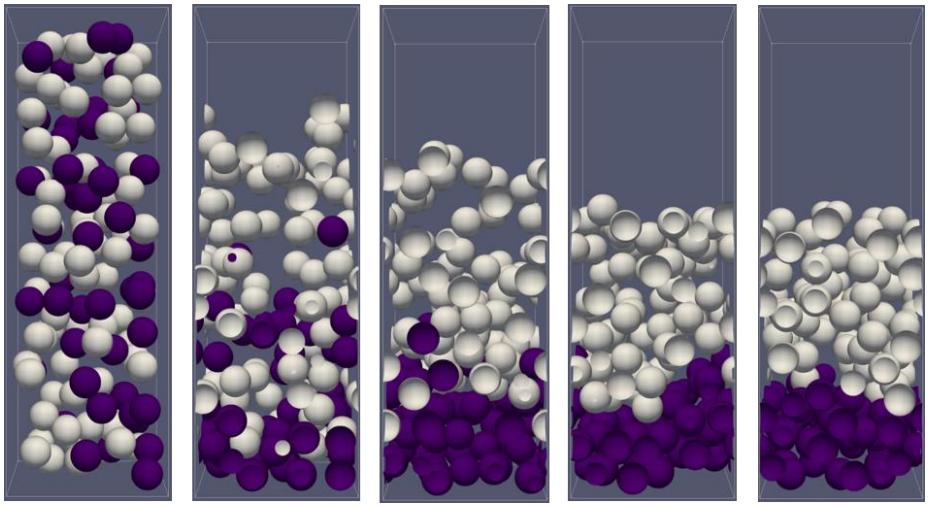

(b)

Figure 4.21. Fluidisation of particles at 0.02, 0.4, 0.6, 1.0 and 3.0 second from the left to the right; (a) uniform density and (b) binary mixture beds. The particles coloured in white, pink and purple show 2000, 2500 and 3000 kg/m^3 particles, respectively.

Snapshots of the uniform density and binary mixture beds from $t = 0.02$ s to $t = 3.0$ s are shown in Figure 4.21. At the beginning, in both cases, the particles fall downwards due to the larger gravitational force as compared to the sum of the particle-fluid interaction and buoyancy forces since the packing fraction is low within the beds. In the binary mixture bed, the denser particles tend to fall faster and accumulate at the bottom of the bed. After the fluidisation regime is reached, i.e. the regime when the average bed height and the resultant concentration remain almost constant over time, the particles with different densities are completely segregated. The bulk height of the two cases is about the same in the fluidisation regime. The estimated packing fraction by Eq. (4.35) is $\phi = 0.30$ and the average ϕ over two seconds in the fluidisation regime in the simulation is 0.315 and 0.291 for the uniform density and binary mixture beds, respectively. It can be seen in Eq. (4.35) that the denser particles at lower layer of the binary mixture bed require the higher ϕ while the lighter particles at the upper layer give smaller ϕ. However, the relationship between the drag force and the packing fraction is nonlinear. The nonlinearity of the drag force may lead to the discrepancy between ϕ obtained by the uniform density and binary mixture beds. It is worth noting that the simulation gives about 5% difference as compared to the Ergun equation.

4.7 Summary

In summary, the resolved CFD–DEM coupling model using the VP method is applied in this chapter for particle-fluid two-phase flows. A smooth mask function is used to avoid numerical oscillation and optimal permeability is employed to improve the accuracy. This chapter figures out the influence of particle-fluid interface thickness

governing the optimal permeability on the simulation accuracy. To evaluate the impact of the particle-fluid interface thickness in the simulation accuracy, three kinds of simulations are performed: (i) the flow past a single particle, (ii) the flow through a periodic array of particles and (iii) a particle approaching to a plane wall. The key findings in each tested case are as follows:

(i) In general, the resolved CFD–DEM model developed with controllable particle-fluid interface can capture the particle-fluid interaction reasonably in the Reynolds number range tested (up to $\mathrm{Re} = 100$). The drag coefficients obtained are comparable to those reported in literature. The thickness parameter is not very sensitive to the computed drag coefficient especially for low Reynolds number flows. In this sense, employing a large thickness parameter is more advantageous since the stable time step limit is determined by the permeability. However, when the highest Reynolds number is used, the error becomes relatively large with the large thickness parameters (i.e. $\delta = d_p/20$ and $d_p/40$). This is because the boundary layer becomes thinner as the Reynolds number increases. This implies that an appropriately small thickness parameter should be chosen for high Reynolds number flows.

(ii) It is proven that the effective pore radius r_{eff} is a good measure to check the mesh independency: simulation cell size needs to be at least 10 times smaller than r_{eff}. A smaller thickness parameter should be used as particle packing fraction increases since the fluid flow in the small gap between particles need to be resolved accurately. An appropriate thickness parameter for packing

fraction up to 0.68 can be readily determined from Figure 4.12 and Figure 4.13.

(iii) The simulation results indicate that the dominant factor is the thickness parameter: a smaller thickness parameter is required to capture the lubrication effect. It is also proven that the error of the fluid force to the exact solution can be universally characterised by the ratio between the gap and the thickness parameter: the error becomes about 5% when the ratio is 10 and becomes 10% roughly when the ratio is 5. These results can be used as a guideline for the further development of a lubrication force model.

In order to demonstrate the applicability of the resolved CFD–DEM model developed to the study of fluid-solid two-phase system, two applications are presented: the prediction of the relative viscosity of suspensions and the fluidised beds with uniform density and binary mixture particles. It is found that the resolved CFD–DEM model developed in this study is able to estimate the relative viscosity of the suspensions with the packing fraction up to 0.3. At higher packing fraction, however, noticeable difference from the experiment as well as the empirical model can be seen. The potential reasons are the lubrication effect as well as the effect of the top and bottom walls. The packing fractions of both the uniform density and binary mixture fluidised beds are $\phi = 0.315$ and 0.291, respectively, which are comparable to that estimated from the Ergun equation, i.e. $\phi = 0.30$. The difference between the particle volume fractions of the uniform density and binary mixture beds could be caused by the nonlinear relationship between the drag force and the packing fraction. The results in

this study indicate that the resolved CFD–DEM model developed is capable of simulating particulate flow from dilute to relatively dense system.

Chapter 5

Gas-Liquid-Solid Three-Phase Flows with Immersed Free Surface Model and Controlled Interfaces

5.1 Introduction

In this chapter, the resolved CFD–DEM model is developed using a gas-liquid interface capturing method, which is based on Volume of Fluid (VOF) method with a controllable gas-liquid interface thickness. The Immersed Free Surface (IFS) model is employed to expressed the wetting of particle surface. Based on the IFS framework, the accuracy of two capillary force models is also investigated. The VP method presented in Chapter 4 is applied for the particle-fluid interaction force.

A critical time step for the diffuse interface parameters is first derived theoretically that it has a relationship with the cell size and diffuse interface parameters as shown in Section 5.8. In order to evaluate the influence of the diffuse interface parameters controlling the gas-liquid interface thickness on the accuracy of the surface tension force calculation, Laplace pressure in a spherical droplet and the static liquid bridge between two particles are computed as shown in Sections 5.9.1 and 5.9.2.2, respectively. Two of the major methods in the literature to calculate the capillary force based on the IFS framework are compared in Section 5.9.2.2. The wetting model

developed using the IFS model is also validated by computing liquid bridge force from small to large contact angle as shown in Section 5.9.2.3. The resolved CFD–DEM model developed is also validated by performing simulation of a particle falling into liquid and dynamic liquid rupture between moving particles. The simulation results show a good agreement with the results found in the literature.

In order to demonstrate the applicability of the resolved CFD–DEM model developed in this study to the complex gas-liquid-solid three-phase system, two applications are presented, i.e. the influence of wettability on two colliding particles with the liquid bridge and analysis of hydrodynamic force acting on two colliding particles with liquid bridge, as shown in Section 5.10.

5.2 Governing equations

5.2.1 CFD governing equations

Two fluids are assumed to be isothermal, immiscible and incompressible. The continuity and momentum equations for fluid phase are shown in the following expression:

Continuity equation:

$$\nabla \cdot \boldsymbol{U} = 0 \tag{5.1}$$

Momentum equation:

$$\frac{\partial}{\partial t}(\rho \boldsymbol{U}) + \nabla \cdot (\rho \boldsymbol{U}\boldsymbol{U}) = -\nabla p + \nabla \cdot \boldsymbol{\tau} + \boldsymbol{f}_{VP} + \boldsymbol{f}_s + \rho \boldsymbol{g} \tag{5.2}$$

where $\boldsymbol{f}_s$ is the source of momentum due to surface tension. The fluid applied in this work is Newtonian and the viscous stress tensor is described in Eq. (4.3).

5.2.2 DEM governing equations

The translational and rotational motions of a particle i are governed by the Newton's second law of motion as follows:

$$m_i \dot{\boldsymbol{v}}_i = \sum_j \boldsymbol{F}_{Cij} + \boldsymbol{F}_{VPi} + \boldsymbol{F}_{CAPi} + \boldsymbol{F}_{Bi} + \boldsymbol{F}_{Gi} \tag{5.3}$$

$$I_i \dot{\boldsymbol{\omega}}_i = \sum_j \boldsymbol{T}_{Cij} + \boldsymbol{T}_{VPi} + \boldsymbol{T}_{CAPi} \tag{5.4}$$

where $\boldsymbol{F}_{CAP}$ is the capillary force (i.e. surface tension along with the three-phase contact line) and $\boldsymbol{T}_{CAP}$ is the capillary torque. The contact force is modelled by the non-linear spring-dashpot model as Section 0.

5.3 Interface capturing method

Volume of Fluid (VOF) method is one of the most frequently used for the interface capturing methods. The VOF method mainly includes interface reconstruction (for instance, Piecewise-Linear Interface Construction method) and colour function

approaches [120]. In this work, a colour function α is used to distinguish different kinds of fluid: $\alpha = 0$ and 1 indicate the gas and liquid, respectively, whereas $0 < \alpha < 1$ the gas-liquid interface. Rusche [67] proposed an advection equation for the motion of the fluid interface as the following expression:

$$\frac{\partial \alpha}{\partial t} + \nabla \cdot (\boldsymbol{U}\alpha) = -\nabla \cdot [\boldsymbol{U}_r \alpha(1-\alpha)] \tag{5.5}$$

where $\boldsymbol{U}_r$ is is the relative velocity of the liquid to the gas [121]. The first term on the right-hand side of Eq. (5.5) is for the interface compression, i.e. to suppress the excessive smearing of the interface due to the numerical diffusion [67]. However, it is reported that this interface compression term may lead to poor estimation of the surface tension force [65,66]. Recently, Washino et al. [69] proposed a combination of Eq. (5.5) and diffuse interface term, the time evolution of the colour function is governed by the following advection equation:

$$\frac{\partial \alpha}{\partial t} + \nabla \cdot (\boldsymbol{U}\boldsymbol{\alpha}) = -\nabla \cdot [\boldsymbol{U}_r \alpha(1-\alpha)] + \nabla \cdot (M \nabla \psi) \tag{5.6}$$

The second term on the right hand side of Eq. (5.6) is introduced for diffuse interface [122], that can be originally found in the phase-field (or diffuse-interface) method [123], to improve the accuracy of the surface tension force evaluation. M is the mobility and ψ is the chemical potential defined as [124]:

$$\psi = \alpha^3 - 1.5\alpha^2 + 0.5\alpha - \nabla \cdot (l^2 \nabla \alpha) \tag{5.7}$$

where l is to govern the thickness of the diffuse interface. The diffuse interface indicates that the gas-liquid interface is no longer sharp but spans over a certain thickness. Since the interface has a certain thickness and hence resolution, this study evaluates the interface thickness and resolution in order to obtain the optimal conditions for them. However, it is worth noting that the interface reconstruction method, which is less diffusive, appears as fairly accurate [125] and it also requires a special scheme for interface curvature calculation [125] or higher-order for interface reconstruction algorithm [126].

Washino et al. [69] showed that the time required to obtain fully developed interface profile, t_d, as well as the interface thickness, h, i.e. the distance between $\alpha = 0.01$ and 0.99, are correlated with the diffuse interface parameters (M and l) as:

$$t_d = 200 \frac{l^2}{M} \tag{5.8}$$

$$h = 13l \tag{5.9}$$

where t_d is the time required for the diffuse interface to be formed from the sharp interface, C is a constant presenting the number of cells smeared across the gas-liquid interface and d_{cell} is the cell size. Eq. (5.9) is used to determine l for desired h, followed by Eq. (5.8) to determine M for fully developed interface within the time scale

t_d. The fluid density and viscosity are calculated by using the weighted average of the gas and liquid properties as shown in the following equations:

$$\rho = \alpha\rho_l + (1-\alpha)\rho_g \tag{5.10}$$

$$\mu = \alpha\mu_l + (1-\alpha)\mu_g \tag{5.11}$$

where the subscripts l and g present the liquid and gas phases, respectively.

5.4 Surface tension force model

In reality, the surface tension force is exerted as a surface force on the free surface which sharply divides the gas and liquid. In the interface capturing method, however, the surface tension force is often converted into a body force and exerted on the gas-liquid interface with a finite thickness as:

$$\boldsymbol{f}_s = \sigma\kappa\nabla\alpha \tag{5.12}$$

where σ is the surface tension coefficient and κ is the interface curvature. This concept is first proposed by Brackbill et al. [63] and called Continuum Surface Force (CSF) model. The curvature κ is calculated by taking the divergence of the unit normal vector to the interface as:

$$\kappa = -\left(\nabla \cdot \frac{\nabla \alpha}{|\nabla \alpha|}\right) \tag{5.13}$$

5.5 mmersed Free Surface model

Sussman [127] introduced the Free Surface Model (FSM) for the treatment of the contact angle by extrapolating the LS function as follows:

$$\frac{\partial \varphi}{\partial \tau} + \mathbf{u}_{extend} \cdot \nabla \varphi = 0 \tag{5.14}$$

where $\mathbf{u}_{extend}$ is the extension velocity, $\mathbf{u}_{extend}$ is determined as follows:

$$\mathbf{u}_{extend} = \begin{cases} -\dfrac{\boldsymbol{n}_s - \cot(\pi - \theta)\,\boldsymbol{n}_2}{|\boldsymbol{n}_s - \cot(\pi - \theta)\,\boldsymbol{n}_2|} & if\ c < 0, \\ -\dfrac{\boldsymbol{n}_s + \cot(\pi - \theta)\,\boldsymbol{n}_2}{|\boldsymbol{n}_s + \cot(\pi - \theta)\,\boldsymbol{n}_2|} & if\ c > 0, \\ \boldsymbol{n}_s & otherwise \end{cases} \tag{5.15}$$

with

$$\boldsymbol{n}_1 = -\frac{\boldsymbol{n}_{ls} \times \boldsymbol{n}_s}{|\boldsymbol{n}_{ls} \times \boldsymbol{n}_s|} \tag{5.16}$$

$$\boldsymbol{n}_2 = -\frac{\boldsymbol{n}_1 \times \boldsymbol{n}_s}{|\boldsymbol{n}_1 \times \boldsymbol{n}_s|} \tag{5.17}$$

$$c = \boldsymbol{n}_{ls} \cdot \boldsymbol{n}_{\boldsymbol{2}} \tag{5.18}$$

$$\boldsymbol{n}_{ls} = \frac{\nabla\varphi}{|\nabla\varphi|} \tag{5.19}$$

The FSM is applied to study the droplet splashing on a dry surface based on LS framework by Yokoi [64], the fluid interface deformation with moving bodies by Sun and Sakai [72] and gas-liquid-solid flows with capillary effects by Sun and Sakai [18] based on VOF framework. $\mathbf{u}_{extend}$ in Eq. (5.14) requires three additional statements for c in order to construct the free surface.

Similar concept to the FSM method, the Immersed Free Surface (IFS) model is used to set the value of the colour function inside the true particle domain, i.e. the domain with $\chi \geq 0.5$. Here, "IFS model" proposed by Fujita et al. [71] is used as a generic term to indicate the model which artificially extends the free surface in the exterior of particles into the interior in a continuous manner as can be seen in Figure 5.1. The contact angle through the IFS solved inside the solid region is captured by solving the following IFS equation as follows:

$$\frac{\partial\varphi}{\partial\tau} + \boldsymbol{n}_s \cdot \nabla\varphi = |\nabla\varphi| \cos\theta \tag{5.20}$$

where θ is the contact angle, τ is the pseudo timestep, φ is the LS function, $\boldsymbol{n}_s$ is the unit normal vector to the particle surface and θ is the contact angle. More details and varieties of the IFS model can be found in the literature [16,64,70,71].

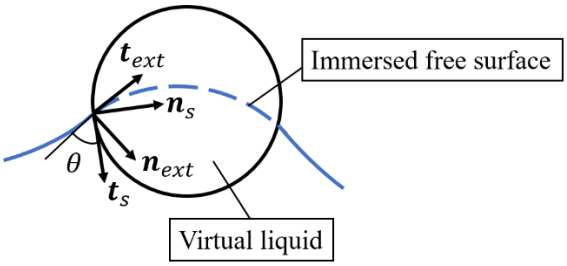

Figure 5.1. Immersed free surface formed inside the particle region. $\boldsymbol{t}_s$ and $\boldsymbol{t}_c$ are perpendicular to $\boldsymbol{n}_s$ and $\boldsymbol{n}_c$, respectively.

In the present study, the following IFS equation is employed and solved only inside the true particle domain [127]:

$$\frac{\partial \alpha}{\partial \tau} + \boldsymbol{t}_{ext} \cdot \nabla \alpha = 0 \tag{5.21}$$

$\boldsymbol{t}_{ext}$ is the direction vector to extend the colour function and it is calculated as follows:

$$\boldsymbol{t}_{ext} = \frac{\boldsymbol{n}_s - (\boldsymbol{n}_{ext} \cdot \boldsymbol{n}_s)\boldsymbol{n}_{ext}}{|\boldsymbol{n}_s - (\boldsymbol{n}_{ext} \cdot \boldsymbol{n}_s)\boldsymbol{n}_{ext}|} \tag{5.22}$$

$$\boldsymbol{n}_{ext} = \boldsymbol{n}_s \cos\theta + \boldsymbol{t}_s \sin\theta \tag{5.23}$$

$$\boldsymbol{t}_s = \frac{\nabla\alpha - (\boldsymbol{n}_s \cdot \nabla\alpha)\boldsymbol{n}_s}{|\nabla\alpha - (\boldsymbol{n}_s \cdot \nabla\alpha)\boldsymbol{n}_s|} \tag{5.24}$$

$$\boldsymbol{n}_s = \frac{\boldsymbol{r}}{|\boldsymbol{r}|} \tag{5.25}$$

where $\boldsymbol{n}_s$ is the unit vector pointing towards the centre of the particle, $\boldsymbol{t}_s$ is the unit vector that is perpendicular to $\boldsymbol{n}_s$ and pointing towards the liquid, and $\boldsymbol{n}_{ext}$ is the unit vector given by the contact angle that is perpendicular to $\boldsymbol{t}_{ext}$. Note that Eq. (5.22) essentially gives the same direction vector used in the literature [64,72], but without having to use any conditional statement.

5.6 Capillary force and torque

In the literature, there are two of the major models applied to compute the capillary force in the framework of the IFS model. The concepts and expressions of each model are briefly explained in this section.

Fujita et al. [71] proved that the line integral of the surface tension along with the three-phase contact line is equivalent to the surface integral of the surface tension force over the immersed free surface as long as the whole immersed free surface is included in the particle. Therefore, in the CSF model, the capillary force and torque can

be calculated by the volume integral of $\boldsymbol{f}_s$ over the true particle volume (i.e. the region with $\chi \geq 0.5$) as:

$$\boldsymbol{F}_{CAPi} = \int_{V_i^{\chi \geq 0.5}} \boldsymbol{f}_s \, dV \tag{5.26}$$

$$\boldsymbol{T}_{CAPi} = \int_{V_i^{\chi \geq 0.5}} \boldsymbol{r} \times \boldsymbol{f}_s \, dV \tag{5.27}$$

This model is used by Fujita et al. [16,71] and Sun and Sakai [18] and called Model A in this work. An illustration of Model A is shown in Figure 5.2(a). Although Sun and Sakai used the tensorial form of the surface tension force, the way the capillary force is calculated is fundamentally the same.

Washino et al. [23] proposed a model to convert the surface tension (as a line force) at the three-phase contact line into a body force by introducing the Dirac delta functions. This treatment is analogous to the CSF model converting the surface tension force (as a surface force) into a body force using the delta function. The capillary force and torque are then computed as:

$$\boldsymbol{F}_{CAPi} = \int_{V_i} \boldsymbol{f}_{ccf} \, dV \tag{5.28}$$

$$\boldsymbol{T}_{CAPi} = \int_{V_i} \boldsymbol{r} \times \boldsymbol{f}_{ccf}\, dV \tag{5.29}$$

$$\boldsymbol{f}_{ccf} = \sigma \boldsymbol{t}_c (\nabla\alpha \cdot \boldsymbol{t}_s)(\nabla\chi \cdot \boldsymbol{n}_s) \tag{5.30}$$

$$\boldsymbol{t}_c = -\frac{\boldsymbol{n}_s - (\boldsymbol{n}_c \cdot \boldsymbol{n}_s)\boldsymbol{n}_c}{|\boldsymbol{n}_s - (\boldsymbol{n}_c \cdot \boldsymbol{n}_s)\boldsymbol{n}_c|} \tag{5.31}$$

$$\boldsymbol{n}_c = \frac{\nabla\alpha}{|\nabla\alpha|} \tag{5.32}$$

where $\boldsymbol{t}_c$ is the unit vector in the direction of the surface tension pulling the particle surface, $\boldsymbol{n}_c$ is the unit vector perpendicular to $\boldsymbol{t}_c$, and $\boldsymbol{f}_{ccf}$ is the surface tension converted to a body force. This model is used by Washino et al. [23] and Kan et al. [17]. Although this model is known as the Continuous Capillary Force (CCF) model, it is called Model B in this work for better readability. An illustration of Model B is shown in Figure 5.2(b). The comparison between Models A and B is shown in Section 5.9.2.2.

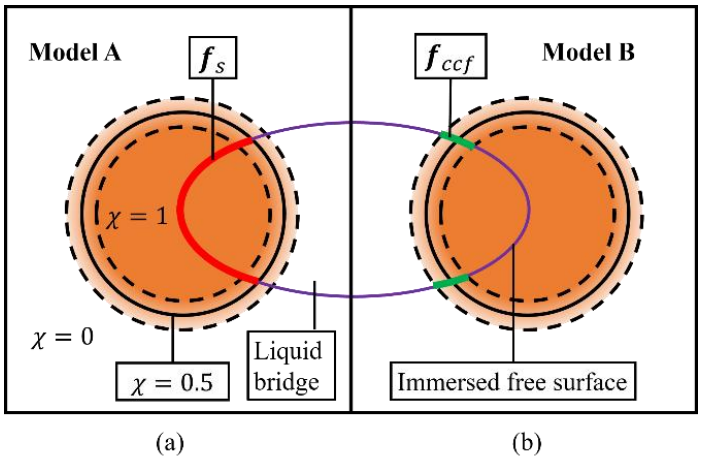

Figure 5.2. Illustrations of capillary force models: (a) Model A and (b) Model B.

5.7 Numerical solution

5.7.1 MULES

In order to ensure the boundedness of hyperbolic problems of colour function, Boris and Book [128] originally proposed the Flux Corrected Transport (FCT) technique. The FCT technique is then improved by Zalesak [129] for the simplicity in implementation. OpenFOAM applies the FCT theory extended from Zalesak's study and called "MULES" (Multidimensional Universal Limiter for Explicit Solution) to yield the boundedness of VOF function. MULES applied in this work is explained in this section. Considering an arbitrary scalar field γ, its transport equation is written as follows:

$$\frac{\partial \gamma}{\partial t} + \nabla \cdot (\boldsymbol{U}\gamma) = \nabla \cdot \boldsymbol{\Omega} \tag{5.33}$$

where $\boldsymbol{\Omega}$ is an arbitrary vector field. The solution of Eq. (5.33) is given by the FVM, the discretisation in an explicit temporal is described as follows:

$$\gamma_j^{n+1} = \gamma_j^n + \frac{\Delta t}{V_j}\left(\sum_f F_f + V_{cj} S_u\right) \tag{5.34}$$

where F_f is the face flux and it is determined as follows:

$$F_f = (\gamma^n \boldsymbol{U}^n \cdot \boldsymbol{S})_f - (\boldsymbol{\Omega}^n \cdot \boldsymbol{S})_f \tag{5.35}$$

and S_u is described as follows:

$$S_u = \frac{\gamma_j^n}{V_{cj}} \sum_f (\boldsymbol{U}^n \cdot \boldsymbol{S})_f \tag{5.36}$$

where the subscript j denotes the cell index, the superscript n is the index for temporal steps, the $\boldsymbol{S}$ is the area vector of the face, V_c is the cell volume, the subscript f indicates the face index of the cell j and Δt is the time step interval. The face flux F_f is then evaluated by a weighting factor λ_f as follows:

$$F_f = F_{adv}^L + \lambda_f A_f \tag{5.37}$$

$$F_{adv} = (\gamma^n \boldsymbol{U}^n \cdot \boldsymbol{S})_f \tag{5.38}$$

$$A_f = F_{adv}^H - F_{adv}^L - (\boldsymbol{\Omega}^n \cdot \boldsymbol{S})_f \tag{5.39}$$

where F_{adv} is the advective face flux, the superscript L and H indicates a lower order scheme and a higher other but unbounded scheme, respectively, and A_f is the anti-diffusive flux. The weighting factor λ_f is defined in the range of $0 \leq \lambda_f \leq 1$. In the cases of $\lambda_f = 0$ or 1, the time integrations have lower or higher order, respectively. The boundedness of γ is controlled by the local extremum γ_j^{min} and γ_j^{max} in the cell j and they are expressed as:

$$\gamma_j^{\max} = \min(\max(\gamma_j, \gamma_{j,N}), \gamma_j^{\max G}) \tag{5.40}$$

$$\gamma_j^{\min} = \max(\min(\gamma_j, \gamma_{j,N}), \gamma_j^{\min G}) \tag{5.41}$$

where $\gamma_{j,N}$ is all the neighbours by face of the cell j and $\gamma_j^{\max G}$ and $\gamma_j^{\min G}$ are the maximum and minimum values of γ in the cell j. The total inflows P_j^+ and outflows P_j^- for each cell are defined as:

$$P_j^+ = -\sum_f A_f^- \tag{5.42}$$

$$P_j^- = -\sum_f A_f^+ \tag{5.43}$$

where A_f^- and A_f^+ represent the inflows and outflows, respectively. The maximum fluxes flowing into the cell i (Q_j^+) and flowing out (Q_j^-) are expressed as follows:

$$Q_j^+ = \frac{V}{\Delta t}\left(\gamma_j^{\max} - \gamma_j\right) + \sum_f F_{adv}^L \tag{5.44}$$

$$Q_j^- = \frac{V}{\Delta t}\left(\gamma_j^n - \gamma_j^{\min}\right) - \sum_f F_{adv}^L \tag{5.45}$$

The weighting factor λ_f is initially set at 1 for all faces and then calculated by the iterative procedure. λ_f is later updated as follows:

$$\lambda_j^{\mp,\epsilon+1} = \max\left[\min\left(\frac{\pm\sum_f \lambda_f^\epsilon A^\pm + Q_i^\pm}{P_j^\pm}, 1\right), 0\right] \tag{5.46}$$

$$\lambda_f^{\epsilon+1} = \begin{cases} \min\left(\lambda_P^{+,\epsilon+1}, \lambda_N^{-,\nu+1}\right), & if\ A_f \geq 0 \\ \min\left(\lambda_P^{-,\epsilon+1}, \lambda_N^{+,\nu+1}\right), & if\ A_f \leq 0 \end{cases} \tag{5.47}$$

where superscript ϵ denotes the number of iterations, the subscript P and N denote the owner and neighbour cell of the given face f, respectively.

5.7.2 Solution of advection equation

In order to ensure the boundedness of the colour function, MUSLES described in Section 5.7.1 is applied to solve the advection equation Eq. (5.6) by replacing γ with α and $\boldsymbol{\Omega}$ with $-\boldsymbol{U_r}\alpha(1-\alpha)+M\nabla\psi$. In addition, $F_{\alpha dv}^{L}$ is evaluated with the upwind scheme and $F_{\alpha dv}^{H}$ with the van Leer second order TVD [130]. The other quantities are given as follows:

$$\alpha_i^{minG}=0 \tag{5.48}$$

$$\alpha_i^{maxG}=1 \tag{5.49}$$

When the interface compression is considered, the interface is compressed in the direction normal to the interface. The interface compression flux is determined as follows [65,67]:

$$(\boldsymbol{U_r}\cdot\boldsymbol{S})_f=C_\alpha\left(\boldsymbol{U}\cdot\frac{\boldsymbol{S}}{|\boldsymbol{S}|}\right)_f\left(\frac{\nabla\alpha}{|\nabla\alpha|}\cdot\boldsymbol{S}\right)_f \tag{5.50}$$

where C_α is a dimensionless coefficient to control the degree of compression and it is equal to 1 in this study.

5.7.3 Solution of IFS equation

At each physical time step, the IFS equation is solved inside the true particle domain until it reaches the steady state in the pseudo-time. Since the $\boldsymbol{t}_{ext}$ field is not divergence free in general, it is difficult to keep the boundedness of the colour function by solving Eq. (5.21). In order to ensure the boundedness, the following constraint is enforced:

$$\alpha = \min(\max(\alpha, 0), 1) \tag{5.51}$$

where the function $\min(A, B)$ and $\max(A, B)$ take the smaller and larger values between A and B, respectively. However, the resultant α field and more importantly its gradient can be unsmooth due to the artificial bounding and may cause a convergence problem. Hence, the following diffusion equation is solved to smooth out the α field:

$$\frac{\partial \alpha}{\partial \tau} = \nabla \cdot (D \nabla \alpha) \tag{5.52}$$

Although this diffusion procedure helps the convergence of the solution, the results can suffer significant interface smearing. Therefore, the following anti-diffusion equation is solved to prevent this problem:

$$\frac{\partial \alpha}{\partial \tau} = -\nabla \cdot (D \nabla \alpha) \tag{5.53}$$

Eqs. (5.21), (5.51), (5.52) and (5.53) are solved in turn at each pseudo-time step. $D = 1$ is used in general although it is slightly increased when there is a convergence problem. The pseudo-time step interval is around 10% of the cell size depending on the value of D. A flux limiter [68] is used for Eq. (5.53) to obtain a stable solution of this ill-posed equation.

5.7.4 Fluid volume correction

The governing equations for fluids and particles in Section 5.2 are not solved simultaneously but solved in turn, which is known as the segregated solution procedure. With the IFS model, this can cause a global mass conservation problem in the fluid domain (i.e. the region with $\chi < 0.5$): when there is a motion of the particle, the fictitious fluid in the particle domain can be "released" to the fluid domain. Therefore, a simple volume correction step is applied as:

$$\alpha = \alpha_{after} + \left|\nabla \alpha_{after}\right| \frac{V_e}{S_s} \tag{5.54}$$

$$V_e = V_{before} - \Delta V_{BC} - V_{after} \tag{5.55}$$

$$V_{before} = \sum_{\chi<0.5} \alpha_{before} V_{cell} \tag{5.56}$$

$$V_{after} = \sum_{\chi<0.5} \alpha_{after} V_{cell} \tag{5.57}$$

$$S_s = \sum_{\chi<0.5} |\nabla \alpha_{after}| V_{cell} \tag{5.58}$$

where α_{after} is the erroneous colour function which does not satisfy the global mass conservation, V_e is the total volume error, S_s is the total surface area of the gas-liquid interface, ΔV_{BC} is the net volume of liquid left through the boundaries, α_{before} is the colour function in the previous time step and V_{cell} is the volume of the CFD cell. This volume correction procedure is similar to what is used by Fujita et al. [16] for the signed distance function, and applied multiple times until the global mass conservation is satisfied.

5.7.5 Numerical solution procedure

The resolved CFD–DEM simulation for gas-liquid-solid three-phase flow is implemented by open source software: OpenFOAM [67] and LIGGGTHS [131] for the fluid and the particle phases, respectively, as the same to Chapter 4. A cartesian coordinate system is used in this study. The pressure and velocity fields are also obtained by the PIMPLE [96] algorithm. In LIGGGTHS, the equation of motion for the particles is solved by using the velocity Verlet algorithm. The simulation time step for CFD is required to be smaller than the following two conditions: (i) the permeability

calculated by Eq. (4.24) and (ii) the critical time step for the diffuse interface term as discussed in 5.8. The time step for DEM is determined based on the Rayleigh time [92] with a safety factor of 0.1. A solution flow chart can be found in Figure 5.3.

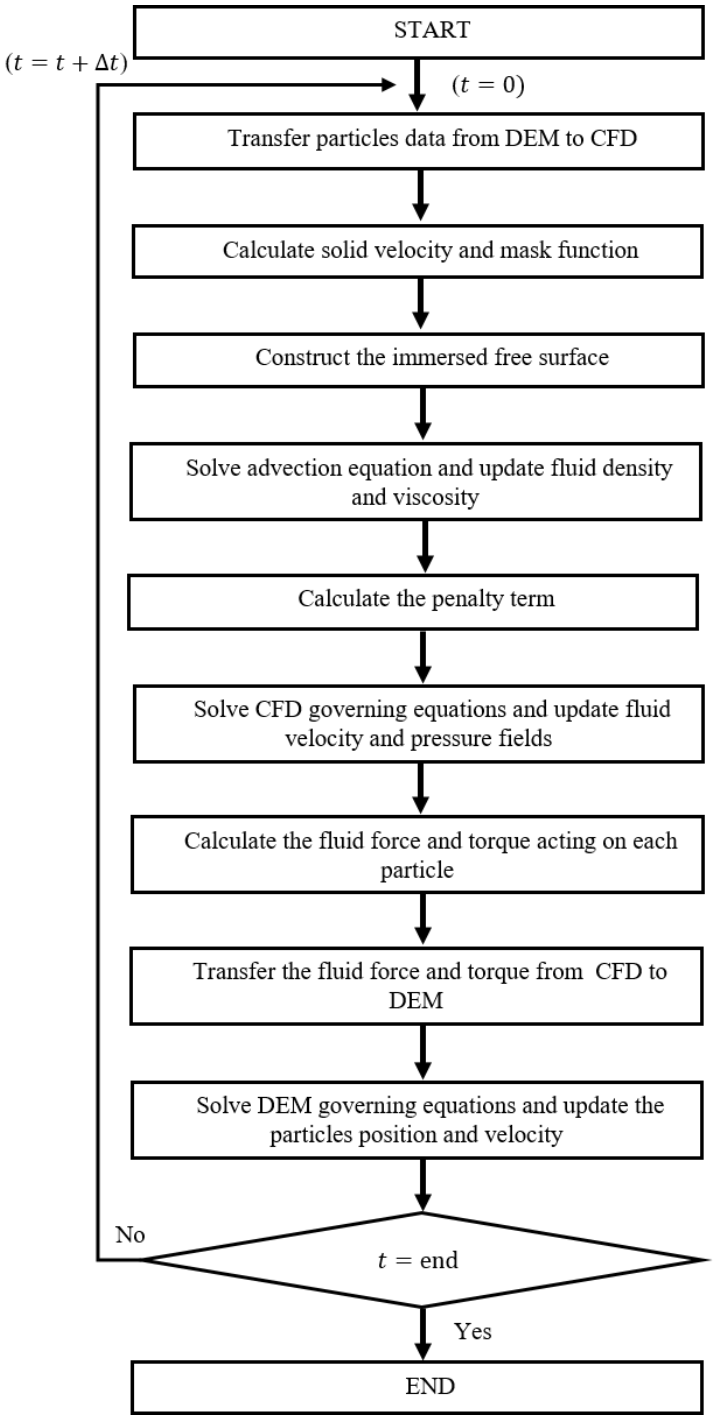

Figure 5.3. Numerical solution flow chart of the resolved CFD–DEM model for gas-liquid-solid three-phase flow.

5.8 Critical time step for diffuse interface

In Section 5.3, it is explained that the diffuse interface can be controlled by the parameters M and l. However, employing excessively large values of these parameters requires a significantly small time step or otherwise the simulation becomes unstable to gives a chequerboard pattern as shown in Figure 5.4(a).

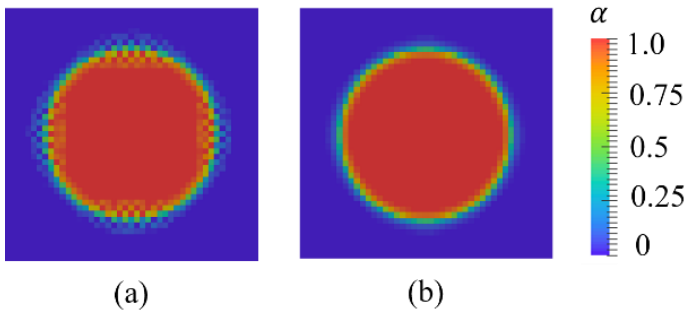

Figure 5.4. Example of colour function fields obtained from (a) unstable and (b) stable simulations.

For stable simulation as shown in Figure 5.4(b), it is important to find a critical time step Δt_c. Neglecting the advection and interface compression terms, Eq. (5.6) can be written in the following non-dimensionalised form:

$$\frac{\partial \alpha}{\partial t^*} = \nabla^* \cdot [\nabla^* \{\alpha^3 - 1.5\alpha^2 + 0.5\alpha - \nabla^* \cdot (\nabla^* \alpha)\}] \tag{5.59}$$

where $t^* = tM/l^2$ and $\nabla^* = l\nabla$. From the stability point of view, the term with the fourth-order space derivative on the right-hand side may be the most critical. Therefore, it is hypothesised that the critical value of the dimensionless time step $\Delta t_c^* = \Delta t_c M/l^2$ is correlated to the dimensionless cell size $\Delta x^* = \Delta x/l$ as:

$$\Delta t_c^* \propto \Delta x^{*4} \tag{5.60}$$

Therefore,

$$\Delta t_c \propto \frac{\Delta x^4}{Ml^2} \tag{5.61}$$

Table 5.1. Calculation conditions for critical time step of diffuse interface.

Properties	Range
Δx [mm]	0.02−0.033
M [mm2/s]	3.17 – 1893.5
l [mm]	0.00308– 0.0308

In order to check the validity of this critical time step correlation, Eq. (5.6) without the advection and interface compression terms is solved with various conditions. $\alpha = 1$ is initially set inside a spherical domain with a diameter of $d_d = 1$

mm placed at the centre of a cubic simulation domain with an edge length of $2d_d$. Zero gradient condition is applied for all the boundaries. The calculation conditions tested are listed in Table 5.1. At each condition, it starts with large Δt so that the simulation is unstable. Δt is then manually reduced until stable simulation is achieved, which is defined as the critical time step Δt_c.

The relationship between $\frac{\Delta x^4}{Ml^2}$ and the obtained Δt_c is shown in Figure 5.5. Although there is a small deviation due to the manual change of the time step, a linear relationship can be clearly seen for a wide range of $\frac{\Delta x^4}{Ml^2}$, which proves that Eq. (5.61) is valid. Although the slope obtained from the least-square method is 0.012, a safety factor is also applied so that this section proposes the following time step criteria for diffuse interface, which is used for all the simulations presented in the sections below as follows:

$$\Delta t = 0.01 \frac{\Delta x^4}{Ml^2} \tag{5.62}$$

Note that the slope 0.01 is specifically for the numerical solution procedure with MULES explained in Section 5.7.1, and may differ if different solution procedure is used. However, the relationship shown in Eq. (5.61) should hold in any case.

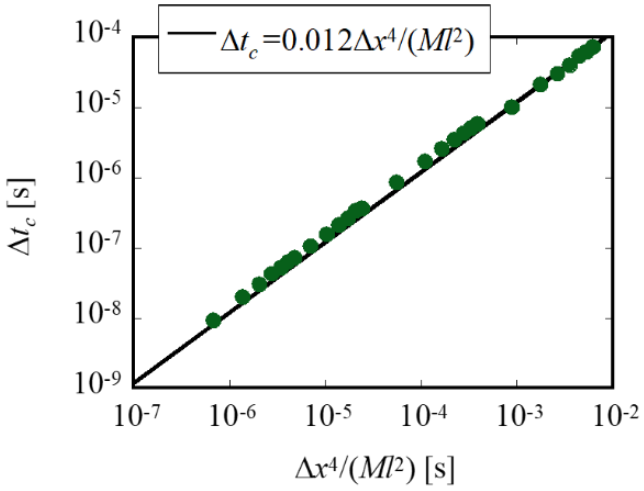

Figure 5.5. Relationship between the critical time step Δt_c and $\frac{\Delta x^4}{Ml^2}$.

5.9 Model validations

5.9.1 Laplace pressure in a spherical droplet

This section presents simulation of a spherical droplet with a diameter d_d of 1 mm as depicted in Figure 5.6 to assess the accuracy of the surface tension force for a gas-liquid two-phase system. The droplet is placed at the centre of a cubic simulation domain with an edge length of $2d_d$. The simulation conditions are listed in. Zero gradient boundary condition is applied for all the boundaries and the gravity is not considered.

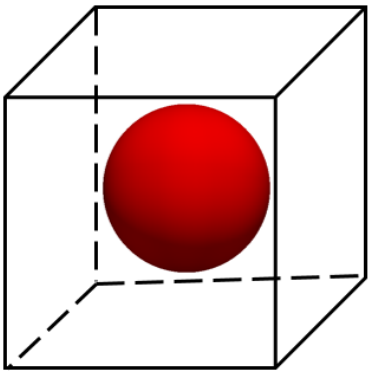

Figure 5.6. Illustration for the spherical droplet in the cube simulation domain.

Table 5.2. Gas and liquid properties for the calculation of Laplace pressure in the spherical droplet.

Properties	Value
Liquid density ρ_l [kg/m3]	1000
Liquid viscosity μ_l [Pa·s]	0.001
Gas density ρ_g [kg/m3]	1.2
Gas viscosity μ_g [Pa·s]	1.8×10^{-5}
Surface tension coefficient σ [N/m]	0.072
t_d [s]	1×10^{-4}

The computed Laplace pressure (i.e. the pressure difference between the interior and exterior of the droplet induced by the surface tension force) obtained from the simulation is compared to the theoretical value to evaluate the error as:

$$\text{Error} = \frac{P_L^{simulation} - P_L^{theory}}{P_L^{theory}} \times 100 \tag{5.63}$$

where $P_L^{simulation}$ is the Laplace pressure obtained from the simulation and P_L^{theory} is the theoretical value given by:

$$P_L^{theory} = \frac{4\sigma}{d_d} \tag{5.64}$$

The following parameters are defined here:

$$l_d^* = \frac{l}{d_d} \tag{5.65}$$

$$l_{\Delta x}^* = \frac{l}{\Delta x} \tag{5.66}$$

where l_d^* is associated with the relative size of the interface thickness to the droplet diameter, and $l_{\Delta x}^*$ is that to the cell size. As mentioned in Section 5.3, if the interface thickness is defined as the distance between $\alpha = 0.01$ and 0.09, $13l_d^*$ indicates the relative size of the interface to the droplet diameter and $13l_{\Delta x}^*$ can be interpreted as the gas-liquid interface resolution (number of cells per interface thickness). However, since the definition of the interface thickness is obviously arbitrary, l_d^* and $l_{\Delta x}^*$ are used in the discussion below. Figure 5.7 shows an example of the gas-liquid interface for $l_d^* =$

0.0077 with different $l^*_{\Delta x}$ values: (a) $l^*_{\Delta x} = 0.15$, (b) $l^*_{\Delta x} = 0.31$, (c) $l^*_{\Delta x} = 0.62$ and (d) $l^*_{\Delta x} = 0.92$.

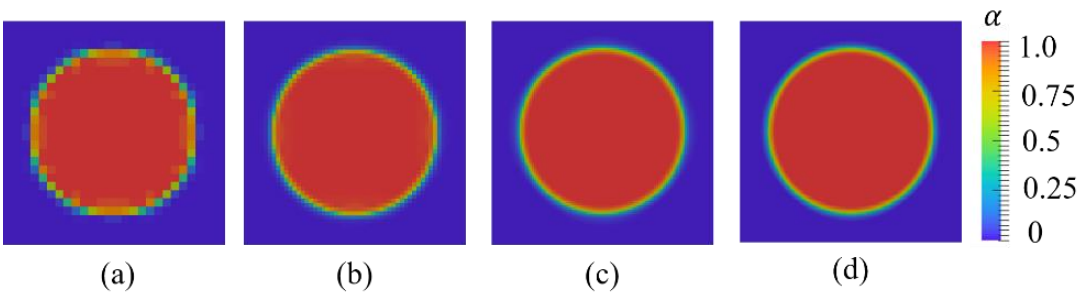

Figure 5.7. Gas-liquid interface of spherical droplet for $l^*_d = 0.0077$ with different interface resolution: (a) $l^*_{\Delta x} = 0.15$, (b) $l^*_{\Delta x} = 0.31$, (c) $l^*_{\Delta x} = 0.62$ and (d) $l^*_{\Delta x} = 0.92$.

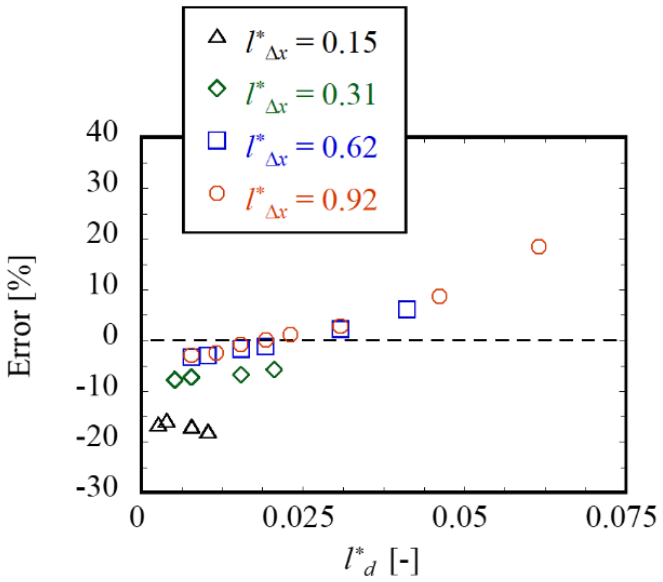

(a)

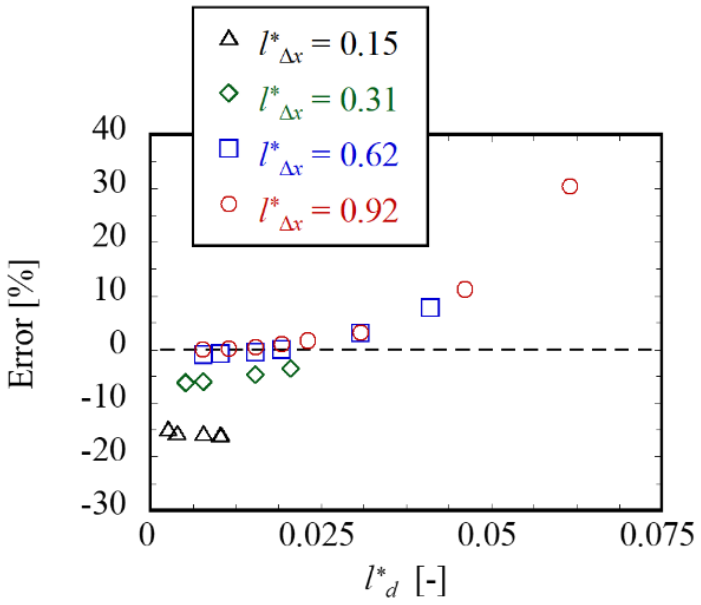

(b)

Figure 5.8. The error of the Laplace pressure for spherical droplet with different gas-liquid interface thickness and resolution; (a) with and (b) without the interface compression term in Eq. (5.6).

Figure 5.8(a) and (b) show the error of the computed Laplace pressure with different l_d^* and $l_{\Delta x}^*$ with and without considering the interface compression term in Eq. (5.6), respectively. In general, both of the graphs show a similar tendency. It is found that the results with $l_{\Delta x}^* = 0.62$ and 0.92 almost give the identical error for a given l_d^* whilst those with $l_{\Delta x}^* = 0.15$ and 0.31 show larger error. This indicates that $l_{\Delta x}^* = 0.62$ is the required gas-liquid interface resolution to achieve the mesh-independent results. In addition, in the cases of $l_{\Delta x}^* = 0.62$ and 0.92, the error decreases as l_d^* decreases and

converges around $l_d^* = 0.013$. This infers that there is a model error caused by introducing the artificial gas-liquid interface thickness, and the maximum thickness to be used for the spherical droplet is roughly given by $l_d^* = 0.013$. Comparing Figure 5.8 (a) and (b), the overall error increases slightly (by a few percent) by using the interface compression term. This is in line with the results in the literature [65,66] and caused by the spurious current induced by the extra sharpening of the gas-liquid interface.

It is in general recommended not to employ the interface compression unless it is necessary, especially to simulate a static case. However, in more dynamic cases with large interface deformation, the numerical diffusion may become a major issue and the interface compression can offer an option to improve the simulation in exchange with a slight increase of the error of the surface tension force by a few percent. The effectiveness of the interface compression in a dynamic case is shown in Section 5.9.3.

5.9.2 Liquid bridge force between two stationary particles

In this section, simulation of a liquid bridge formed between two stationary particles of equal size as shown in Figure 5.9 is presented to assess the accuracy of the surface tension force (Section 5.9.2.1), capillary force (Section 5.9.2.2) and contact angle (Section 5.9.2.3) for a gas-liquid-solid three-phase system. The particle diameter d_p is 1 mm, the ratio between the liquid volume and the single particle volume is 0.3 and the separation distance s is a quarter of the particle diameter d_p. The contact angle is 60° in Sections 5.9.2.1 and 5.9.2.2 whilst it is varied in Section 5.9.2.3. The common

calculation conditions are listed in Table 5.3. Since only a static liquid bridge is considered, the interface compression term in Eq. c is not used as suggested in Section 5.9.2. The simulation domain is $1.5d_p \times 2.7d_p \times 1.5d_p$. Zero gradient boundary condition is applied for all the boundaries and the gravity is not considered.

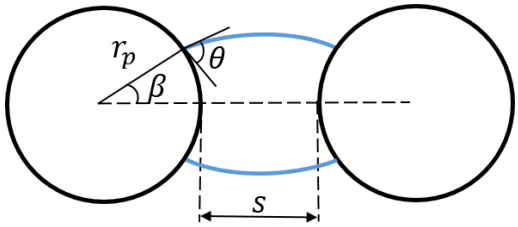

Figure 5.9. Schematic of liquid bridge between two particles.

Table 5.3. Calculation conditions for liquid bridge between two stationary particles.

Properties	Value
Particle diameter d_p [mm]	1
Liquid density ρ_l [kg/m3]	1000
Liquid viscosity μ_l [Pa·s]	0.01
Gas density ρ_g [kg/m3]	1.2
Gas viscosity μ_g [Pa·s]	1.8×10^{-5}
Surface tension coefficient σ [N/m]	0.072
Liquid to single particle volume ratio [-]	0.3
t_d [s]	1×10^{-4}

The liquid bridge force exerted on the particle on the right is calculated from the simulation as:

$$F_{LB} = F_{CAP} + F_{LAP} \tag{5.67}$$

where F_{LB} is the axial component of the liquid bridge force, F_{CAP} is that of the force due to the surface tension along with the three-phase contact line (i.e. capillary force) and F_{LAP} due to the Laplace pressure. As used by other researchers [18,132–136], employ the Surface Evolver (SE) solver [137] is employed to obtain the reference value of the liquid bridge force. The SE solver expresses the gas-liquid interface with a mesh to find the shape to minimize the free surface energy based on the gradient descent algorithm. The SE solver provides the geometrical shape of the liquid bridge so that F_{CAP} and F_{LAP} can be calculated based on the following equations [138]:

$$F_{CAP} = -2\pi r_p \sigma \sin\beta \sin(\theta + \beta) \tag{5.68}$$

$$F_{LAP} = \pi r_p^2 P_L \sin^2\beta \tag{5.69}$$

where β is the half-filling angle (see Figure 5.9) and P_L is the Laplace pressure. It is confirmed that the mesh used for the SE solver is fine enough and the results are mesh independent in all the results presented in this section.

The gas-liquid interface is extended into the particles using the IFS model as shown in Figure 5.10. The liquid bridge force obtained from the simulation $F_K^{simulation}$ is compared to that from the SE solver F_K^{SE}. The difference is defined as:

$$\text{Difference} = \frac{F_K^{simulation} - F_K^{SE}}{F_K^{SE}} \times 100 \tag{5.70}$$

where the subscript K takes CAP, LAP or LB.

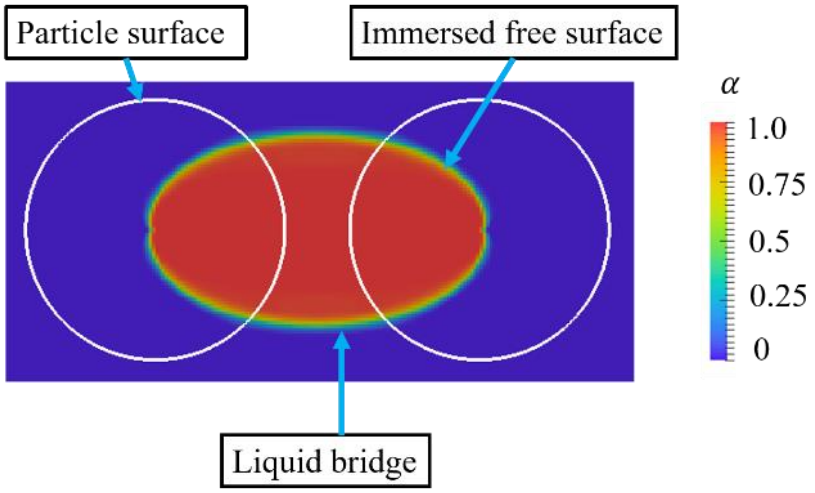

Figure 5.10. Example of liquid bridge between two particles with immersed free surface.

In the simulation, F_{LAP} is computed by Eq. (4.6) since the penalty term should be in balance with only the pressure gradient term if all the terms related to the velocity and external force are zero in the fluid momentum equation. F_{CAP} is calculated by Eqs.

(5.26) and (5.28), i.e. Model A and B, so that the results can be compared. The following parameters are defined here:

$$\delta^* = \frac{\delta}{d_p} \tag{5.71}$$

$$l_p^* = \frac{l}{d_p} \tag{5.72}$$

where δ^* is associated with the relative size of the fluid-solid interface thickness to the particle diameter and is used to assess the error related to the VP method. l_p^* is associated with the relative size of the gas-liquid interface thickness to the particle diameter that is related to the accuracy of the calculation of the surface tension and capillary forces.

5.9.2.1 Force due to Laplace pressure

The difference of F_{LAP} from the results of the SE solver as a function of δ^* with different $l_{\Delta x}^*$ is shown in Figure 5.11. l_p^* is kept constant to 0.0077. For a given δ^*, $l_{\Delta x}^* = 0.62$ and 0.92 give similar results whereas employing smaller $l_{\Delta x}^*$ than 0.62 results in a larger difference, which is in line with the results in Section 5.9.1. When large δ^* is used (e.g. 0.013), the permeability calculated by Eq. (4.24) becomes large and the spurious current can migrate into the particle domain as shown in Figure 5.12(a). Therefore, not only the pressure gradient term but also the inertial and viscous terms remain in the fluid momentum equation, and F_{LAP} calculated from Eq. (4.6) becomes

less accurate. As δ^* decreases, the difference from the SE solver results decreases: it becomes less than 5% around $\delta^* = 0.0063$ and roughly converges at $\delta^* = 0.0031$ where the spurious current hardly exists inside the particle domain in Figure 5.12(b).

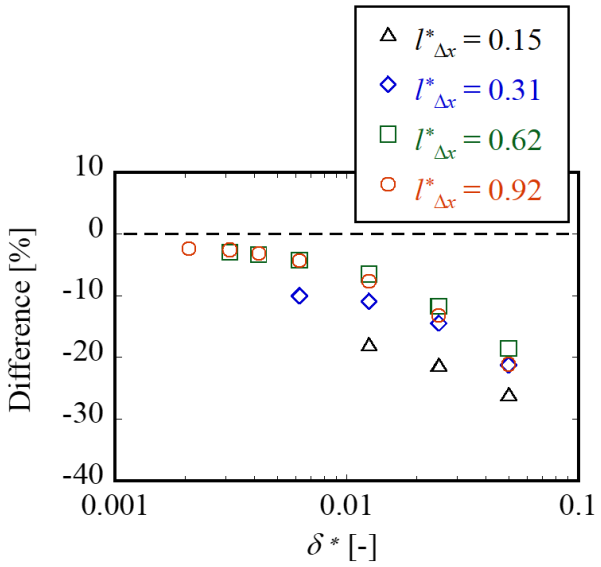

Figure 5.11. Difference of F_{LAP} from the results of the SE solver as a function of δ^*.

Figure 5.13 shows the difference of F_{LAP} from the results of the SE solver as a function of l_p^* with $\delta^* \leq 0.0063$ as based on Figure 5.11. Similar to Figure 5.11, $l_{\Delta x}^* = 0.62$ is the sufficient gas-liquid interface resolution and the smaller l_p^* yields lesser difference. It can be found that the difference converges at around $l_p^* = 0.012$. This suggests the maximum gas-liquid interface thickness to be about the same as the gas-liquid two-phase case in Figure 5.8.

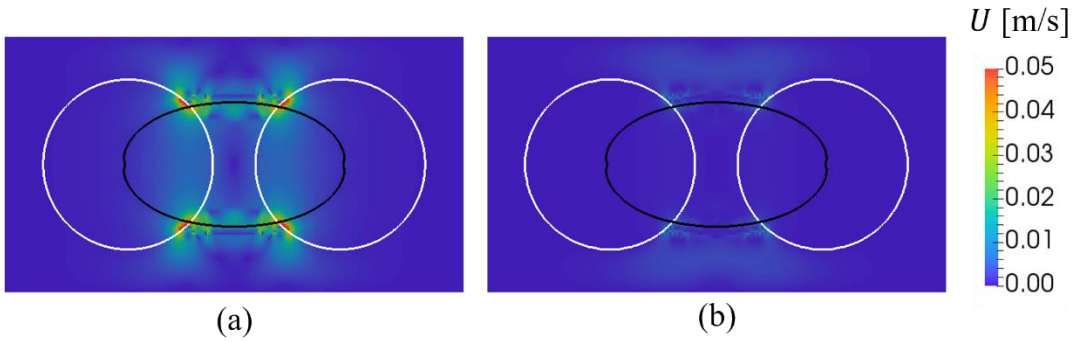

Figure 5.12. Computed velocity field with $l^*_{\Delta x} = 0.62$; (a) $\delta^* = 0.013$ and (b) $\delta^* = 0.0031$. The white and black lines show $\chi = 0.5$ and $\alpha = 0.5$, respectively.

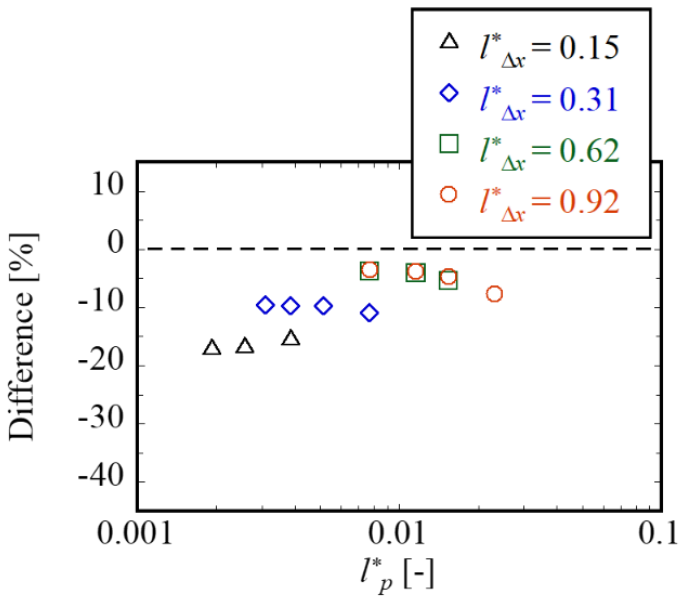

Figure 5.13. Difference of F_{LAP} from the results of the SE solver as a function of l^*_p.

5.9.2.2 Capillary force

Figure 5.14 shows the difference of F_{CAP} obtained from (a) Model A and (b) Model B from the results of the SE solver as a function of l_p^*. In Figure 5.14(a), for a given l_p^*, the results do not converge as $l_{\Delta x}^*$ is increased from 0.15 to 0.92. This implies that even higher gas-liquid interface resolution is required to achieve mesh-independent simulation. In addition, the calculated F_{CAP} value is largely influenced by l_p^*. On the other hand, in Figure 5.14(b), the results are not very sensitive to neither l_p^* nor $l_{\Delta x}^*$, and the difference from the SE results is smaller than that in Figure 5.14(a). Figure 5.15 shows the fields of (a) $\boldsymbol{f}_s$ and (b) $\boldsymbol{f}_{ccf}$ which are used for Model A and B, respectively.

The free surface constructed with the IFS model usually has a point with large curvature where the free surfaces immersed from different locations on the contact line meet. In Figure 5.15(a), that point is near the particle centre, and the value of $\boldsymbol{f}_s$ becomes significantly large. This requires a thin gas-liquid interface with high resolution to achieve accurate calculation. On the other hand, Model B does not have such a problem and $\boldsymbol{f}_{ccf}$ can be easily calculated from smooth curvature as demonstrated in Figure 5.15(b). This may explain the difference in accuracy between Models A and B in Figure 5.14. It can be concluded that Model B can give more accurate results than Model A.

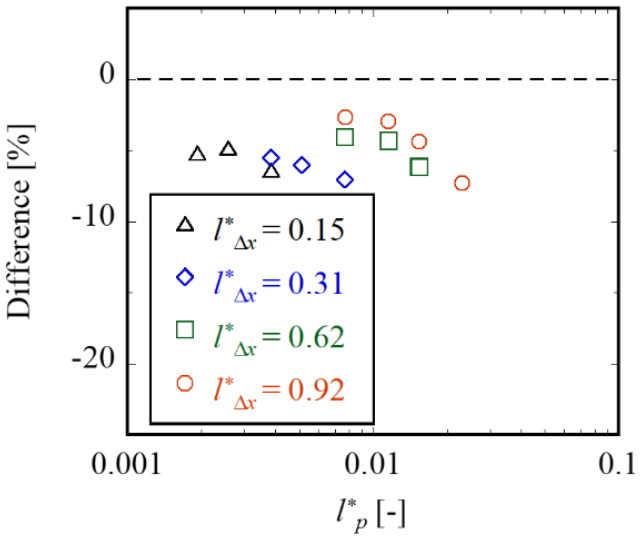

(a)

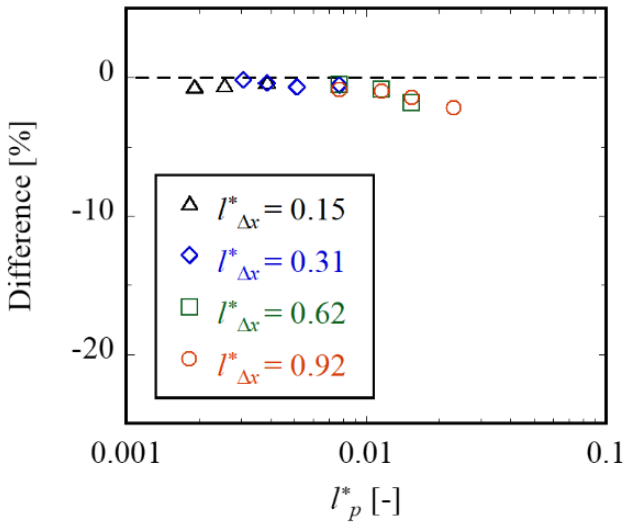

(b)

Figure 5.14. Difference of F_{CAP} from the results of the SE solver as a function of l_p^*; (a) Model A and (b) Model B.

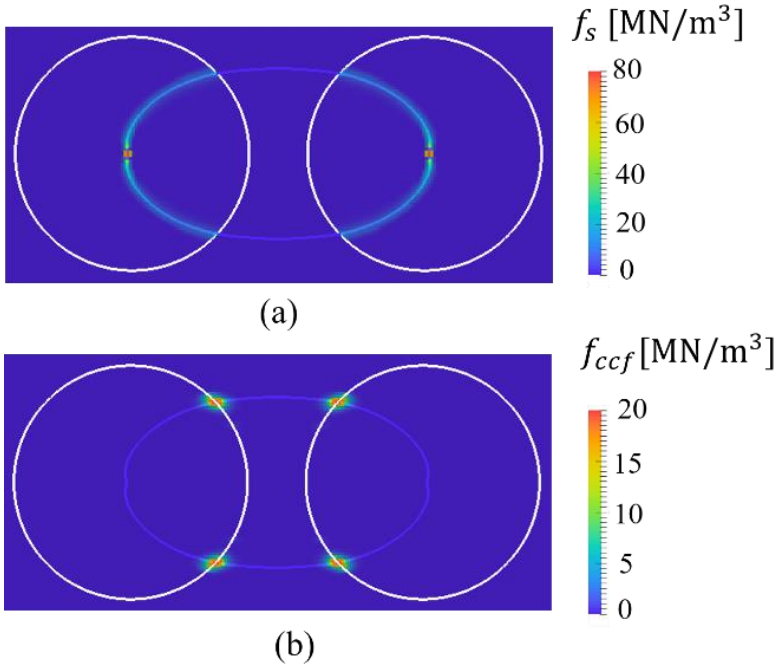

Figure 5.15. Fields of (a) f_s and (b) f_{ccf} calculated with $l^*_{\Delta x} = 0.62$, $l^*_p = 0.0077$ and $\delta^* = 0.025$. The white line shows $\chi = 0.5$, and the isoline of $\alpha = 0.5$ is coloured with f_s and f_{ccf} values.

5.9.2.3 Contact angle

The contact angle is fixed to 60° in Sections 5.9.2.1 and 5.9.2.2. This section examines the liquid bridge force with the contact angle varying from 30° to 150°, i.e. from the hydrophilic to hydrophobic particles. Based on the results in Section 5.9.2.1 and 5.9.2.2, the simulation is performed with $l^*_{\Delta x} = 0.62$, $l^*_p = 0.0052$ and $\delta^* = 0.0042$, and Model B is used for the calculation of the capillary force.

The resultant α fields with different contact angles are shown in Figure 5.16. F^*_{CAP}, F^*_{LAP} and F^*_{LB} exerted on the particle on the right in Figure 5.9, that are F_{CAP}, F_{LAP} and F_{LB} normalised by σr_p, respectively, are compared to the results obtained from the SE solver and plotted in Figure 5.17. Good agreement can be seen between the simulation and SE solver results. This proves that the resolved CFD–DEM model developed with the controllable gas-liquid interface and IFS model is capable of predicting the liquid bridge force from hydrophilic to hydrophobic particles

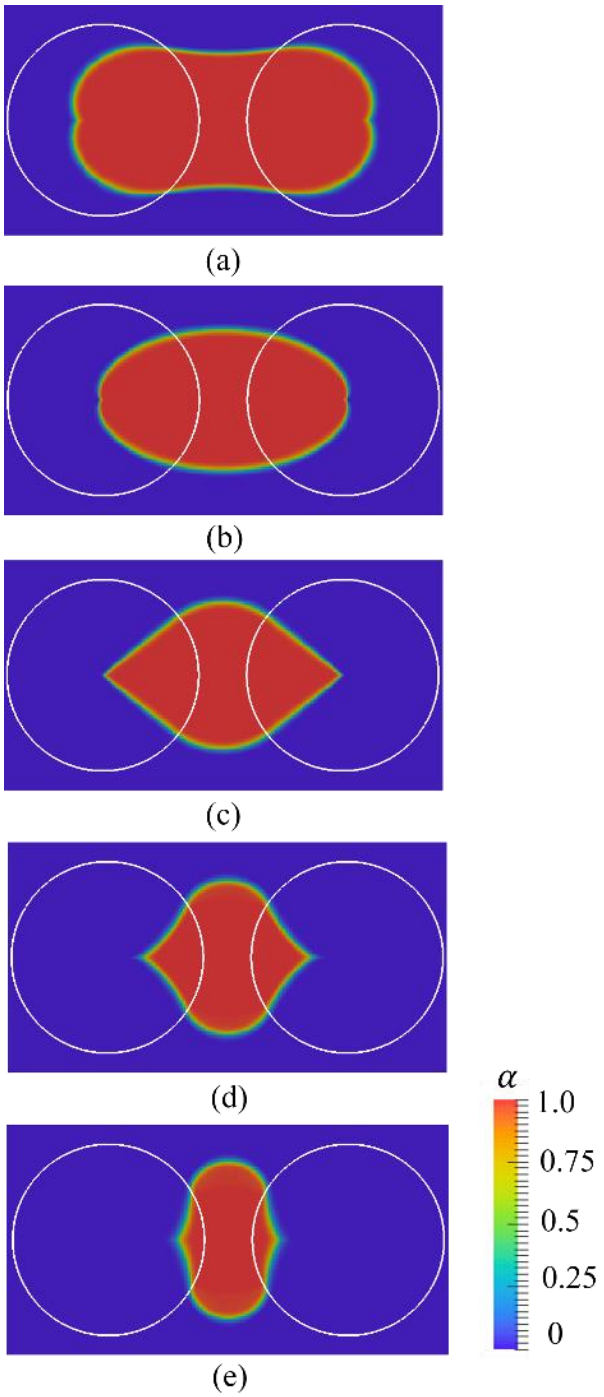

Figure 5.16. Static liquid bridges with different contact angle; (a) 30°, (b) 60°, (c) 90°, (d) 120° and (e) 150°.

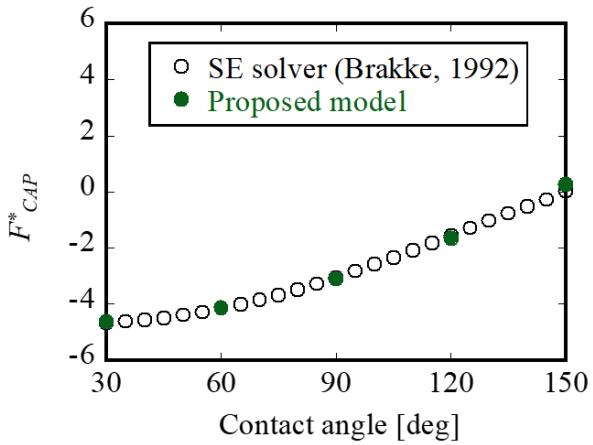
6
4
2
0
-2
-4
-6
30
60
90
120
150
F^*_{CAP}
SE solver (Brakke, 1992)
Proposed model
Contact angle [deg]

(a)

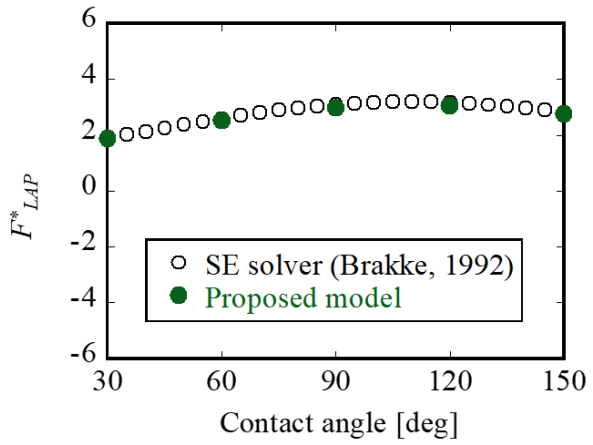
6
4
2
0
-2
-4
-6
30
60
90
120
150
F^*_{LAP}
SE solver (Brakke, 1992)
Proposed model
Contact angle [deg]

(b)

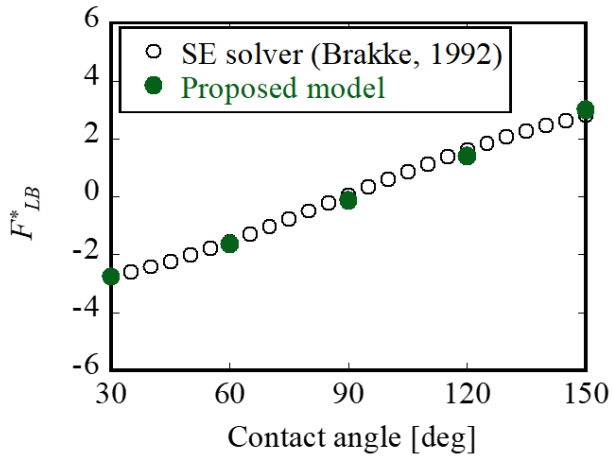

(c)

Figure 5.17. Dimensionless liquid bridge forces; (a) F^*_{CAP}, (b) F^*_{LAP} and (c) F^*_{LB}.

5.9.3 Particle falling into liquid

This section discusses the applicability of the resolved CFD–DEM model to a dynamic system by performing simulation of a particle falling into liquid. The simulation conditions are based on the experiment by Liu and Ding [139]. The simulation domain is $8d_p \times 8d_p \times 4.5d_p$. A schematic diagram of the system is shown in Figure 5.18.

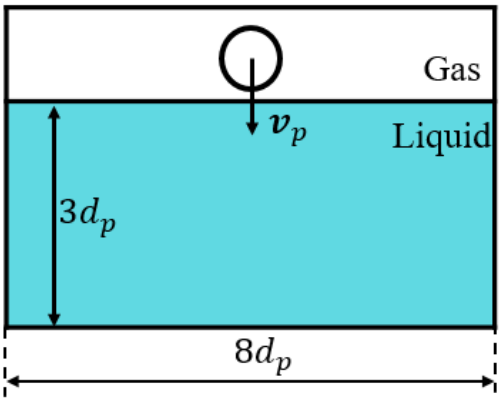

Figure 5.18. Schematic of particle falling into liquid.

The particle is 2 mm in diameter and 7800 kg/m^3 in density, and initially placed at $0.25d_p$ above the gas-liquid interface (i.e. at $0.75d_p$ for particle centroid) with a downward velocity. The gas-liquid interface is initially located at $3d_p$ from the bottom boundary and is $8d_p$ both in width and depth. Zero gradient boundary condition is applied for all the boundaries. Gravity is considered in the simulation. The contact angle measured in experiment is $100^o \pm 10^o$. However, this is the static contact angle and should be different from the dynamic contact angle. A dynamic contact angle model should be required to properly capture this event. However, it is still an open question what is the appropriate dynamic contact angle for such a complex flow in this system. Hence, this study employs a somewhat large contact angle, i.e. 120°, representing the advancing contact angle. Note that a similar treatment is also used by Liu and Ding in their simulation. The calculation conditions are listed in Table 5.4.

Table 5.4. Calculation conditions of particle falling into liquid.

Properties	Value
Particle diameter d_p [mm]	2
Particle density ρ_p [kg/m3]	7800
Liquid density ρ_l [kg/m3]	1000
Liquid viscosity μ_l [Pa·s]	0.01
Gas density ρ_g [kg/m3]	1.2
Gas viscosity μ_g [Pa·s]	1.8×10^{-5}
Surface tension coefficient σ [N/m]	0.072
Contac angle θ [deg]	120
t_d [s]	1×10^{-4}

The Weber number (We) and Reynolds number (Re) are defined as:

$$\mathrm{We} = \frac{\rho_l v_p^2 d_p}{\sigma} \tag{5.73}$$

$$\mathrm{Re} = \frac{\rho_l v_p d_p}{\mu_l} \tag{5.74}$$

where v_p is the magnitude of the impact velocity of the particle to the gas-liquid interface. The impact velocity used is 0.71 m/s to give $\mathrm{We} = 14$ and $\mathrm{Re} = 1420$. Based on the results obtained in Section 5.9.2.1, $l_p^* = 0.0077$ and $\delta^* = 0.0063$ are chosen as the gas-liquid and fluid-solid interface thicknesses, respectively, and $l_{\Delta x}^* =$

0.62 is used as the gas-liquid interface resolution. The capillary force is calculated using Model B.

Figure 5.19 shows snapshots of the simulation results at three different dimensionless times $t^* = \frac{t \times v_p}{d_p}$ (a) with and (b) without using the interface compression in Eq. (5.6) . Note that t^* = 0 is taken when the particle first comes into contact with the gas-liquid interface. It is observed that the three-phase contact line cannot move easily on the top half of the particle surface due to the large contact angle, and creates a gas cavity above the particle ($t^* = 1.69$). As the particle moves downwards, the three-phase contact line is almost pinned and a neck appears in the cavity ($t^* = 2.57$). When the neck is completely closed, a large upward velocity is induced to shoot up the gas-liquid interface, while small amount of gas bubble is entrained in the liquid ($t^* = 2.75$). It can be seen that the simulation results in Figure 5.19(b) suffer a significant amount of interface smearing at $t^* = 2.75$ since the numerical diffusion becomes more pronounced with a large fluid velocity. On the other hand, the numerical diffusion is largely suppressed by using the interface compression in Figure 5.19(a).

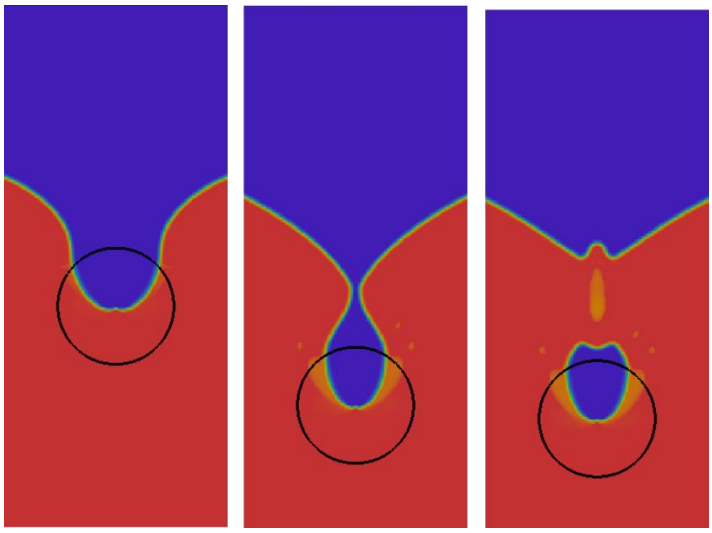

(a)

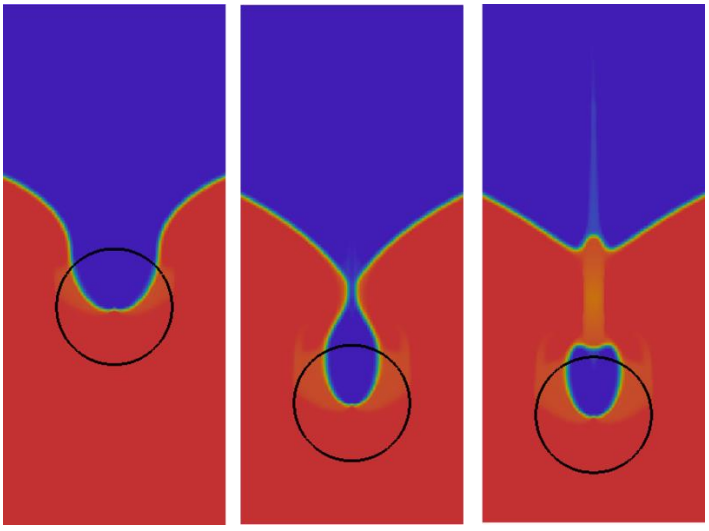

(b)

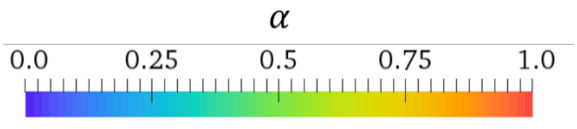

Figure 5.19. Snapshots of particle falling into liquid at t^*= 1.69, 2.57 and 2.75 from left to right (a) with and (b) without interface compression term.

Figure 5.20 shows the comparison between the experiment and simulation when the interface compression term Eq. (5.6) is considered. Although a constant contact angle is applied in this section, good qualitative agreement can be seen in terms of the behaviour of the gas-liquid interface as well as the particle position with time. In general, it can be concluded that the resolved CFD–DEM model developed can capture the dynamic behaviour of a three-phase system. However, a dynamic contact angle model is required in order to be consistent with theory.

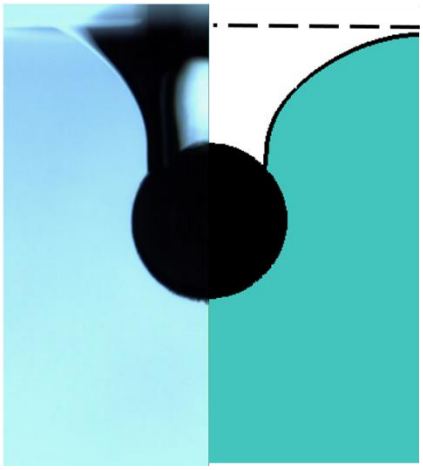

(a)

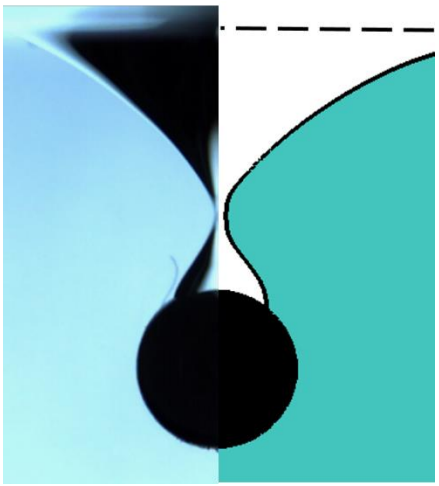

(b)

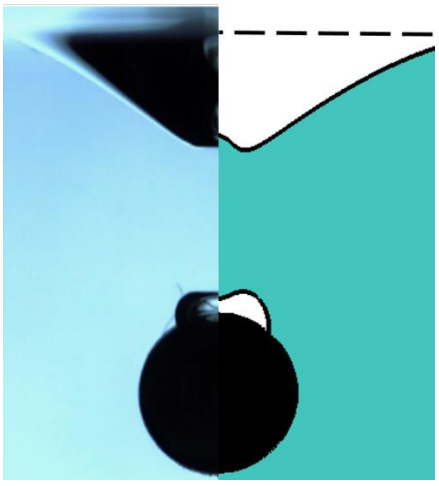

(c)

Figure 5.20. Comparison between the experiment [139] (left) and the simulation (right) at (a) t^*= 1.69, (b) t^*= 2.57, (c) t^*= 2.75. The dashed line indicates the initial height of the gas-liquid interface.

5.9.4 Dynamic liquid bridge with a free-falling particle

In this section, the resolved CFD–DEM model developed is applied to simulate a dynamic liquid bridge between two particles of 6.35 mm in diameter and 7800 kg/m^3 in density. The simulation conditions are based on the experiment by Kan et al. [17]. The particles are aligned vertically and initially in contact. Liquid of 2.6 mm^3 in volume is generated between the particles and relaxed to form a static liquid bridge. The upper particle is fixed in space and the lower particle starts to free fall at $t = 0$ ms. Gravity is considered in the simulation. The calculation conditions are listed in Table 5.5. Based on the results obtained in Section 5.9.2.1, $l_p^* = 0.0052$ and $\delta^* = 0.0042$ are used as the gas-liquid and fluid-solid interface thicknesses, respectively, and the interface resolution is $l_{\Delta x}^* = 0.62$. The contact angle is assumed to be constant. The interface compression is included since it is useful for a dynamic system, and Model B is applied for the calculation of the capillary force.

Table 5.5. Calculation conditions for dynamic liquid bridge with a free-falling particle.

Property	Value
Particle diameter d_p [mm]	6.35
Particle density ρ_p [kg/m3]	7800
Liquid density ρ_l [kg/m3]	818
Liquid viscosity μ_l [Pa·s]	0.818×10^{-3}
Gas density ρ_g [kg/m3]	1.184

Gas viscosity μ_g [Pa·s]	1.82×10^{-5}
Surface tension coefficient σ [N/m]	0.0169
Liquid volume V_l [mm3]	2.6
Contact angle θ [deg]	30
t_d [s]	1×10^{-4}

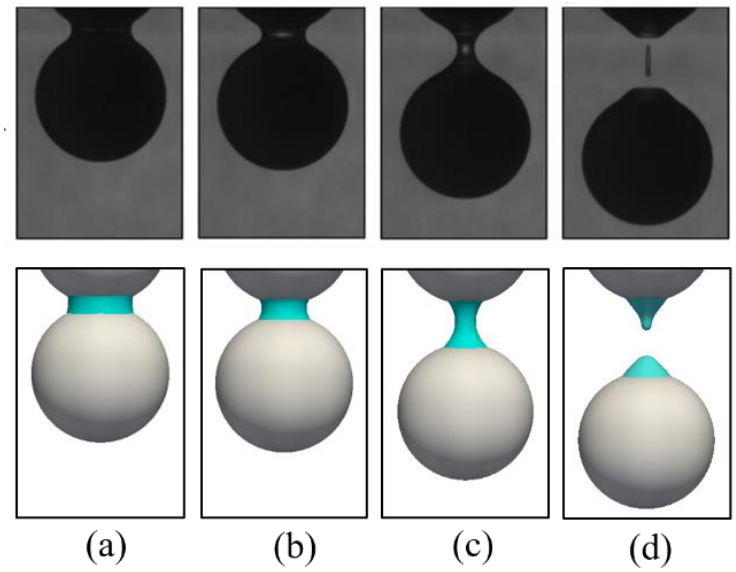

Figure 5.21. Snapshots of dynamic liquid bridge. The top and bottom show the results obtained from the experiment [17] and simulation, respectively; (a) $t = 0$ ms (b) $t = 10$ ms (c) $t = 20$ ms and (d) $t = 26$ ms.

Figure 5.21(a), (b), (c) and (d) show snapshots of the dynamic liquid bridge at $t = 0$, 10, 20 and 26 ms, respectively. It can be seen that the simulation results are in good agreement with the experiment in terms of the liquid bridge shape. However, the

satellite droplet at $t = 26$ ms is not captured by the simulation since it is too small to be resolved with the interface thickness and resolution used. The distance between the two particles with time is plotted in Figure 5.22. Due to the attractive force induced by the liquid bridge, the particles in the experiment and simulation fall more slowly than the free-falling particle without a liquid bridge although the difference is subtle because of the large mass of the particle. Both the experiment and simulation results almost fall into the same curve and the time for the bridge rupture is also comparable.

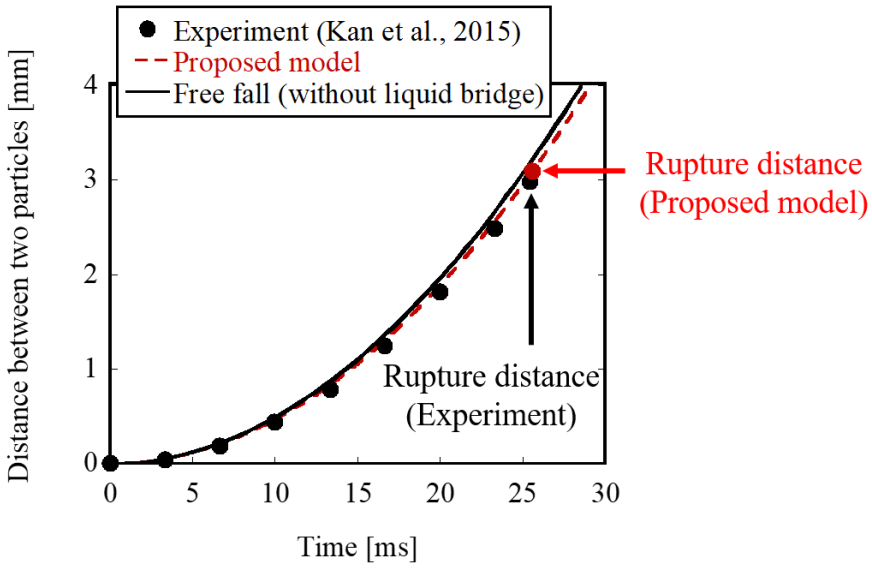

Figure 5.22. Temporal change of the distance between two particles with dynamic liquid bridge.

5.10 Model applications

5.10.1 Influence of wettability on two colliding particles with liquid bridge

In the study of wet particulate flows such as wet granulation and particle coating, it is important to understand the behaviour of colliding particles connected with a liquid bridge. This section applies the resolved CFD–DEM model developed to investigate the impact of a liquid bridge on the motion of two colliding particles. Figure 5.23 is a schematic diagram of the system to be simulated. The simulation domain is $6.5 \times 14 \times 6.5$ mm^3 in the x-, y- and z-directions. Gravity is not considered in the simulation. The particle is 0.5 mm in diameter, 2500 kg/m^3 in density and 10 GPa in Young's modulus. Two particles are initially separated with a distance of $s = 0.7d_p$. A spherical droplet of $d_d = 0.5d_p$ in diameter is placed in between the particles. The contact angles tested are assumed to be constant, i.e. $\theta = 30^{\circ}, 60^{o}, 90^{o}$ and 120° in order to evaluate the impact of particle wettability. The particles are initially enforced to move towards each other with a velocity magnitude of 0.125 m/s. The calculation conditions are listed in Table 5.6. Based on the results obtained in Section 5.9.2.1, $l_p^* = 0.0052, l_d^* = 0.01$ and $\delta^* = 0.0042$ are chosen as the gas-liquid and fluid-solid interface thicknesses, respectively, and $l_{\Delta x}^* = 0.62$ is used as the gas-liquid interface resolution. The interface compression is included and the capillary force is calculated with Model B.

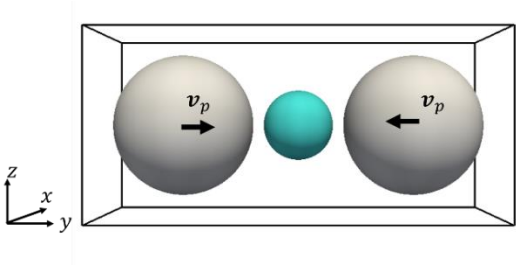

Figure 5.23. Schematic of two particles and a spherical liquid droplet.

Table 5.6. Fluid and particle properties for the simulation of two colliding particles with liquid bridge.

Properties	Value
Liquid density ρ_l [kg/m3]	1000
Liquid viscosity μ_l [Pa·s]	0.001
Gas density ρ_g[kg/m3]	1.2
Gas viscosity μ_g [Pa·s]	1.8×10^{-5}
Surface tension coefficient σ [N/m]	0.072
Contact angle θ [deg]	30, 60, 90, 120
Particle diameter d_p [mm]	0.5
Particle density ρ_p [kg/m3]	2500
Young's modulus [GPa]	10
Poisson's ratio [-]	0.25
Restitution coefficient [-]	0.9
Friction coefficient [-]	0.3
t_d [s]	1×10^{-4}

Snapshots of the simulation results are shown in Figure 5.24(a) and (b) for the cases of $\theta = 30^{o}$ and 120° representing hydrophilic and hydrophobic cases, respectively. In Figure 5.24(a), the small contact angle (good wettability) causes the quick spreading of the liquid over the particle surface right after the particle-liquid contact. The liquid spreading is faster than the particle movement and makes the bridge neck to be small. The liquid bridge then ruptures and stays on the particle surface as a cap. The liquid caps come into contact and forms a liquid bridge again. After that, the particles collide to each other and rebound. The concave liquid bridge continuously pulls the particles, and the rebounded particles change the direction again. The particles then move towards each other for the second collision. In Figure 5.24(b), the liquid spreading is limited because of the large contact angle and the liquid bridge has a convex shape. This makes the pressure inside the bridge high and causes a repulsion force. The particles move towards each other and come close, but do not collide. The particles then gradually accelerated in the opposite directions until they reach nearly the impact velocity. It is noted that the liquid bridge becomes asymmetric at $t = 2.4$ ms, which is not likely to happen in reality since the system is symmetric. This is because the contact area between the particle and liquid is small, and the liquid bridge can easily move with the spurious current that is not completely symmetric due to the numerical error.

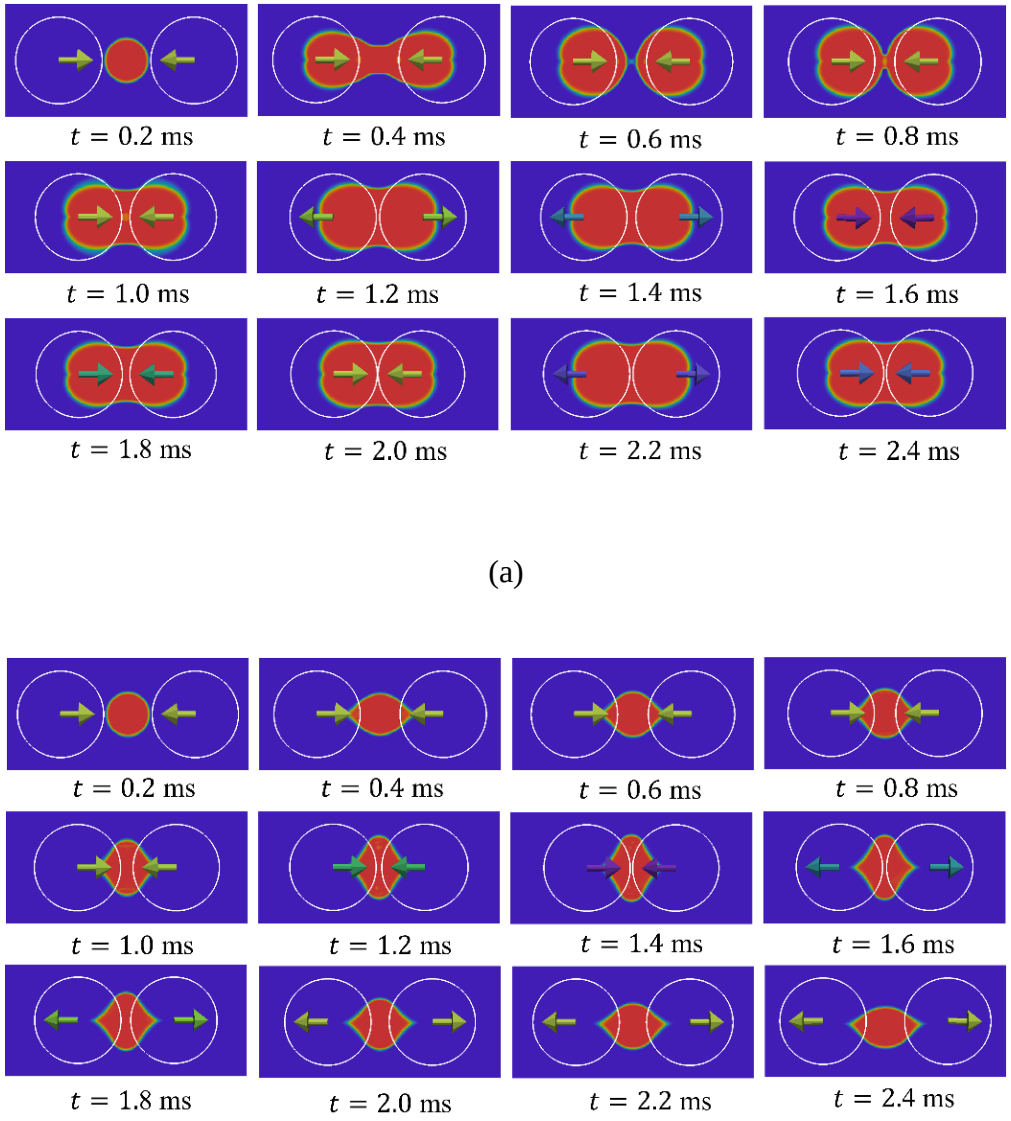

Figure 5.24. Time evolution of particles with liquid bridge with different contact angles; (a) $\theta = 30^{o}$ and (b) $\theta = 120^{o}$. The arrows show the particle velocity.

Figure 5.25 shows the velocity of the particle on the left. At the approaching stage (before the particle-liquid contact), the particle moves with a constant velocity from $t = 0$ to 0.35 ms. In the case of $\theta = 30^{o}, 60^{o}$ and 90°, rapid velocity increase can be seen after the reformation of the liquid bridge at t = 0.8 ms due to the attractive liquid bridge force. Right after the collision, the particle velocity becomes negative, i.e. moving to the opposite direction. The liquid bridge continuously pulls the particle and the rate of change of the particle velocity is more or less constant until the particles collide again. In the case of $\theta = 120^{o}$, right after the particle-liquid contact at $t = 0.35$ ms, there is a subtle increase of the particle velocity due to the capillary force. However, as the particles come closer, the force due to the Laplace pressure becomes dominant and the velocity decreases. Sudden velocity change cannot be seen which implies that there is no particle collision. It is concluded that the wettability of the particle surface is one of the dominating factors which influences the behaviour of the particles connected with a liquid bridge.

Although the assumed constant contact angles are applied in this section for simplicity, the resolved CFD-DEM model developed can give general feature of wetting effect on two colliding particles connected with a liquid bridge. A dynamic contact angle (i.e. advancing and preceding angles) should be applied in order to get more realistic results. In addition, a lubrication model is also required in order to improve the accuracy.

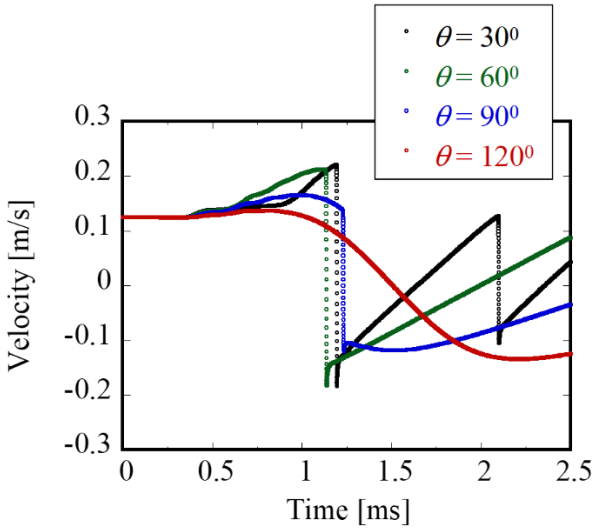

Figure 5.25. Time evolution of particle velocity.

5.10.2 Analysis of hydrodynamic force acting on two colliding particles with liquid bridge

Section 5.10.1 shows that the particle velocity is drastically decreased when it rebounds. This section investigates the cause of the velocity decline and hydrodynamic force acting on two colliding particles with a liquid bridge. The simulation conditions are the same the ones of Section 5.10.1, except for the constant contact angle $\theta = 45^{o}$ which is applied in this section. The time evolution of the particle on the left in Figure 5.23 is shown in Figure 5.26 focusing on the velocity profile during the second collision. The behaviour of two moving particles with a liquid bridge is discussed regarding four continuous stages: I (before collision), II (collision), III (rebound) and

IV (subsequence), as shown in Figure 5.26. Stage I takes place before collision when the particles are approaching toward each other with almost constant velocity. Then, the particle velocity is then rapidly changed due to the collision in stage II. The particle velocity is drastically decreased in stage III where the two particles rebound whilst it is almost constant in stage IV.

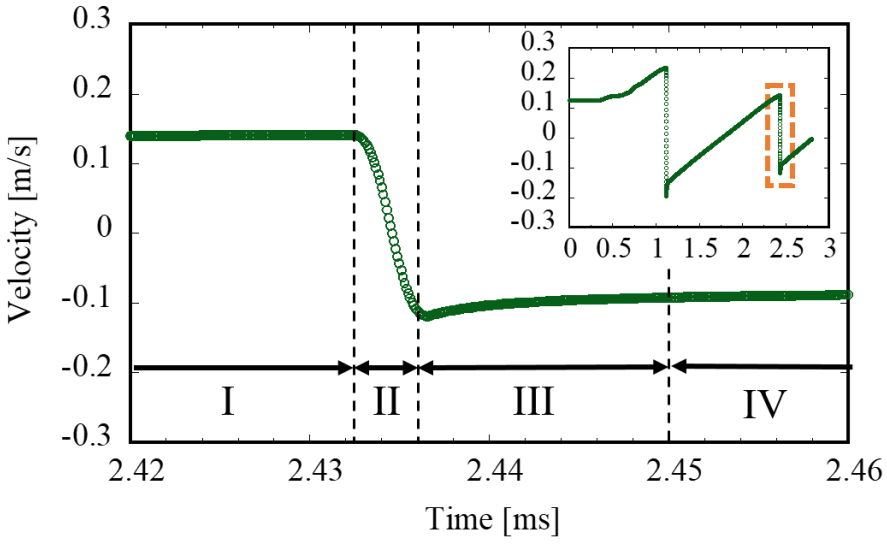

Figure 5.26. Time evolution of particle velocity with the contact angle of 45°.

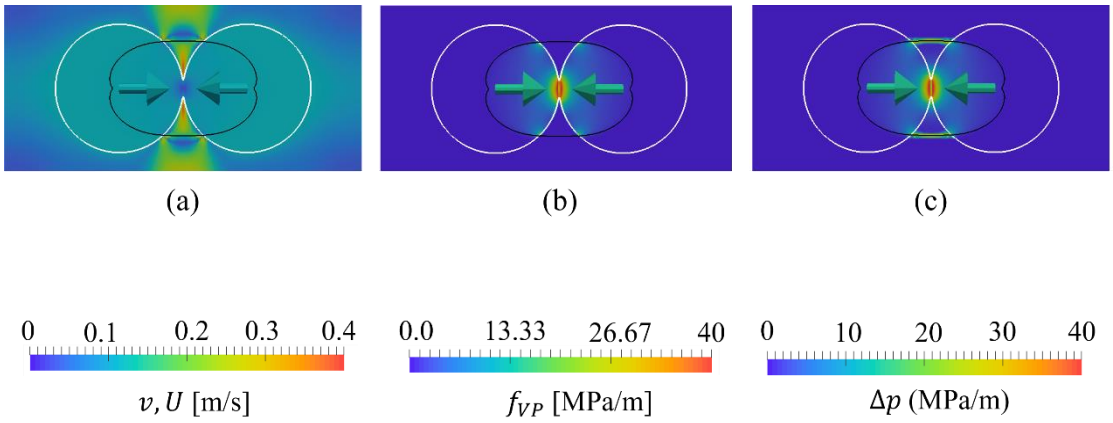

Figure 5.27. Instantaneous fluid velocity, penalty term and pressure gradient fields in stage I at $t = 2.432$ ms. (a): fluids velocity U, (b): penalty term f_{VP}; (c) pressure gradient Δp. The arrows show the particle velocity v. The white and black lines show $\chi = 0.5$ and $\alpha = 0.5$, respectively.

At stage I, squeeze flow is found near the narrow gap between the two particles due to the particles approaching as shown in Figure 5.27(a). As a result, large pressure and penalty term are also observed as shown in Figure 5.27(b) and Figure 5.27(c), respectively. The hydrodynamic force acting on the particle in stage I is related to the lubrication force due to the drainage of the interstitial fluid in the small gap between two particles.

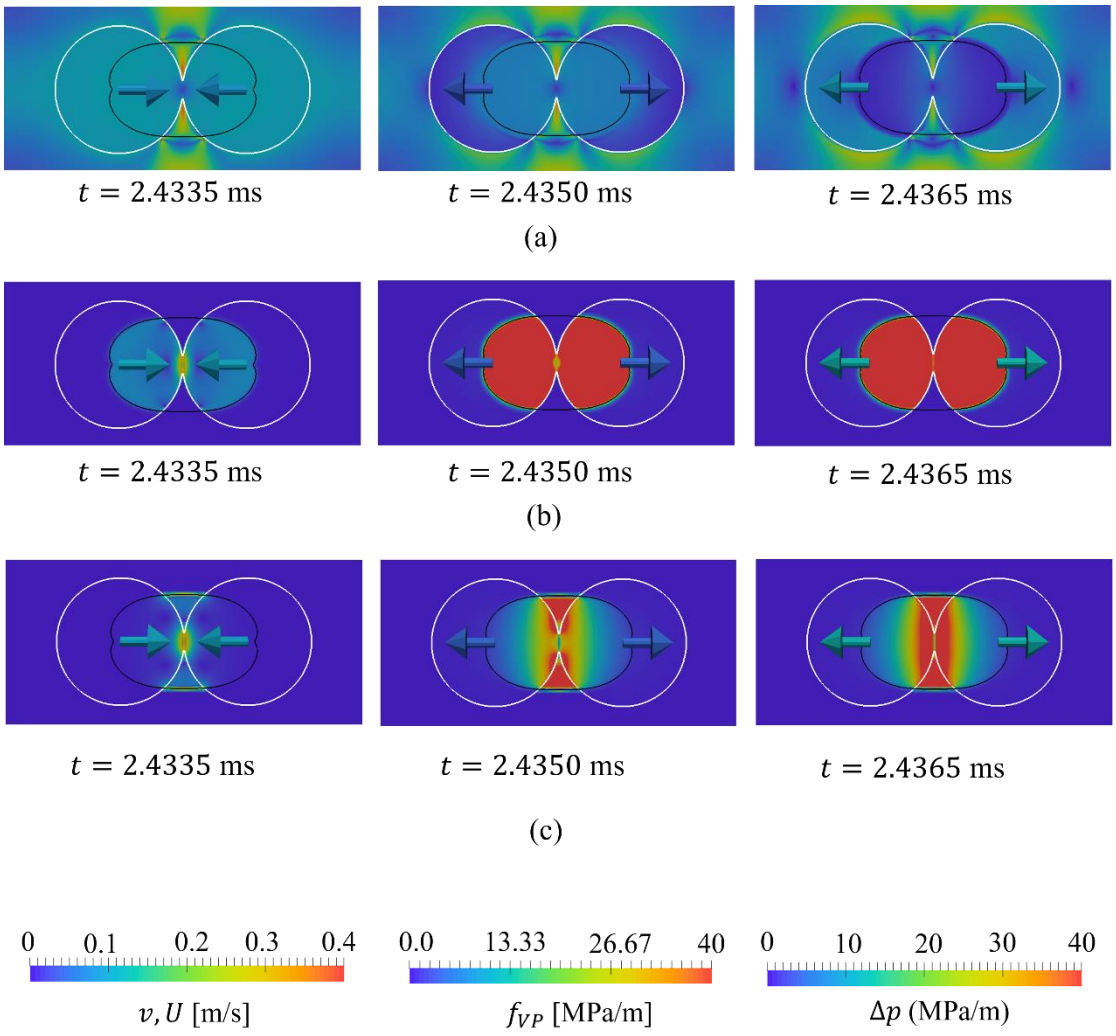

Figure 5.28. Instantaneous fluid velocity, penalty term and pressure gradient fields in stage II. (a): fluids velocity U, (b): penalty term f_{VP}; (c) pressure gradient Δp. The arrows show the particle velocity v. The white and black lines show $\chi = 0.5$ and $\alpha = 0.5$, respectively.

At stage II, (from $t\sim$ 2.4327 to 2.4368 ms), the two particles collide and their moving directions are changed. Squeeze flow still remains in the liquid bridge as shown in Figure 5.28(a). After changing their moving directions, the particles acceleration becomes very large leading to a large penalty term in the immersed liquid as shown in Figure 5.28(b). When two particles are accelerated due to the contact force, there is a corresponding acceleration of the liquid bridge. The rate of change of liquid velocity is assumed to be the same as the rate of change of particle velocity so that the first term in the right-hand side in Eq. (5.2) becomes dominant. The rate of change of liquid velocity approximately equals 63.4 MPa/m while the pressure gradient in the liquid barged body is uniformly equal to 31.5 MPa/m approximately as shown in Figure 5.30(b). The hydrodynamic force in stage II may be associated with the force required to accelerate the fluid surrounding the moving particle. This phenomenon may be related to the Virtual mass effect [140]. However, the lubrication effect may still remain in this second stage.

It is noted that there is a large difference in velocity between the immersed liquid and the particles when the particles are largely accelerated from $t\sim$ 2.435 to2.4365 ms as shown in Figure 5.28(a). The optimal permeability shown in Section 4.3 is obtained from the zeroth order normal velocity and is tested with Re up to 100 in Chapter 4. Hence, a higher leading order normal velocity should be applied for the optimal permeability in order to eliminate the difference in velocity between fluid and particle when a large acceleration occurs.

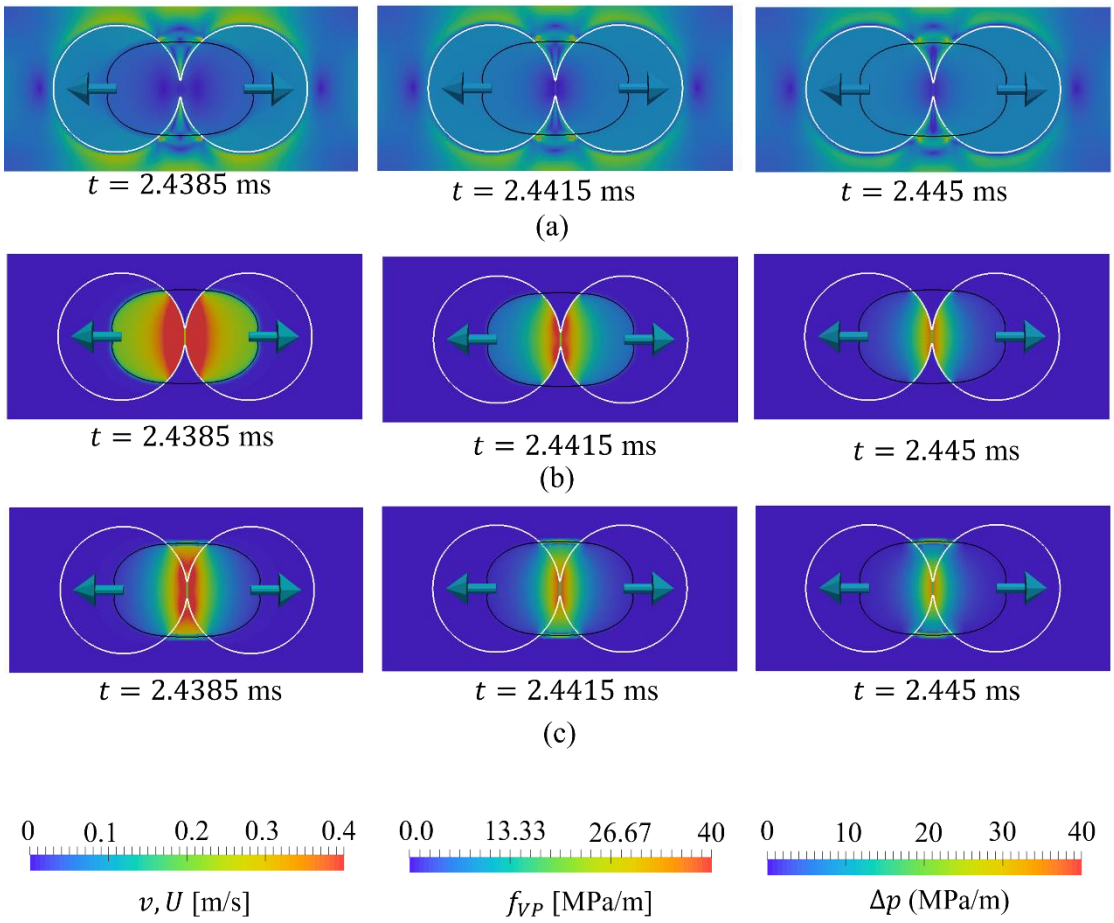

Figure 5.29. Instantaneous fluid velocity, penalty term and pressure gradient fields in stage III. (a): fluids velocity U, (b): penalty term f_{VP}; (c) pressure gradient Δp. The arrows show the particle velocity v. The white and black lines show $\chi = 0.5$ and $\alpha = 0.5$, respectively.

At stage III (from $t\sim$ 2.4368 to 2.45 ms), the rate of change of particle velocity is much smaller than in stage II so that the difference in velocity between the immersed liquid and the particles is mitigated as shown in Figure 5.29(a). In addition, the velocity field of the squeeze flow is also decreased due to the flow development in the liquid bridge. As a result, the penalty term and pressure gradient are gradually declined as shown in Figure 5.29(b) and (c), respectively. The hydrodynamic force associated with the fluid flow development may be linked to the Basset force [141] which may cause the drastically decrease in particle velocity in stage III.

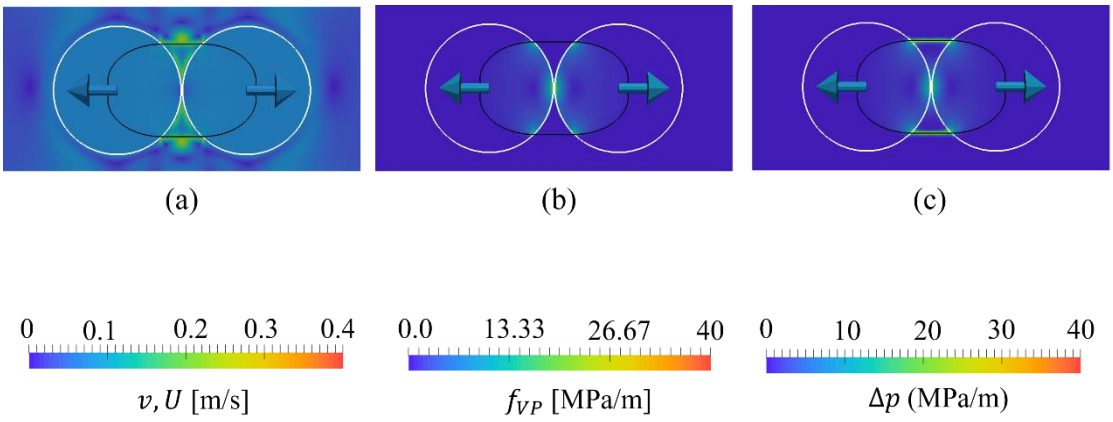

Figure 5.30. Instantaneous fluid velocity, penalty term and pressure gradient fields in stage I at $t = 2.4675$ ms. (a): fluids velocity U, (b): penalty term f_{VP}; (c) pressure gradient Δp . The arrows show the particle velocity v. The white and black lines show $\chi = 0.5$ and $\alpha = 0.5$, respectively.

At stage IV, the velocity in the liquid bridge increases after squeeze flow as shown in Figure 5.30(a) so that the liquid flow is fully developed in stage IV. A slightly large penalty term and pressure gradient still remain at the narrow gap between two particles as shown in Figure 5.30(b) and Figure 5.30(c), respectively. It could be concluded that the lubrication force may be the dominant factor of stage IV.

5.11 Summary

In summary, this chapter develops the resolved CFD–DEM model using the controllable gas-liquid interface thickness and the IFS model for the study of gas-liquid-solid three-phase flows. The gas-liquid interface is controlled by the diffuse interface parameters (i.e. M and l) leading to the improvement of the calculations of surface tension and capillary forces. The VP method is applied for the calculation of the hydrodynamic interaction force between fluids and particles. The value of the colour function inside the particle domain is set using the Immersed Free Surface (IFS) model.

This chapter reveals the influence of the parameters for the diffuse interface term controlling the gas-liquid interface thickness (and hence resolution) on the accuracy of the surface tension force calculation. Two of the major methods to calculate the capillary force in the literature, i.e. Model A proposed by Fujita et al. [71] and Model B by Washino et al. [23] (which is also known as the CCF model), are compared in this work. Four kinds of simulations are performed in order to evaluate the diffuse interface parameters and compare two capillary force model as well as validate the IFS model

for particle wettability: (i) a spherical droplet, (ii) a static liquid bridge between two particles, (iii) a particle falling into a liquid and (iv) a dynamic liquid bridge with a free-falling particle. The key findings in each test case are as follows:

(i) It is theoretically derived that the critical time step for the diffuse interface has the following relationship with the cell size and diffuse interface parameters:

$$\Delta t_c \propto \frac{\Delta x^4}{M l^2}$$

Gas-liquid interface resolution has a large impact on the accuracy of the surface tension force calculation. In order to yield the mesh-independent Laplace pressure, $l_{\Delta x}^* = 0.62$ is required. The artificial gas-liquid interface thickness also induces a model error, and l_d^* has to be smaller than 0.013 to obtain reasonable results. The interface compression increases the error by a few percent and not recommended to be used for static cases.

(ii) The thickness of the particle-fluid interface can affect the accuracy of F_{LAP} in the simulation. $\delta^* = 0.0031$ is required to obtain converged F_{LAP}, and it is recommended to use $l_{\Delta x}^* \geq 0.62$ and $l_p^* < 0.012$ for reasonable computation. F_{CAP} calculated by Model A gives less accurate results than that by Model B. The convergence cannot be obtained by Model A with the gas-liquid interface resolution and thickness tested. In contrast, F_{CAP} calculated by Model B is not very sensitive to the gas-liquid interface resolution and thickness and more accurate. It is also found that the resolved CFD–DEM model developed is

capable of predicting the liquid bridge force accurately from hydrophilic to hydrophobic particles.

(iii) A significant amount of interface smearing is found when the gas-liquid interface deforms drastically. The problem can be effectively suppressed by considering the interface compression. Good qualitative agreement can be seen between the experiment and simulation in terms of the interface deformation pattern as well as the entrainment of the gas bubble although a dynamic contact angle model is required for more quantitative comparison.

(iv) Good agreement is found between the experiment and simulation in terms of the liquid bridge shape and the rupture. However, the generation of the satellite droplet cannot be seen in the simulation unless smaller gas-liquid interface thickness and higher resolution are employed.

In order to demonstrate the applicability of the resolved CFD–DEM model developed to the complex gas-liquid-solid three-phase system, simulation of two colliding particles with a liquid bridge is performed with different contact angles. Different behaviours of the particles and fluids are found depending on the contact angle (and hence the wettability of particle surface). The liquid spreading is very fast in the case of $\theta = 30^{o}$ where the liquid bridge ruptures even before the particle collision. When the contact angle is increased, i.e $\theta = 60^{o}$, there is no liquid rupture. On the other hand, the liquid spreading is limited in the case of $\theta = 120^{o}$. The particles do not collide due to the repulsion force induced by the convex liquid bridge. In order to analyse the hydrodynamic force acting on two colliding particles with a liquid bridge,

the collision-rebound process is divided into four stages. Stage I (before collision) is mainly controlled by the lubrication force. Virtual mass and of Basset forces may be the main contributor when two particles are collided (in stage II) and rebounded (in stage III), respectively. After a rebound (stage IV), the liquid flow is fully developed and mainly controlled by the lubrication force.

Chapter 6

Conclusions

A resolved CFD–DEM model for gas-liquid-solid three-phase flows is developed in this study. The unique point of the model is that both particle-fluids and gas-liquid interfaces are represented as smooth transition regions with controllable interface thickness. The particle-fluids interface is described by using a smooth mask function in the framework of the VP method along with the optimal permeability [43]. The gas-liquid interface is captured using a colour function, and the thickness of the interface is controlled by employing both interface compression and diffuse interface techniques simultaneously [69]. The wetting of particle surface is expressed by the Immersed Free Surface (IFS) model. The accuracy of two capillary force models is also investigated in the IFS framework.

This last Chapter concludes the dissertation and is divided in two Sections. The first summarises the conclusions acquired from this work and the second makes suggestions for future work.

6.1 Conclusions

The results of the present study have been extensively assessed and discussed in the previous Chapters. In the following, the most important conclusions are summarised in terms of the particle-fluids interaction model, gas-liquid interface capturing method, wetting and capillary force models as well as model applications

6.1.1 Hydrodynamic interaction model between particles and fluids

Rigorous sensitivity analysis of the influence of particle-fluid interface thickness (thickness parameter) governing the optimal permeability on the hydrodynamic force between particles and fluid is carried out in Chapter 4. The study of particle-fluid interface thickness is also presented in Chapter 5 for the calculation of force due to Laplace pressure. The key findings are summarised below:

(i) The hydrodynamic force between particles and fluid (drag force) is accurately computed with the Reynolds number up to 100. The computed drag force especially for low Reynolds number flows in dilute cases, i.e. flow past a single particle and periodic array with packing fraction up to 0.3, is not very sensitive to the thickness parameter. Thus, a large thickness parameter, i.e. $\delta = d_p/20$ and $d_p/40$ (and hence large permeability) should be employed since the stable simulation time step is limited by the permeability. However, when the high Reynolds number or dense case are used, a small thickness parameter should be chosen since the boundary layer becomes thinner as the Reynolds number increases or the gap between particles need to be resolved accurately for the fluid flow, respectively.

(ii) When a particle approaches to the plane wall, a smaller thickness parameter is required to capture the lubrication effect. It is concluded from the simulation results that the error of the fluid force exerted on the particle can be universally characterised by the ratio between the gap and the thickness parameter. The error becomes larger when the ratio becomes smaller.

(iii) The thickness of the particle-fluid interface can affect the force due Laplace pressure in the simulation of a static liquid bridge between two particles as shown in Chapter 5. The smaller thickness of the particle-fluid interface helps to eliminate spurious current migrating into the particle domain fluid. It is found that dimensionless thickness parameter $\delta^* = 0.0031$ is required to obtain converged force due Laplace pressure.

6.1.2 Gas-liquid interface capturing method

The accuracy of the surface tension force calculation can be improved by employing appropriate gas-liquid interface thickness (through the controlled diffuse interface parameter) as shown in the simulation of the spherical droplet as well as a static liquid bridge between two particles in Chapter 5. The effectiveness of the interface compression term is also presented in the simulation of a particle falling into liquid. The key findings are summarised below:

(i) The critical time step for the diffuse interface has the relationship with the cell size and diffuse interface parameters as follows:

$$\Delta t_c \propto \frac{\Delta x^4}{M l^2}$$

(ii) Gas-liquid interface resolution mainly controls the accuracy of the surface tension force calculation. In order to yield the mesh-independent of the calculation of Laplace pressure, $l^*_{\Delta x} = 0.62$ is required.

(iii) Since the gas-liquid interface thickness is artificially generated, it also induces a model error. The dimensionless gas-liquid interface thickness corresponding

to the spherical droplet diameter l_d^* and particle diameter l_p^* has to be smaller than 0.013 in order to obtain reasonable results.

(iv) The interface compression term actively suppresses the significant amount of interface smearing when the gas-liquid interface deforms drastically.

(v) The satellite droplet cannot be captured in the simulation of liquid rupture between a stationary and a falling particle unless smaller gas-liquid interface thickness and higher resolution are employed.

6.1.3 Wetting and capillary force models

The IFS model is applied to smoothly express the contact angle through the immersed free surface solved in the interior region of particle. Two capillary forces models are presented in this work: Model A and Model B. In Model A, the capillary force and torque can be calculated by the volume integral of surface tension force over the true particle volume. On the other hand, the capillary force based on Model B is calculated by the surface tension converted to a body force and it is only considered at the particle-fluid interface region for the volume integral. The IFS model is validated by calculating the liquid bridge force between two stationary particles with different contact angle and comparing the simulation results with the experiments, i.e. a particle falling into liquid, dynamic liquid rupture between a stationary and a falling particle. The key findings are summarised below:

(i) The resolved CFD–DEM model developed with IFS model is able to predict the liquid bridge force accurately from hydrophilic to hydrophobic cases, i.e.

from 30° to 150°. It also can be applied to quantitatively capture the contact angle in dynamic case, i.e. a particle falling into liquid, dynamic liquid rupture between a stationary and a falling particle.

(ii) The capillary force calculated by Model B is more accurate results than Model A. In addition, Model B is not very sensitive to the gas-liquid interface resolution and thickness whilst Model A cannot give the convergence with the gas-liquid thickness and resolutions tested.

6.1.4 Model applications

In order to demonstrate the applicability of the resolved CFD–DEM model to the study of multiphase flows, two applications for fluid-solid two-phase flows, i.e. the prediction of the relative viscosity of suspensions and the fluidised beds with uniform density and binary mixture particles, are shown in Chapter 4. In addition, applications to gas-liquid-solid three-phase flows, i.e. two colliding particles with a liquid bridge are shown in Chapter 5. The key findings are summarised below:

(i) The resolved CFD–DEM model developed is able to estimate the relative viscosity of the suspensions with the packing fraction up to 0.3. At higher packing fraction, the lubrication effect as well as the effect of the top and bottom walls should be considered. The packing fractions of both the uniform density and binary mixture fluidised beds are comparable to that found from the Ergun equation. However, there is a slightly different in the particle volume fractions between the uniform density and binary mixture beds that

may be caused by the nonlinear relationship between the drag force and the packing fraction.

(ii) Depending on the wettability of particle surface, different behaviours of the particles and fluids are found: the liquid spreading is very fast in the hydrophilic case than that in the hydrophobic case. The particles do not collide due to the repulsion force induced by the convex liquid bridge in the hydrophobic case. When hydrodynamic force acting on two colliding particles with a liquid bridge is analysed, the collision-rebound process is divided into four stages. Virtual mass and Basset forces may dominate when two particles are collided (stage II) and rebounded (stage III), respectively. Before collision (stage I) and after rebound (stage IV), the particle-fluids interaction may be dominated by lubrication force.

6.2 Suggestions for future work

The resolved CFD-DEM model developed has some limitations that are addressed for the future research as follows:

(i) In Section 4.3, the optimal permeability is obtained from the leading order normal velocity, which is zeroth order. It is applied and tested with Re up to 100 in this study. For larger Reynolds flow regime, the optimal permeability presented in this study may not be valid. Hence, a higher leading order model error should be applied to derive the form for the optimal permeability.

(ii) The gas-liquid interface capturing method applied in Section 5.3 is very accurate in term of surface tension force calculation. However, $l^*_{\Delta x} = 0.62$ is required to resolved gas-liquid interface thickness that may increase the calculation cost since the resolution may become very large. For instance, it may require very high resolution in order to capture satellite droplet as shown Section 5.9.4. Hence, there is a room to improve the gas-liquid interface capturing method used in this study, i.e. applying density-scale model for interface curvature interpolation as proposed in Yokoi [64].

(iii) Lubrication effect should be added in the simulation in order to capture the physical phenomenon occurring in the cases where the particle collisions are important.

(iv) A dynamic contact angle model should be considered for model development in the future in order to improve the accuracy of the study of dynamic cases.

References

[1] D. Gidaspow, Multiphase Flow and Fluidization: Continuum and Kinetic Theory Descriptions, 1st ed., Academic Press, 1994.

[2] J.A.M. Kuipers, K.J. van Duin, F.P.H. van Beckum, W.P.M. van Swaaij, Computer simulation of the hydrodynamics of a two-dimensional gas-fluidized bed, Comput. Chem. Eng. 17 (1993) 839–858.

[3] T.B. Anderson, R. Jackson, A fluid mechanical description of fluidized beds: Comparison of Theory and Experiment, Ind. Eng. Chem. Fundam. 8 (1969) 137–144.

[4] P.A. Cundall, O.D.L. Strack, A discrete numerical model for granular assemblies, Geotechnique. 29 (1979) 47–65.

[5] Y. Tsuji, T. Kawaguchi, T. Tanaka, Discrete particle simulation of two-dimensional fluidized bed, Powder Technol. 77 (1993) 79–87.

[6] Y. Li, J. Zhang, L.S. Fan, Numerical simulation of gas-liquid-solid fluidization systems using a combined CFD-VOF-DPM method: Bubble wake behavior, Chem. Eng. Sci. 54 (1999) 5101–5107.

[7] M.S. van Buijtenen, W.J. van Dijk, N.G. Deen, J.A.M. Kuipers, T. Leadbeater, D.J. Parker, Numerical and experimental study on multiple-spout fluidized beds, Chem. Eng. Sci. 66 (2011) 2368–2376.

[8] F. Alobaid, J. Ströhle, B. Epple, Extended CFD/DEM model for the simulation of circulating fluidized bed, Adv. Powder Technol. 24 (2013) 403–415.

[9] D. Jajcevic, E. Siegmann, C. Radeke, J.G. Khinast, Large-scale CFD-DEM simulations of fluidized granular systems, Chem. Eng. Sci. 98 (2013) 298–310.

[10] K. Washino, H.S. Tan, M.J. Hounslow, A.D. Salman, Meso-scale coupling model of DEM and CIP for nucleation processes in wet granulation, Chem. Eng. Sci. 86 (2013) 25–37.

[11] H.R. Charles-Williams, R. Wengeler, K. Flore, H. Feise, M.J. Hounslow, A.D. Salman, Granule nucleation and growth: Competing drop spreading and infiltration processes, Powder Technol. 206 (2011) 63–71.

[12] V. Chouk, G. Reynolds, M. Hounslow, A. Salman, Single drop behaviour in a high shear granulator, Powder Technol. 189 (2009) 357–364.

[13] K. Murase, T. Mochida, Y. Sagawa, H. Sugama, Estimation on the strength of a liquid bridge adhered to three spheres, Adv. Powder Technol. 19 (2008) 349–367.

[14] N.G. Deen, M. van S. Annaland, J.A.M. Kuipers, Direct numerical simulation of complex multi-fluid flows using a combined front tracking and immersed boundary method, Chem. Eng. Sci. 64 (2009) 2186–2201.

[15] K. Washino, H.S. Tan, A.D. Salman, M.J. Hounslow, Direct numerical simulation of solid–liquid–gas three-phase flow: Fluid–solid interaction, Powder Technol. 206 (2011) 161–169.

[16] M. Fujita, O. Koike, Y. Yamaguchi, Direct simulation of drying colloidal suspension on substrate using immersed free surface model, J. Comput. Phys. 281 (2015) 421–448.

[17] H. Kan, H. Nakamura, S. Watano, Numerical simulation of particle-particle

adhesion by dynamic liquid bridge, Chem. Eng. Sci. 138 (2015) 607–615.

[18] X. Sun, M. Sakai, Direct numerical simulation of gas-solid-liquid flows with capillary effects: An application to liquid bridge forces between spherical particles, Phys. Rev. E. 94 (2016) 1–22.

[19] Y. Mino, S. Sakai, H. Matsuyama, Simulations of particulate flow passing through membrane pore under dead-end and constant-pressure filtration condition, Chem. Eng. Sci. (2018).

[20] J. Gu, S. Takeuchi, T. Kajishima, Influence of Rayleigh number and solid volume fraction in particle-dispersed natural convection, Int. J. Heat Mass Transf. 120 (2018) 250–258.

[21] K. Kushimoto, S. Ishihara, J. Kano, Development of ADEM–CFD model for analyzing dynamic and breakage behavior of aggregates in wet ball milling, Adv. Powder Technol. (2019).

[22] N.G. Deen, M. van S. Annaland, J.A.M. Kuipers, Direct numerical simulation of complex multi-fluid flows using a combined front tracking and immersed boundary method, Chem. Eng. Sci. 64 (2009) 2186–2201.

[23] K. Washino, H.S. Tan, M.J. Hounslow, A.D. Salman, A new capillary force model implemented in micro-scale CFD-DEM coupling for wet granulation, Chem. Eng. Sci. 93 (2013) 197–205.

[24] H. Kan, H. Nakamura, S. Watano, Effect of collision angle on particle-particle adhesion of colliding particles through liquid droplet, Adv. Powder Technol. (2018).

[25] Y. Mino, H. Shinto, Lattice Boltzmann method for simulation of wettable

particles at a fluid-fluid interface under gravity, Phys. Rev. E. (2020).

[26] C.S. Peskin, Numerical analysis of blood flow in the heart, J. Comput. Phys. 25 (1977) 220–252.

[27] E.R. Mittal, G. Iaccarino, Immersed boundary methods, Annu. Rev. Fluid Mech. 37 (2005) 239–261.

[28] R.P. Beyer, R.J. Leveque, Analysis of a one-dimensional model for the immersed boundary method, SIAM J. Numer. Anal. 29 (1992) 332–364.

[29] J. Mohd-Yusof, Combined immersed boundary/B-spline methods for simulation of flow in complex geometries, Cent. Turbul. Res. Annu. Res. Briefs1. (1997) 171–186.

[30] J. Kim, D. Kim, H. Choi, An Immersed-Boundary Finite-Volume Method for Simulations of Flow in Complex Geometries, J. Comput. Phys. 171 (2001) 132–150.

[31] Y.H. Tseng, J.H. Ferziger, A ghost-cell immersed boundary method for flow in complex geometry, J. Comput. Phys. 192 (2003) 593–623.

[32] J.K. Patel, G. Natarajan, Diffuse interface immersed boundary method for multi-fluid flows with arbitrarily moving rigid bodies, J. Comput. Phys. 360 (2018) 202–228.

[33] D. Kim, H. Choi, Immersed boundary method for flow around an arbitrarily moving body, J. Comput. Phys. 212 (2006) 662–680.

[34] F. Domenichini, On the consistency of the direct forcing method in the fractional step solution of the Navier-Stokes equations, J. Comput. Phys. (2008).

[35] N. Sato, S. Takeuchi, T. Kajishima, M. Inagaki, N. Horinouchi, A consistent

direct discretization scheme on Cartesian grids for convective and conjugate heat transfer, J. Comput. Phys. 227 (2016) 6372–6384.

[36] D. Goldstein, R. Handler, L. Sirovich, Modeling a No-Slip Flow Boundary with an External Force Field, J. Comput. Phys. 105 (1993) 354–366.

[37] M.C. Lai, C.S. Peskin, An immersed boundary method with formal second-order accuracy and reduced numerical viscosity, J. Comput. Phys. 160 (2000) 705–719.

[38] E.M. Saiki, S. Biringen, Numerical simulation of a cylinder in uniform flow: Application of a virtual boundary method, J. Comput. Phys. 123 (1996) 450–465.

[39] P. Angot, C.H. Bruneau, P. Fabrie, A penalization method to take into account obstacles in incompressible viscous flows, Numer. Math. 81 (1999) 497–520.

[40] G. Carbou, P. Fabrie, Boundary layer for a penalization method for viscous incompressible flow, Adv. Differ. Equations. 8 (2003) 1453–1480.

[41] T. Engels, D. Kolomenskiy, K. Schneider, J. Sesterhenn, Numerical simulation of fluid – structure interaction with the volume penalization method, J. Comput. Phys. 281 (2015) 96–115.

[42] K. Guo, X. Cui, M. Liu, A Coupled Lattice Boltzmann-Volume Penalization for Flows Past Fixed Solid Obstacles with Local Mesh Refinement, Math. Probl. Eng. 2018 (2018) 1–12.

[43] E.W. Hester, G.M. Vasil, K.J. Burns, Improving convergence of volume penalized fluid-solid interactions, (2020). arxiv.org/abs/1903.11914 (accessed June 10, 2020).

[44] D. Kolomenskiy, K. Schneider, A Fourier spectral method for the Navier–Stokes equations with volume penalization for moving solid obstacles, J. Comput. Phys. 228 (2009) 5687–5709.

[45] K. Schneider, Immersed boundary methods for numerical simulation of confined fluid and plasma turbulence in complex geometries: A review, J. Plasma Phys. 81 (2015) 1–21.

[46] M. Specklin, Y. Delauré, A sharp immersed boundary method based on penalization and its application to moving boundaries and turbulent rotating flows, Eur. J. Mech. B/Fluids. 70 (2018) 130–147.

[47] B. Lambert, L. Weynans, M. Bergmann, Local lubrication model for spherical particles within incompressible Navier-Stokes flows, Phys. Rev. E. 97 (2018) 1–16.

[48] B. Lambert, L. Weynans, M. Bergmann, Methodology for numerical simulations of ellipsoidal particle-laden flows, Int. J. Numer. Methods Fluids. 92 (2020) 855–873.

[49] B. Kadoch, D. Kolomenskiy, P. Angot, K. Schneider, A volume penalization method for incompressible flows and scalar advection-diffusion with moving obstacles, J. Comput. Phys. 231 (2012) 4365–4383.

[50] C. Jause-Labert, F.S. Godeferd, B. Favier, Numerical validation of the volume penalization method in three-dimensional pseudo-spectral simulations, Comput. Fluids. 67 (2012) 41–56.

[51] T. Engels, D. Kolomenskiy, K. Schneider, J. Sesterhenn, Two-dimensional simulation of the fluttering instability using a pseudospectral method with

volume penalization, Comput. Struct. 122 (2013) 101–112.

[52] W. Iwakami, Y. Yatagai, N. Hatakeyama, Y. Hattori, A new approach for error reduction in the volume penalizationmethod, Commun. Comput. Phys. 16 (2014) 1181–1200.

[53] D. Kolomenskiy, R. Nguyen Van Yen, K. Schneider, Analysis and discretization of the volume penalized Laplace operator with Neumann boundary conditions, Appl. Numer. Math. 95 (2015) 238–249.

[54] T. Engels, D. Kolomenskiy, K. Schneider, J. Sesterhenn, Numerical simulation of fluid–structure interaction with the volume penalization method, J. Comput. Phys. 281 (2015) 96–115.

[55] C. Bernier, M. Gazzola, R. Ronsse, P. Chatelain, Simulations of propelling and energy harvesting articulated bodies via vortex particle-mesh methods, J. Comput. Phys. 392 (2019) 34–55.

[56] K.J. Burns, D. Lecoanet, G.M. Vasil, J.S. Oishi, B.P. Brown, The “Sphered Cube”: A New Method for the Solution of Partial Differential Equations in Cubical Geometry, (2019). arxiv.org/abs/1903.12642 (accessed March 29, 2019).

[57] F.H. Harlow, J.E. Welch, Numerical calculation of time-dependent viscous incompressible flow of fluid with free surface, Phys. Fluids. 8 (1965) 2182–2189.

[58] S.O. Unverdi, G. Tryggvason, A front-tracking method for viscous, incompressible, multi-fluid flows, J. Comput. Phys. 100 (1992) 25–37.

[59] G. Tryggvason, R. Scardovelli, S. Zaleski, Direct numerical simulations of Gas-

Liquid multiphase flows, 2011.

[60] S. Osher, J.A. Sethian, Fronts propagating with curvature-dependent speed: Algorithms based on Hamilton-Jacobi formulations, J. Comput. Phys. 79 (1988) 12–49.

[61] C.. Hirt, B.. Nichols, Volume of fluid (VOF) method for the dynamics of free boundaries, J.Computational Phys. 39 (1981) 201–225.

[62] T. Qian, X.P. Wang, P. Sheng, Molecular scale contact line hydrodynamics of immiscible flows, Phys. Rev. E. 68 (2003) Article 016306.

[63] J.U. Brackbill, D.B. Kothe, C. Zemach, A continuum method for modeling surface tension, J. Comput. Phys. 100 (1992) 335–354.

[64] K. Yokoi, A practical numerical framework for free surface flows based on CLSVOF method, multi-moment methods and density-scaled CSF model: Numerical simulations of droplet splashing, J. Comput. Phys. 232 (2013) 252–271.

[65] T. Yamamoto, Y. Okano, S. Dost, Validation of the S-CLSVOF method with the density-scaled balanced continuum surface force model in multiphase systems coupled with thermocapillary flows, Int. J. Numer. Methods Fluids. 83 (2017) 223–244.

[66] A. Albadawi, D.B. Donoghue, A.J. Robinson, D.B. Murray, Y.M.C. Delauré, Influence of surface tension implementation in Volume of Fluid and coupled Volume of Fluid with Level Set methods for bubble growth and detachment, Int. J. Multiph. Flow. 53 (2013) 11–28.

[67] H. Rusche, Computational Fluid Dynamics of Dispersed Two-Phase Flows at

High Phase Fractions, PhD Thesis. (2002) 152–154.

[68] K.K. So, X.Y. Hu, N.A. Adams, Anti-diffusion method for interface steepening in two-phase incompressible flow, J. Comput. Phys. 230 (2011) 5155–5177.

[69] K. Washino, E.L. Chan, T. Kaji, Y. Matsuno, T. Tanaka, On large scale CFD–DEM simulation for gas–liquid–solid three-phase flows, Particuology. (2020). https://doi.org/10.1016/j.partic.2020.05.006.

[70] K. Yokoi, D. Vadillo, J. Hinch, I. Hutchings, Numerical studies of the influence of the dynamic contact angle on a droplet impacting on a dry surface, Phys. Fluids. 21 (2009) Artilcle 072102.

[71] M. Fujita, O. Koike, Y. Yamaguchi, Computation of capillary interactions among many particles at free surface, Appl. Phys. Express. 6 (2013) Article 036501.

[72] X. Sun, M. Sakai, Numerical simulation of two-phase flows in complex geometries by using the volume-of-fluid/immersed-boundary method, Chem. Eng. Sci. 139 (2016) 221–240.

[73] H. V. Patel, S. Das, J.A.M. Kuipers, J.T. Padding, E.A.J.F. Peters, A coupled Volume of Fluid and Immersed Boundary Method for simulating 3D multiphase flows with contact line dynamics in complex geometries, Chem. Eng. Sci. 166 (2017) 28–41.

[74] McDonald PW, Computation of transonic flow through two- dimensional gas turbine cascades, in: ASME Pap 71-GT-89, 1971.

[75] R. Maccormack, A. Paullay, Computational efficiency achieved by time splitting of finite difference operators, in: 10th Aerosp. Sci. Meet., 1972.

[76] S. V. Patankar, Numerical heat transfer and fluid flow, Taylor & Francis, 1980.

[77] H.K. Versteeg, W. Malalasekera, G. Orsi, J.H. Ferziger, A.W. Date, J.D. Anderson, An Introduction to Computational Fluid Dynamics - The Finite Volume Method, 1995.

[78] G.A. Taylor, M. Hughes, N. Strusevich, K. Pericleous, Finite volume methods applied to the computational modelling of welding phenomena, Appl. Math. Model. 26 (2002) 311–322.

[79] F. Moukalled, L. Mangani, M. Darwish, The finite volume method in computational fluid dynamics : An Advanced Introduction with OpenFOAM and Matlab, 2016.

[80] J. Tu, G.-H. Yeoh, C. Liu, J. Tu, G.-H. Yeoh, C. Liu, CFD Mesh Generation: A Practical Guideline, in: Comput. Fluid Dyn., Butterworth-Heinemann, 2018: pp. 125–154.

[81] R. Courant, E. Isaacson, M. Rees, On the solution of nonlinear hyperbolic differential equations by finite differences, Commun. Pure Appl. Math. 5 (1952) 243–255.

[82] R.A. Gentry, R.E. Martin, B.J. Daly, An Eulerian differencing method for unsteady compressible flow problems, J. Comput. Phys. 1 (1966) 87–118.

[83] J.H. Ferziger, M. Perić, Computational Methods for Fluid Dynamics, Springer-Verlag, Berlin, 1996.

[84] B.J. Alder, T.E. Wainwright, Phase transition for a hard sphere system, J. Chem. Phys. 27 (1957) 1208–1209.

[85] C.S. Campbell, C.E. Brennen, Computer simulation of granular shear flows, J.

Fluid Mech. 151 (1985) 167–188.

[86] W. Goldsmith, Impact: The Theory and Physical Behavior of Colliding Solids, J. Appl. Mech. Edward Arn (1961).

[87] J. Shäfer, S. Dippel, D.E. Wolf, Force Schemes in Simulations of Granular Materials, J. Phys. I. 1 (1996) 5–20.

[88] A.B. Stevens, C.M. Hrenya, Comparison of soft-sphere models to measurements of collision properties during normal impacts, Powder Technol. 23 (2005) 99–109.

[89] Mindlin, R. D., Compliance of elastic bodies in contact, J. Appl. Mech. 16 (1949) 259–268.

[90] Y. Tsuji, T. Tanaka, T. Ishida, Lagrangian numerical simulation of plug flow of cohesionless particles in a horizontal pipe, Powder Technol. 71 (1992) 239–250.

[91] K.L. Johnson, Contact Mechanics, Cambridge University Press, Cambridge, 1985. https://doi.org/DOI: 10.1017/CBO9781139171731.

[92] Y. Li, Y. Xu, C. Thornton, A comparison of discrete element simulations and experiments for “sandpiles” composed of spherical particles, Powder Technol. 160 (2005) 219–228.

[93] K. Samiei, Implicit and explicit algorithms in discrete element method, 2014.

[94] E. Hairer, C. Lubich, G. Wanner, Geometric numerical integration illustrated by the Störnier-Ver let method, Acta Numer. 12 (2003) 399–450.

[95] G.F.F. G, Hertz’s miscellaneous papers, Nature. 55 (1896) 6–9.

[96] A. Passalacqua, R.O. Fox, Implementation of an iterative solution procedure for multi-fluid gas-particle flow models on unstructured grids, Powder Technol. 213

(2011) 174–187.

[97] R.I. Issa, B. Ahmadi-Befrui, K.R. Beshay, A.D. Gosman, Solution of the implicitly discretised reacting flow equations by operator-splitting, J. Comput. Phys. 93 (1991) 388–410.

[98] L. Schiller, Z. Naumann, A drag coefficient correlation, Z.Ver.Deutsch.Ing. 77 (1935) 318–320.

[99] C. Jause Labert, Simulation numérique d'écoulements turbulents en rotation, confinement et forçage à l'aide d'une méthode de pénalisation, L'Université de Lyon, 2012.

[100] A.A. Zick, G.M. Homsy, Stokes flow through periodic arrays of spheres, J. Fluid Mech. 115 (1982) 13–26.

[101] S. Middleman, Capillary Penetration Dynamics, in: Model. Axisymmetric Flows Dyn. Film. Jets, Drops, Academic Press, San Diego, 1995: pp. 211–239.

[102] M. Denesuk, G.L. Smith, B.J.J. Zelinski, N.J. Kreidl, D.R. Uhlmann, Capillary penetration of liquid droplets into porous materials, J. Colloid Interface Sci. 158 (1993) 114–120.

[103] J. Kozeny, Uber kapillare Leitung des Wassers im Boden, Sitzungsber Akad. Wiss. Wien. 136(2a) (1927) 271–306.

[104] H. Brenner, The slow motion of a sphere through a viscous fluid towards a plane surface, Chem. Eng. Sci. 16 (1961) 242–251.

[105] S.L. Dance, M.R. Maxey, Incorporation of lubrication effects into the force-coupling method for particulate two-phase flow, J. Comput. Phys. 189 (2003) 212–238.

[106] J.A. Simeonov, J. Calantoni, Modeling mechanical contact and lubrication in Direct Numerical Simulations of colliding particles, Int. J. Multiph. Flow. 46 (2012) 38–53.

[107] K. Washino, S. Hashino, H. Midou, E.L. Chan, T. Tsuji, T. Tanaka, Lubrication force model for a pendular liquid bridge of power-law fluid between two particles, Chem. Eng. Res. Des. 132 (2018) 1030–1036.

[108] E. Biegert, B. Vowinckel, E. Meiburg, A collision model for grain-resolving simulations of flows over dense, mobile, polydisperse granular sediment beds, J. Comput. Phys. 340 (2017) 105–127.

[109] J. Gu, M. Sakaue, S. Takeuchi, T. Kajishima, An immersed lubrication model for the fluid flow in a narrow gap region, Powder Technol. 329 (2018) 445–454.

[110] J.J. Stickel, R.L. Powell, Fluid mechanics and rheology of dense suspensions, Annu. Rev. Fluid Mech. 37 (2005) 129–149.

[111] M. Maxey, Simulation Methods for Particulate Flows and Concentrated Suspensions, Annu. Rev. Fluid Mech. 49 (2017) 171–193.

[112] J. Topping, Investigations on the Theory of the Brownian Movement, Phys. Bull. (1956).

[113] M. Kunitz, Empirical formula for the relation between viscosity of solution and volume of solute, J. Gen. Physiol. 9 (1926) 715–725.

[114] M. Mooney, The viscosity of a concentrated suspension of spherical particles, J. Colloid Sci. 6 (1951) 162–170.

[115] T.F. Ford, Viscosity-concentration and fluidity-concentration relationships for suspensions of spherical particles in Newtonian liquids, J. Phys. Chem. 64

(1960) 1168–1174.

[116] Y. Yoshida, T. Katsumoto, S. Taniguchi, A. Shimosaka, Y. Shirakawa, J. Hidaka, Prediction of viscosity of slurry suspended fine particles using coupled DEM-DNS simulation, Chem. Eng. Trans. 32 (2013) 2089–2094.

[117] Y. Mori, N. Ototake, On the Viscosity of Suspensions, Chem. Eng. 20 (1956) 488–494.

[118] P.N. Rowe, A.W. Nienow, Particle mixing and segregation in gas fluidised beds. A review, Powder Technol. 15 (1976) 141–147.

[119] S. Ergun, Fluid flow through packed columns, Chem. Eng. Prog. 48 (1952) 89–94.

[120] M. Wörner, Numerical modeling of multiphase flows in microfluidics and micro process engineering: A review of methods and applications, Microfluid. Nanofluidics. 12 (2012) 841–886.

[121] K. Washino, E.L. Chan, T. Matsumoto, S. Hashino, T. Tsuji, T. Tanaka, Normal viscous force of pendular liquid bridge between two relatively moving particles, J. Colloid Interface Sci. 494 (2017) 255–265.

[122] J.W. Cahn, J.E. Hilliard, Free Energy of a Nonuniform System. I. Interfacial Free Energy, J. Chem. Phys. 28 (1958) 258–267.

[123] D.M. Anderson, G.B. McFadden, A.A. Wheeler, Diffuse-interface methods in fluid mechanics, Annu. Rev. Fluid Mech. 30 (1998) 139–165.

[124] J. Kim, Phase field computations for ternary fluid flows, Comput. Methods Appl. Mech. Eng. 196 (2007) 4779–4788.

[125] M. Meier, G. Yadigaroglu, B.L. Smith, A novel technique for including surface

tension in PLIC-VOF methods, Eur. J. Mech. B/Fluids. 12 (2002) 61–73.

[126] E.G. Puckett, A volume-of-fluid interface reconstruction algorithm that is second-order accurate in the max norm, Commun. Appl. Math. Comput. Sci. 5 (2010) 199–220.

[127] M. Sussman, An adaptive mesh algorithm for free surface flows in general geometries, in: and W.E.S. A. V. Wouwer , Ph. Saucez (Ed.), Adapt. Method Lines, Chapman and Hall/CRC, London, 2001: pp. 207 – 231.

[128] J.P. Boris, D.L. Book, Flux-corrected transport. I. SHASTA, a fluid transport algorithm that works, J. Comput. Phys. 11 (1973) 38–69.

[129] S.T. Zalesak, Fully multidimensional flux-corrected transport algorithms for fluids, J. Comput. Phys. (1979).

[130] B. van Leer, Towards the ultimate conservative difference scheme. V. A second-order sequel to Godunov's method, J. Comput. Phys. 32 (1979) 101–136.

[131] C. Kloss, C. Goniva, A. Hager, S. Amberger, S. Pirker, Models, algorithms and validation for opensource DEM and CFD-DEM, Prog. Comput. Fluid Dyn. 12 (2012) 140–152.

[132] M. Rayner, G. Trägårdh, C. Trägårdh, P. Dejmek, Using the Surface Evolver to model droplet formation processes in membrane emulsification, J. Colloid Interface Sci. 279 (2004) 175–185.

[133] S.J. Cox, A viscous froth model for dry foams in the Surface Evolver, Colloids Surfaces A Physicochem. Eng. Asp. 263 (2005) 81–89.

[134] A. Virozub, N. Haimovich, S. Brandon, Three-dimensional simulations of liquid bridges between two cylinders: Forces, energies, and torques, Langmuir. 25

(2009) 12837–12842.

[135] M. Mancini, E.M. Guène, J. Lambert, R. Delannay, Using Surface Evolver to measure pressures and energies of real 2D foams submitted to quasi-static deformations, Colloids Surfaces A Physicochem. Eng. Asp. 468 (2015) 193–200.

[136] S. Cho, R. Tummala, Y. Joshi, Capillary Performance of Micropillar Arrays in Different Arrangements, Nanoscale Microscale Thermophys. Eng. 22 (2018) 97–113.

[137] K.A. Brakke, The surface evolver, Exp. Math. 1 (1992) 141–165.

[138] G. Lian, C. Thornton, M.J. Adams, A Theoretical Study of the Liquid Bridge Forces between Two Rigid Spherical Bodies, J. Colloid Interface Sci. 161 (1993) 138–147.

[139] H.R. Liu, H. Ding, A diffuse-interface immersed-boundary method for two-dimensional simulation of flows with moving contact lines on curved substrates, J. Comput. Phys. 294 (2015) 484–502.

[140] T.L. Cook, F.H. Harlow, Virtual mass in multiphase flow, Int. J. Multiph. Flow. 10 (1984) 691–696.

[141] J. Boussinesq, Essai sur la theorie des eaux courantes, in: Mémoires Présentés Par Divers Savans à l'Académie R. Sci. l'Institut Fr. 23, Imprimerie nationale, 1877.